Universidade do Minho
Escola de Ciências

Raquel Gaudência Dias Andrade

Development of magnetic nanocarriers for enhanced anticancer potential of lactoferrin

dezembro de 2019

Raquel Gaudência Dias Andrade **Development of magnetic nanocarriers for enhanced anticancer potential of lactoferrin**

Uminho | 2019

Universidade do Minho
Escola de Ciências

Raquel Gaudência Dias Andrade

Development of magnetic nanocarriers for enhanced anticancer potential of lactoferrin

Dissertação de Mestrado
Mestrado em Biofísica e Bionanossistemas

Trabalho realizado sob orientação da
Professora Doutora Elisabete Maria dos Santos Castanheira Coutinho
e da
Professora Doutora Maria Manuela Sansonetty Gonçalves Côrte-Real

dezembro de 2019

Acknowledgements

Here, I would like to express my sincere gratitude for all the involved ones in this journey.

First, I would like to thank my research supervisors, Dr. Elisabete Castanheira Coutinho and Dr. Manuela Côrte-Real for accepting me in their groups, for providing the necessary tools to perform my work and for all the knowledge they passed on to me. I would also like to thank Dr. Paulo Coutinho for being always available to answer my questions.

I would like to express my deep gratitude to Cátia Pereira for her indispensable help and orientation in biological tests and acquisition of fluorescence images, performed in this work. I also want to thank Rita Rodrigues for her orientation, availability and useful suggestions throughout my investigation.

I must express my gratitude to my colleague and friend Sérgio Veloso for the initial orientation in the laboratory and for all the help and support during this work and, also, for challenging me with new ideas. I also want to thank all my friends that provided me good times and supported me.

I want to acknowledge the Center of Physics of the University of Minho and Porto (CF-UM-UP), the Center of Molecular and Environmental Biology (CBMA) and Center of Biological Engineering (CEB) for providing me the equipment and resources needed in this work. I would like to extend my gratitude to the Unidade de Microscopia Electrónica of University of Trás-os-Montes and Alto Douro for providing the X-ray diffraction technique, to University of Aveiro for the SQUID measurements at CICECO, and C.A.C.T.I. of the University of Vigo for providing the transmission electron microscopy images.

Last, and above all, I would like to thank to my loving parents, for always supporting me and encouraging me to be the best I can. For all their effort to provide me everything that I needed to reach this stage. For this and many other things I will always be grateful.

STATEMENT OF INTEGRITY

I hereby declare having conducted this academic work with integrity. I confirm that I have not used plagiarism or any form of undue use of information or falsification of results along the process leading to its elaboration.

I further declare that I have fully acknowledged the Code of Ethical Conduct of the University of Minho.

Título: Desenvolvimento de nanotransportadores magnéticos para aumento do potencial anticancerígeno da lactoferrina

Resumo: A nanotecnologia tem sido um importante ramo da ciência para o desenvolvimento e manipulação de materiais à nanoescala, tendo aplicações em diversas áreas, nomeadamente nas ciências biomédicas. As nanopartículas magnéticas têm sido alvo de investigação na área da nanomedicina pelas suas propriedades únicas, como o superparamagnetismo, que torna possível o desenvolvimento de novas terapias do cancro, como a hipertermia magnética e o transporte guiado de fármacos específico, superando as limitações dos métodos convencionais. A elevada razão superfície/volume permite um grande número de ligandos funcionais à superfície, sendo de elevada importância para a produção de nanossistemas biocompatíveis e não tóxicos. Para reduzir a agregação das nanopartículas e aumentar o tempo de vida na circulação sanguínea, têm sido investigadas formas de incorporar nanopartículas em nanotransportadores como, por exemplo, os lipossomas. Os magnetolipossomas aquosos e sólidos são nanotransportadores de excelência constituídos por nanopartículas magnéticas dentro de uma bicamada lipídica, com a capacidade de guiar fármacos até um local específico quando aplicado um campo magnético externo. A lactoferrina é uma glicoproteína multifuncional sequestradora de Fe^{3+}, que intervém no transporte do ferro, na resposta imunitária, na atividade antioxidante e possui uma importante capacidade antimicrobiana e anticancerígena. A eficácia terapêutica da lactoferrina dependerá da criação de novas formulações que integrem a lactoferrina e outros agentes quimioterapêuticos permitindo uma terapia dual do cancro. Neste trabalho, foram desenvolvidos magnetolipossomas aquosos (AMLs) e sólidos (SMLs) carregados ou funcionalizados com lactoferrina, respectivamente. Devido à sua baixa toxicidade, fácil preparação e elevada suscetibilidade magnética, foram preparadas nanopartículas de ferrite de manganês, cujas propriedades estruturais e magnéticas foram avaliadas. A eficiência de encapsulamento e a localização da lactoferrina nos nanotransportadores foram avaliadas por técnicas de fluorescência (FRET, anisotropia de fluorescência e inibição de fluorescência). Informação acerca do tamanho, índice de polidispersividade e carga superficial foi obtida por DLS. A atividade biológica dos magnetolipossomas com e sem lactoferrina foi testada em leveduras, em linhas celulares de mama tumorigénicas e não-tumorigénicas, revelando baixa citotoxicidade em leveduras e células do cancro da mama. A internalização foi observada, por microscopia de fluorescência, em células de cancro da mama e em células não tumorais.

Palavras-chave: Citotoxicidade, Lactoferrina, Magnetolipossomas, Nanopartículas magnéticas, Terapia do cancro.

Title: Development of magnetic nanocarriers for enhanced anticancer potential of lactoferrin

Abstract: Nanotechnology has become a fundamental science for the development and manipulation of materials with dimensions at the nanoscale, exhibiting applications in several areas, namely in biomedical sciences. Magnetic nanoparticles have been widely investigated in nanomedicine due to their unique properties, like superparamagnetism, that makes possible the development of new cancer therapies, like magnetic hyperthermia and targeted drug delivery, overcoming many limitations of conventional methods. The large surface-to-volume ratio allows a high loading of functional ligands at the surface, which is of major importance to produce biocompatible and non-toxic nanosystems. To reduce nanoparticles aggregation and increase their circulation lifetime, several strategies have been developed to load magnetic nanoparticles into delivery vectors, such as liposomes. Magnetoliposomes, both aqueous and solid, are nanocarriers of excellence composed by magnetic nanoparticles entrapped in a lipid bilayer, that can guide therapeutic drugs to a specific site of interest by application of an external magnetic field. Lactoferrin is a Fe^{3+}-binding glycoprotein with multifunctional properties, including in iron transport, immune response and with important antimicrobial, antioxidant and anticancer activities. The therapeutic efficacy of lactoferrin on anticancer therapy may be enhanced by the development of new formulations capable of delivery lactoferrin to tumor sites. In this work, aqueous (AMLs) and solid (SMLs) magnetoliposomes loaded or functionalized with lactoferrin, respectively, were developed. Due to their low toxicity, simple preparation and high magnetic susceptibility, manganese ferrite nanoparticles were prepared, and their structural and magnetic properties were evaluated. The encapsulation efficiency and location of lactoferrin in these nanocarriers was assessed by fluorescence-based techniques (FRET, fluorescence anisotropy and fluorescence quenching). Information about size, polydispersity index and surface charge, was obtained by DLS. The biological activity of plain and lactoferrin-loaded magnetoliposomes was tested in yeast, in breast cancer and non-tumorigenic cell lines, revealing lower cytotoxicity in yeast and breast cancer cells. Internalization of magnetoliposomes was observed by fluorescence microscopy in breast cancer and non-tumorigenic cells.

Key words: Cancer therapy, Cytotoxicity, Lactoferrin, Magnetoliposomes, Magnetic nanoparticles.

Index

Abbreviation list

AC ..... Alternating Current

AEC–CP–Fe-bLf ..... alginate-enclosed chitosan–calcium phosphate-loaded-Fe-bLf

AMF ..... Alternating Magnetic Field

AML ..... Aqueous magnetoliposomes

anti-EGFR ..... anti-Epidermal Growth Factor Receptor

ASGRP ..... Asialoglycoprotein Receptor

bLf ..... bovine Lactoferrin

CCD ..... Charged Coupled Device

CDI ..... N,N'-carbonyl Diimidazole

Chol ..... cholesterol

concA ..... concanamicine A

CONTIN ..... constrained regularization method for inverting data

DLS ..... Dynamic Light Scattering

DMEM ..... Dulbecco's modified Eagle's medium

DNA ..... Deoxyribonucleic Acid

DOX ..... Doxorubicin

DPH ..... Diphenylhexatriene

DPPC/PG ..... Dipalmitoylphosphatidylcholine/Phosphatidylglycerol

DSPE-PEG_{2000} ..... 1,2-distearoyl-sn-glycero-3-phosphoethanolamine-N-[amino(polyethylene glycol)-2000]

EDL ..... Electric Double Layer

EDS ..... Electron Dispersive Spectroscopy

EDX ..... Energy Dispersive X-ray

Egg-PC ..... Egg-yolk Phosphtidylcholine

EGF ..... Epidermal Growth Factor

ELS ..... Electrophoretic Light Scattering

EPR ..... Enhanced Permeability and Retention

FA ..... Folic Acid

FBS ..... Fetal Bovine Serum

FC ..... Field Cooling

FR ..... Folate Receptor

FRET ..... Förster Resonance Energy Transfer

FWHM ..... Full Width at Half Maximum

GSH ..... Glutathione

GUVs..... Giant Unilamellar Vesicles

HAADF ..... High Angle Annular Dark Field

HOMO..... Highest Occupied Molecular Orbital

HR-TEM..... High Resolution Transmission Electron Microscopy

Lf ..... Lactoferrin

LHRH ..... Luteinizing Hormone Releasing Hormone

LUMO ..... Lowest Unoccupied Molecular Orbital

LUVs ..... Large Unilamellar Vesicles

MLVs..... Multilamellar vesicles

MNPs..... Magnetic Nanoparticles

MRI ..... Magnetic resonance imaging

MVVs..... Multivesicular vesicles

NAD ..... Nicotinamide Adenine Dinucleotide

NPs..... Nanoparticles

OD ..... Optical Density

PDI..... Polydispersity Index

PEG ..... Polyethylene Glycol

PEI ..... Poly(ethyleneimine)

pH_i ..... intracellular pH

PLGA..... Poly(lactide-co-glycolide)

RES..... Reticulo-Endothelial System

RGD..... arginyl-glycyl-aspartic acid

ROS ..... Reactive Oxygen Species

SEM ..... Scanning Electron Microscopy

SML ..... Solid magnetoliposomes

SPIONs ..... Superparamagnetic Iron Oxide Nanoparticles

SQUID..... Superconducting Quantum Interference Device

SRB ..... Sulforhodamine B

STEM ..... Scanning Transmission Electron Microscopy

SUVs..... Small Unilamellar Vesicles

TEM ..... Transmission Electron Microscopy

XRD ..... X-ray Diffraction

YPD..... Yeast extract Peptone Dextrone

ZFC ..... Zero-Field-Cooling

ZP ..... Zeta Potential

17-AAG 7-allylamio-17-desmethoxygeldanamycin

ΔpH ..... pH gradient

Figure index

Table index

Chapter 1 – Introduction

1.1. Nanoparticles and nanomedicine

Nanotechnology has become a fundamental science for the development and manipulation of materials at the nanoscale with important applications in many areas such as biomedical sciences, materials and electronic engineering, food industry, cosmetics and pharmaceutics [1]. Thus, nanotechnology uses nanoparticles and their unique properties to promote technological advances in many areas. Nanoparticles are materials with sizes in the range 1-100 nm at least in one dimension with different physicochemical properties from the bulk size [1]. As size gets smaller, quantum mechanics rules the behavior of materials resulting in different optical, electronic and magnetic properties, that are not only size but also shape dependent [1,2]. The jellium model assumes that nanoparticles, like atoms, have valence and conduction bands that dictate their electronic properties. The electrons in the valence band or highest occupied molecular orbital (HOMO) can absorb energy and jump to the nearest band, which is the lowest unoccupied molecular orbital (LUMO) or conduction band. When electrons leave valence band, they dissociate from the electron-hole, their mathematically opposite positive charge. In semiconductors, there is a band gap between the valence and conduction bands and electrons can only migrate from HOMO to LUMO if they absorb the equivalent to the energy of the band gap (gap energy). A decrease in size is associated to a decrease in confinement dimensions, resulting in discrete energy levels and increase in the energy gap, in a process called quantum confinement (figure 1.1.A). This process can be optically observed through a radiation shift from red to blue in semiconductor nanoparticles (figure 1.1.B) [1]. Other important feature of nanoparticles is their large surface to volume ratio, resulting in an increased surface area that can be modified with various types of molecules.

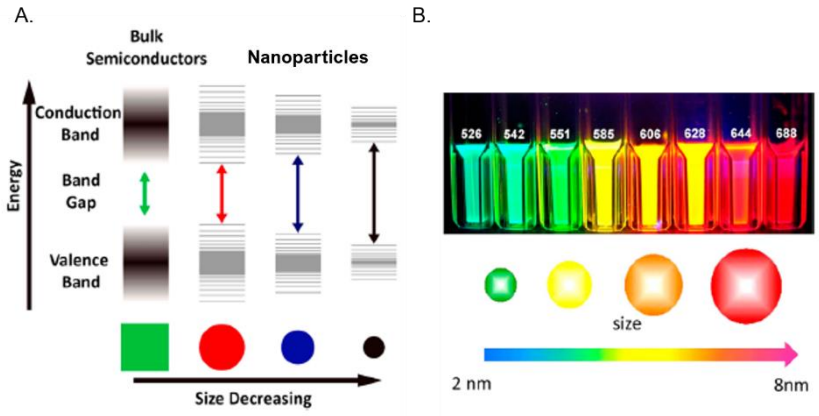

Figure 1.1. A. Energy diagrams for bulk semiconductors and semiconductor nanoparticles. **B.** Size-dependent tunable emissions for semiconductor nanoparticles. Adapted from [3].

The use of nanoparticles and their unique size-dependent properties for medicine has grown as the need for new therapy and diagnosis alternatives increases. Considering the problems related with conventional drug administration like poor solubility, nonspecific distribution, low bioavailability, rapid elimination and intrinsic toxicity, nanotechnology has proven to be the answer for an efficient administration minimizing adverse side effects, as the drug can be loaded into nanocarriers and be delivered in a controlled and safe manner [2]. Many nanomaterials can be used in nanomedicine such as magnetic nanoparticles, quantum dots, polymeric nanoparticles, viral-based nanoparticles, micelles, dendrimers and liposomes [4,5]. Thus, nanomedicine can be considered as the utilization of nanotechnology for designing novel biomedical tools for diagnosis and therapy, including drug delivery, *in vivo* imaging, *in vitro* diagnostics, biomaterials and active implants [6]. The key for an efficient drug administration and bioimaging is selective targeting, and that can be accomplished using nanocarriers that are able of passing biological barriers and accumulate in a specific tissue [7,3]. Due to their surface area, nanoparticles can be functionalized with different types of molecules (polymers, proteins, antibodies) that improve selectivity, protect them from opsonization and rapid clearance and increase their half-life circulation in the bloodstream [8,9].

The major focus of nanomedicine is cancer diagnosis and therapy (theranostics) through drug delivery and bioimaging [10]. Nanoparticles can either work as nanocarriers for anticancer drugs or act as contrast agents in diagnostic imaging like MRI (Magnetic Resonance Imaging) (figure 1.2) [3,8]. The advantage of using nanoparticles in cancer theranostics is that they can extravasate from the bloodstream and accumulate in tumor cells through a process called enhanced permeability and retention (EPR) effect. This effect is possible because the fast-growing tumor cells require the continuous formation of new vessels to oxygen supply, failing in the recruitment of important structural regulators. Thus, the resulting vasculature is disorganized and leaky, becoming a gateway to the entry of nanoparticles [4,11]. Besides passive targeting like EPR effect, other possible mechanism is receptor-mediated targeting that can be accomplished by conjugating ligands or antibodies in the surface of drug carriers, allowing their specific binding to cancer cells [11].

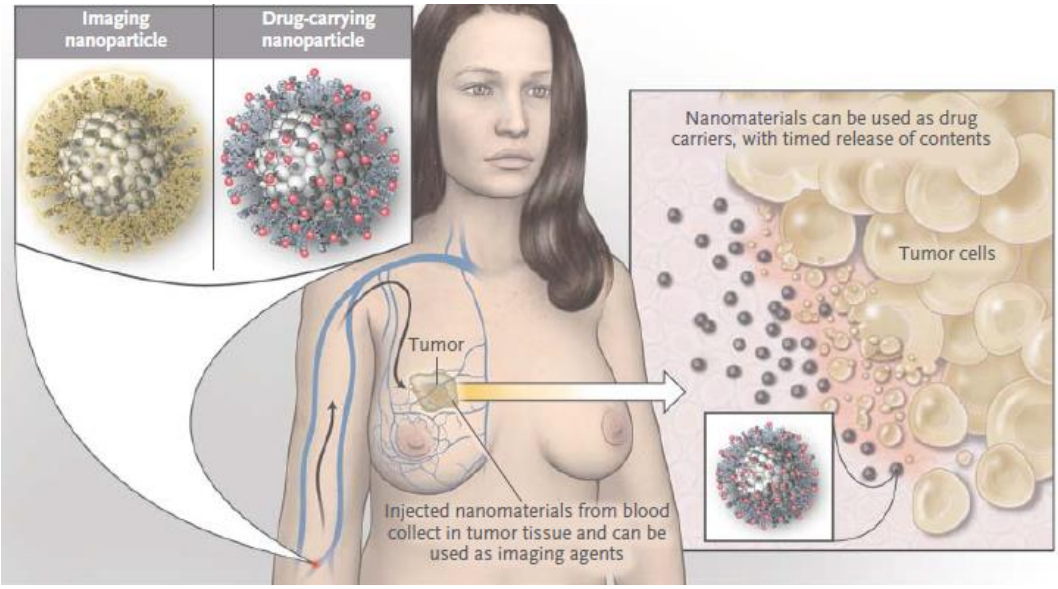

Figure 1.2. Nanoparticles can be used in diagnostic, as imaging agents, and therapy, as drug carriers (theragnostic). Reproduced from [8].

1.2. Magnetic nanoparticles

Magnetic nanoparticles are materials with dimensions below 100 nm that show response to an external applied magnetic field [12]. Among the existing types of magnetic materials, ferromagnetic (Fe, Ni, Co) and ferrimagnetic materials (iron oxides) exhibit important features for biomedical applications, like biocompatibility and chemical stability [13,14]. Ferromagnetic materials are composed by domains (Weiss domains) in which the magnetic moments of their atoms are parallel and create a net magnetic moment of that domain. The magnetic moments of the domains have different directions, canceling each other, and giving the material a zero net magnetic moment [12,15]. When a magnetic field is applied, all domains have their magnetic moments aligned with the external magnetic field. In ferrimagnetic materials, on the other hand, magnetic moments are parallel but with different magnitudes resulting in appearance of spontaneous magnetization [12,15]. Magnetic nanoparticles show several properties that result from finite-size effects and surface effects such as high magnetization and superparamagnetism which make them interesting for use in nanomedicine [16]. The dependence between magnetic behavior of ferromagnetic materials and their size results from the structure of their magnetic domains. When size decreases to a threshold value (commonly 20 nm [8]), the ferromagnetic material becomes a single domain which is characterized by a uniform magnetization (figure 1.3) [15-17].

The magnetic behavior of a ferromagnetic material is described by a hysteresis loop which depends on its remanence and coercivity [16]. Coercivity or coercive field refers to the opposite applied force that is

required to reduce the magnetization to zero [15,16]. Coercivity reaches a maximum value in the critical diameter and becomes zero as size decreases below this value. At this point, and above the blocking temperature (T_B), nanoparticles enter in the superparamagnetic regime, that is characterized by the loss of magnetization upon removal of an applied magnetic field (remanent magnetization) [15-18]. This property is of major importance in biological applications because avoids aggregation of nanoparticles and other undesirable effects in physiological fluids.

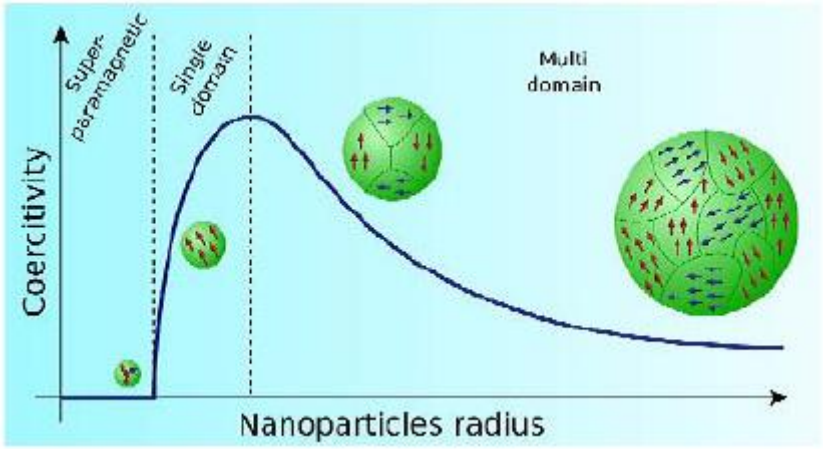

Figure 1.3. Size-dependent behavior of magnetic nanoparticles. Reproduced from [16].

Among the magnetic nanoparticles, superparamagnetic iron oxide nanoparticles, such as magnetite (Fe_3O_4), maghemite (γ-Fe_2O_3), calcium ferrite ($CaFe_2O_4$) and manganese ferrite ($MnFe_2O_4$) have been increasingly explored for drug delivery, hyperthermia, tissue targeting and repair, cellular labeling and magnetic resonance imaging, due to their low cell toxicity and ability to not retain any magnetization after the magnetic field is removed [19,20]. In order to efficiently use these nanoparticles in biological media, important parameters such as their magnetic response, size and shape, surface charge, colloidal stability and surface coating must be considered [21]. Controlled size, shape and surface chemistry can be achieved with proper fabrication methods. The principal routes of iron oxide nanoparticles preparation are physical (physical vapor deposition, aerosol), chemical (co-precipitation, hydrothermal) and biological methods (microbial incubation) [22]. Although several methods can be chosen to obtain the desirable properties, the most frequently used are chemical-based methods, due to their efficiency, simplicity and possible management of conditions, like Fe^{2+}/Fe^{3+} ratio, pH and ionic strength, to control size, shape and composition of nanoparticles [22,23]. Co-precipitation is a liquid phase method that is widely used in magnetite production. This method is based on precipitation of mixed ferric and ferrous ions at a 1:2

molar ratio under alkaline conditions and absence of oxygen [22-24]. Manganese ferrite nanoparticles can also be obtained by co-precipitation method mixing Mn^{2+} ions with Fe^{3+} ions in the same molar ratio and alkaline conditions [25,26]. One of the problems of bare iron oxide nanoparticles in suspension is their tendency to agglomerate due to strong magnetic forces, van der Waals forces and high surface energy. Surface coating and functionalization is often performed to chemically stabilize the surface of bare nanoparticles [22-24]. Organic (polymers, surfactants) and inorganic (metallic NPs, silica) compounds can be employed to obtain core-shell, matrix dispersed and shell-core-shell structures, which protect iron oxide nanoparticles from chemical degradation and allow functionalization with biomolecules at the surface, making them suitable for *in vivo* applications [27,28].

1.3. Magnetic nanoparticles in cancer diagnosis and treatment

The problems associated with cancer therapy and diagnosis defy scientists to develop alternative solutions to the conventional techniques. The unique physicochemical properties of magnetic nanoparticles described above, like superparamagnetic behavior and large surface-to-volume ratio, allow an improved circulation in biological systems and a specific targeting, which in turn lowers therapeutic dosage and side effects [29]. Nanoparticles size should be between 10 to 100 nm so they can enter the capillaries and avoid rapid renal clearance. The surface functionalization with cationic or hydrophilic polymers is also important because allows to reduce opsonization and off-target toxicity. In order to achieve a specific target, magnetic nanoparticles undergo two types of targeting, the passive and active targeting [30,31]. The EPR effect is present in the solid tumor microenvironment, characterized by a hypervascularization, augmented vascular permeability and lack of lymphatic drainage [30,31]. These features make possible the passive targeting of magnetic nanoparticles, which have an easier entry in the tumor cells because of their nanosize, promoting specific targeting and increasing the therapeutic effect of drugs [30,31]. The active targeting can be achieved by nanoparticles surface modification in which specific ligands for the tumor cells receptors are attached to the nanoparticles like peptides and antibodies, e.g. luteinizing hormone releasing hormone (LHRH), folate, RGD (arginyl-glycyl-aspartic acid) and anti-epidermal growth factor receptor (anti-EGFR) or by an external magnetic field gradient (figure 1.4) [32]. Active targeting with an applied magnetic field takes advantage on the responsiveness of magnetic nanoparticles towards a magnetic field depending on several parameters like magnetic susceptibility of the magnetic core, the volume of the core and magnetic permeability of free space [33]. Iron oxide nanoparticles have been extensively used in cancer diagnosis as enhanced contrast agents in MRI [34]. The main advantages of

MRI are high spatial resolution, soft tissue contrast, and most important, the possibility to early detect the presence of tumors, increasing therapy success [34]. Thus, it is of major importance the conception of new strategies that can optimize this technique. Superparamagnetic iron oxide nanoparticles (SPIONs) are strong candidates to be used as contrast agents due to their biocompatibility and ability to increase contrast enhancement [35]. A MRI image is obtained through nuclear relaxation of the tissue protons, that can be longitudinal (T1) or transversal (T2) [36-38]. Positive contrast agents (T1) decrease longitudinal relaxation time, resulting in a brighter image, while negative contrast agents (T2) decrease transversal longitudinal relaxation time, causing a darkening in MRI image (figure 1.5) [36-38]. Commonly, SPIONs are used for darkening T2- weighted images, but it was already reported that these nanoparticles are also capable to provide positive contrast enhancement, overpassing the toxicity of the usual gadolinium chelates contrast agents [39-41].

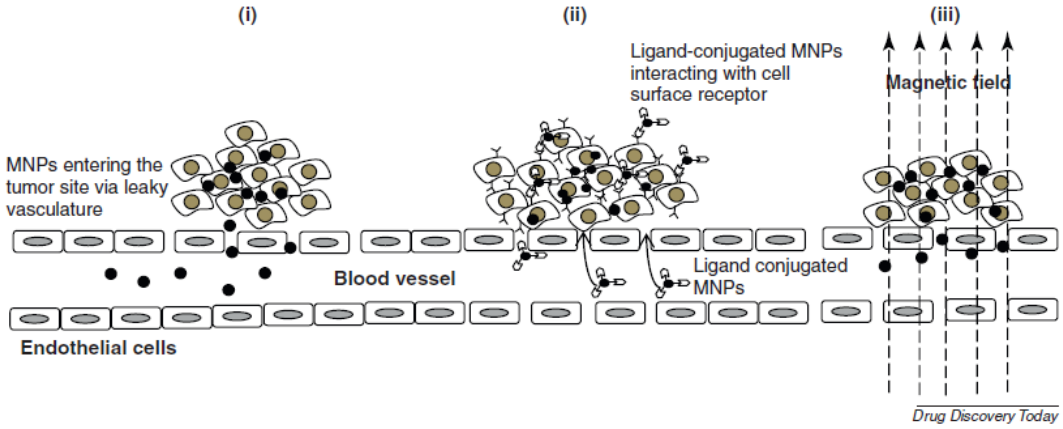

Figure 1.4. Schematic representation of three types of mechanisms of tumor cells targeting. (i) Passive targeting in which MNPs have an easier entry due to EPR effect; (ii) Active targeting with modification of MNPs with specific ligands to surface receptors; (iii) Active targeting promoted by a magnetic field that deliver MNPs to tumor cells. Reproduced from [32].

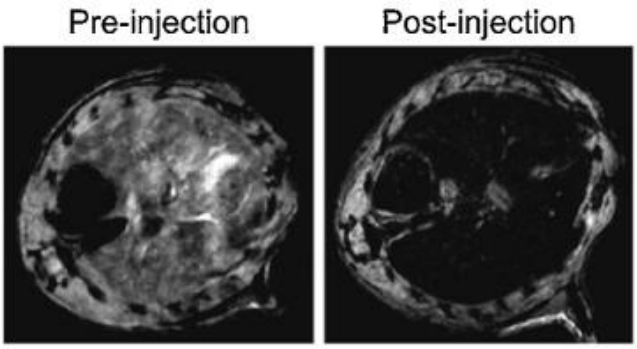

Figure 1.5. MRI images of mouse liver before and after 2 hours of exposure to dextran coated bismuth-iron oxide nanoparticles. Reproduced from [34].

Cancer cells can be killed when exposed to high temperatures between 41 and 47 °C in a process called hyperthermia [42]. Hyperthermia can be induced when magnetic nanoparticles are exposed to an alternating magnetic field (AMF) and produce heat due to Néel and Brownian relaxations of the rotating magnetic moments induced by the alternating current (AC) magnetic field in single-domain nanoparticles [42,43]. Metallic nanoparticles have the highest saturation magnetization, but their inherent toxicity and chemical instability make them not suitable for biomedical applications. Thus, the most used nanoparticles for hyperthermia applications are iron oxide nanoparticles that show low toxicity, facile fabrication and physical and chemical unique properties [33,43]. This treatment can be combined with specific delivery of therapeutic drugs into the tumor cells, in order to increase the therapeutic effect and reduce the needed dosage and side effects [42,43].

The appliance of an external magnetic field to magnetic nanoparticles allows their accumulation on cancer cells and the release of drugs (e.g. paclitaxel, doxorubicin) that can be attached in the nanoparticles coating by bioconjugation, electrostatic or hydrophobic interactions and by encapsulation (figure 1.6) [33]. The combined hyperthermia and chemotherapy create a synergistic effect that results in an increased drug accumulation and toxicity in tumor cells because of augmented blood flow and enhanced cellular permeability induced by the rise of local temperature [44]. To stabilize the nanoparticle suspension, to avoid the immune system and increase the half-life in the blood stream, the surface chemistry of nanoformulations must be considered [45,46]. The nanoparticles functionalization can be made by polymeric stabilizers like polyethylene glycol (PEG), Dextran, poly(lactic-co-glycolic acid) (PLGA), chitosan and poly(ethyleneimine) (PEI), nonpolymeric stabilizers like fatty acids, silica and gold, and by targeting ligands like lactoferrin, which belongs to the transferrins family of proteins [19,46]. PEG is a widely used coating polymer due to its hydrophilicity, non-immunogenic properties, reduced reticuloendothelial system (RES) uptake and capacity to act as a steric barrier *in vivo* to macromolecules like opsonins [46,47].

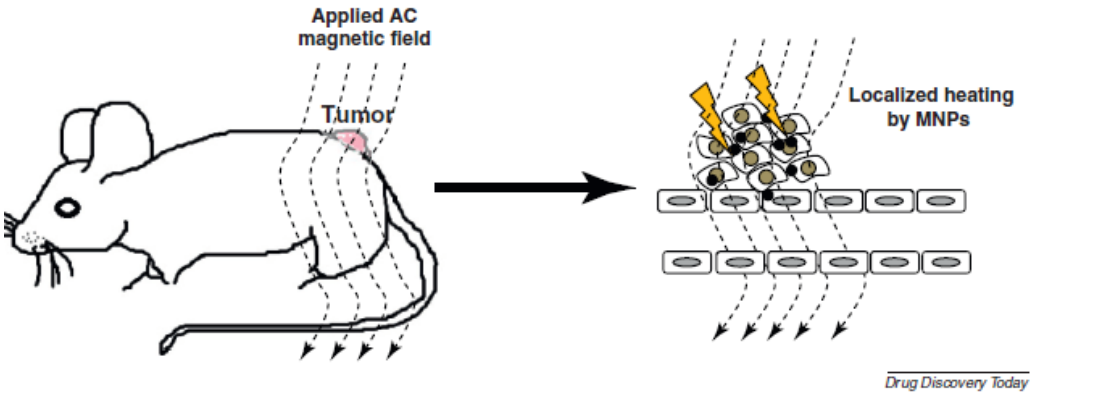

Figure 1.6. Schematic representation of hyperthermia mechanism. After the MNPs being accumulate in the tumor cells, an applied alternating magnetic field promotes alignment of nanoparticles with the magnetic field and the release of heat when relaxation occurs, killing the cancer cells, that are more sensitive to the higher temperatures (41-47 °C) than normal cells. Reproduced from [32].

1.4. Liposomes – nanocarriers in drug delivery

As described before, *in vivo* administration of bare magnetic nanoparticles can be problematic. The use of nanocarriers for magnetic nanoparticles like polymeric nanoparticles, hydrogels, dendrimers and liposomes, allows an efficient drug delivery with controlled release of drugs, reduction of systemic exposure and non-specific cell binding as well as storage and protection of therapeutic drugs inside the body avoiding the harming of healthy cells [48].

Liposomes are spherical structures composed by single or multiple phospholipid bilayers organized by self-assembly, that can be classified in different types depending on their size, organization and preparation method. Unilamellar vesicles comprise the small unilamellar vesicles (SUVs) that have sizes below 200 nm and the large unilamellar vesicles (LUVs) that have a size ranging from 200 to 1000 nm. Multilamellar vesicles (MLVs) are composed by multiple concentric bilayers and multivesicular vesicles (MVVs) consist in several small vesicles inside larger ones (figure 1.7.A) [49,50]. MLVs can be produced by the widely used thin-film hydration method, firstly reported by Bangham *et al.* [51]. In this method, lipid is dissolved in an organic solvent, followed by evaporation of solvent that creates a lipid film [52,53]. The lipid film is then dispersed with an aqueous solution. SUVs can be obtained through sonication of MLVs. The main disadvantage of this method is its low encapsulation efficiency of water-soluble drugs [52]. Among solvent dispersion methods, ethanolic injection and reverse phase evaporation methods are the most common. Ethanolic injection consists in the injection of a mixture of lipids dissolved in ethanol directly to the aqueous phase that produces unilamellar vesicles, however with some heterogeneity [53].

The reverse phase evaporation allows the production of liposomes with high aqueous volume-to-lipid ratio [53]. In this method, the aqueous phase and the organic solvent containing the lipids are sonicated and reverse micelles are obtained, which are spherical layers of phospholipids with hydrophobic chains exposed to the organic solvent and the head groups delimiting an aqueous core. As the solvent is removed, micelles are converted to a gel form and when a critical point is achieved, the excess of phospholipids lead to the formation of liposomes [53,54]. These two methods present higher encapsulation efficiencies than the thin-film hydration [52].

The main advantages of using liposomes as nanocarriers are their biocompatibility and the fact that liposomes can bear both hydrophilic and hydrophobic drugs entrapped in its aqueous center or encapsulated in the lipid bilayer, respectively [50]. These properties arise from the nature of their building blocks, the phospholipids. Phospholipids are amphiphilic molecules that have a hydrophilic head group containing phosphate and two hydrophobic acyl chains [52,55]. When dispersed in aqueous solutions, hydrophobic chains interact with each other, while the polar head prefer the aqueous environment. A lipid bilayer is formed due to the hydrophobic and Van der Waals interactions between acyl chains of two layers, and hydrogen bonds of the head group with water molecules (figure 1.7.B) [52,55].

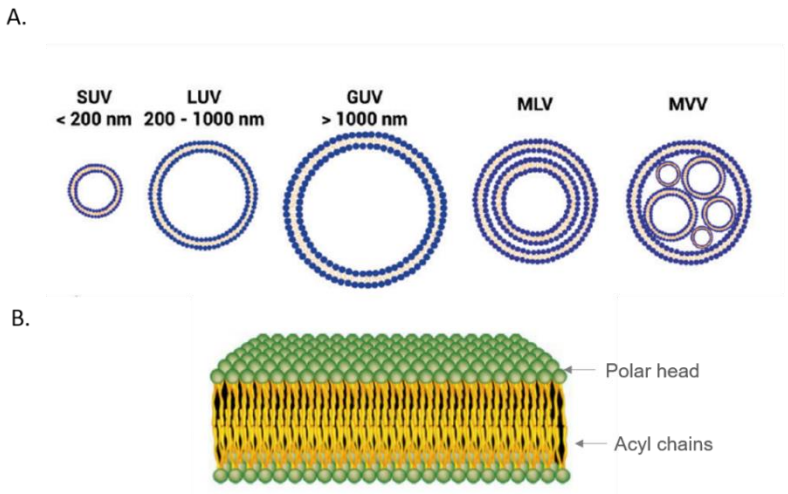

Figure 1.7. A. Different types of liposomes and correspondent sizes. **B.** Schematic representation of a lipid bilayer. A and B reproduced from [50] and [52], respectively.

Liposomes have been used as carriers for therapeutic drugs for more than 40 years and new types of liposome-based nanocarriers are still being investigated [55]. Liposomes can protect the encapsulated compounds from oxidation and degradation before reaching the desired location, also protecting healthy

cells from the action of carried drugs and increasing their therapeutic index. Clinical applications of liposomes have been rising, especially in cancer treatment, that is accompanied with modification in liposomal formulations. Long-circulating liposomes are developed to increase the half-life of liposomes in blood circulation. This can be achieved by functionalization of the surface of liposomes with biocompatible molecules like PEG, that avoids interaction with opsonins and uptake by the reticuloendothelial system [56,57]. Targeted delivery of liposomes is possible when antibodies or receptor ligands are attached in the surface of liposomes. Folate-mediated liposome targeting takes advantage of overexpression of folate receptors in cancer cells to increase the uptake of liposomes [58]. Other popular approach is the use of transferrin ligands in liposomes to improve their uptake in cancer cells that overexpress transferrin receptors [59]. Dual-targeted PEGylated liposomes showed an increased association and uptake by HeLa cancer cells, improving the anticancer activity of doxorubicin [60]. Thermosensitive liposomes that are below the melting temperature of lipid bilayers (T_m) are found in a rigid and highly organized gel state while above T_m they form a liquid crystalline fluid phase, thus triggering drug delivery when exposed to hyperthermic temperatures and rising the tumor drug uptake up to 20-30 times more [61]. pH-sensitive liposomes can change their conformation in the presence of an acidic environment, like the tumor microenvironment, facilitating the controlled release of therapeutic drugs [62].

1.5. Magnetoliposomes

Magnetoliposomes are liposomes that incorporate magnetic nanoparticles entrapped in the aqueous core (aqueous magnetoliposomes, AMLs) or covered with a lipid bilayer (solid magnetoliposomes, SMLs). Magnetoliposomes are multifunctional nanocarriers that can be used in nanotheranostics. The presence of magnetic nanoparticles allows the guidance of magnetoliposomes with therapeutic drugs to the tumor site through the application of an external magnetic field, a process called magnetic drug targeting. Drug delivery of these compounds can be monitored through MRI, given the ability of iron oxide nanoparticles to work as T2 contrast agents [64]. Besides that, it is possible to incorporate hydrophobic dyes in the lipid bilayer, allowing the *in vitro* tracking of magnetoliposomes by fluorescence microscopy [65].

The unique features of magnetic nanoparticles and the increased pharmacokinetics of liposomes make these nanosystems ideal for combined cancer hyperthermia and chemotherapy. Magnetoliposomes are considered multifunctional drug delivery systems, as they can trigger the controlled release of loaded drugs through thermal activation, when an alternating magnetic field is applied, and undergo biological targeting with binding of specific ligands to receptors present in tumor cells (figure 1.8) [64,66,67].

Kulshrestha *et al.* [68] developed encapsulated paclitaxel and iron oxide nanoparticles functionalized with acid citric in magnetoliposomes in which the lipid bilayer was formed by two thermosensitive lipids, DPPC/PG at a 9:1 molar ratio, to stabilize liposomes at temperatures lower than the gel-liquid crystalline phase transition temperature avoiding the early drug release. Here, magnetoliposomes improved the therapeutic efficacy on tumor cells and showed great potential for hyperthermia and drug release application.

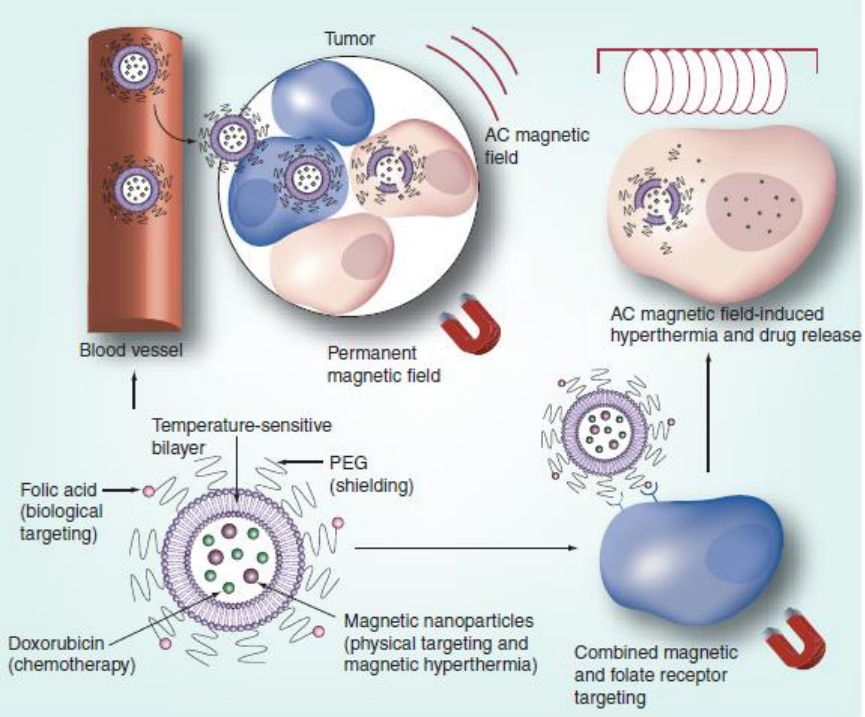

Figure 1.8. Multifunctional magnetoliposomes in cancer chemotherapy and hyperthermia. PEGylated doxorubicin loaded magnetoliposomes functionalized with specific ligands, such as folic acid, enable a physical and biological targeting. The controlled release of the loaded drug (chemotherapy) from thermosensitive liposomes is triggered through the application of an alternating magnetic field that induces the production of heat (hyperthermia). Reproduced from [64].

Conventional administration of doxorubicin (DOX) is non-specific, resulting in drug acting in healthy tissues, possibly causing heart failure. A method to avoid this can be the drug encapsulation in magnetoliposomes [69]. For example, magnetoliposomes loaded with doxorubicin were developed for colorectal cancer cells, in which iron-oxide magnetic nanoparticles coated with citric acid were used (figure 1.9) and it was demonstrated that this formulation induced 56% death of cancer cells [70].

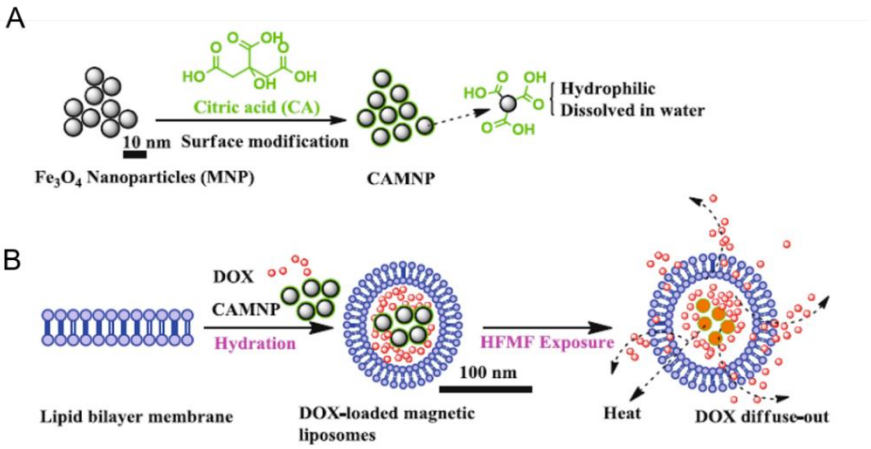

Figure 1.9. Magnetite nanoparticles coating with citric acid (A) and their encapsulation along with doxorubicin in liposomes (B). Upon high frequency magnetic field exposure, the heat absorption triggers the DOX release. Reproduced from [68].

The preparation methods of superparamagnetic nanoparticles containing iron or nickel are of great importance, because they determine the particles final shape, size distribution, surface chemistry and magnetic properties which, in turn, reflect the entire system behavior [71]. Nickel nanoparticles show interesting magnetic properties at room temperature, but they are associated with potential toxicity and high reactivity, so coating with silica or use of nickel ferrites is needed. For this purpose, nickel/silica core/shell nanoparticles synthesized by microheterogeneous templating have been developed [71] as well as nickel ferrite nanoparticles prepared by coprecipitation method [72]. These nanoparticles were then encapsulated in liposomes or covered with lipid bilayers, to form aqueous or solid magnetoliposomes, respectively, both with sizes lower than 100 nm.

Besides these examples, manganese ferrite nanoparticles are of great interest for magnetic drug targeting, as they have high magnetic susceptibility and show high biocompatibility and low toxicity in healthy cells [73]. Rodrigues *et al.* [73,74] developed magnetoliposomes, both AMLs and SMLs, successfully incorporating antitumor thienopyridine derivates, with preserved superparamagnetic properties and capable of inducing cancer cell death. Magnetoliposomes containing magnesium ferrite nanoparticles were also developed to deliver curcumin, which has anti-inflammatory and anticancer properties, overcoming its low solubility and poor bioavailability [75]. Magnetoliposomes containing iron oxide nanoparticles like magnetite have been the most used for biomedical applications because of their biocompatibility, low toxicity, higher specific absorption rate as well as higher saturation magnetization than the ones observed for nickel ferrite and manganese ferrite nanoparticles, showing an efficient

synergistic effect of chemotherapy and magnetic hyperthermia against highly metastatic cancer cells [76,77].

Along with magnetic drug delivery, the binding of specific ligands to the surface of magnetoliposomes can enhance selectivity to the target tissue, reducing side effects of drugs in circulation and increasing their concentration at the treatment site. Recently, an innovative nanosystem was developed, which is composed by magnetoliposomes incorporating magnetite nanoparticles in the aqueous core and a heat-shock protein (HSP90) inhibitor, 7-allylamio-17-desmethoxygeldanamycin (17-AAG), in the lipid bilayer. The liposome was coated with PEG and folic acid (FA), the latter having high affinity for folate receptor (FR) that is overexpressed in tumor tissues. This system has shown to be more effective to bind and enter in tumor cells and capable of enhance the hyperthermia effect as the HSP90 inhibitor sensitizes the cancer cells to heat without affecting normal cells [78].

1.6. Lactoferrin – a multifunctional protein

Lactoferrin (Lf) is an 80 kDa iron-binding glycoprotein of the transferrin family, produced by mucosal epithelial cells or neutrophils during inflammation processes, which is also present in several biological fluids like saliva, tears, sweat and, in great abundance, in milk [79,80]. Lactoferrin has been described as a multifunctional protein [81], as it is involved in immunomodulatory processes and exhibits antibacterial [79-84], anti-viral [80], antifungal [85-87], anticancer activities [88-90], among others.

1.6.1. Antimicrobial activity of lactoferrin

The bioinorganic structure of lactoferrin enables the performance of several important functions like iron transportation and immune defense. The strong binding force of lactoferrin to iron ($K_d \sim 10^{-20}$ mol/L) allows the local privation of this element avoiding bacterial growth and the formation of biofilms by competition with bacterial siderophores [80]. Interestingly, lactoferrin contains a highly cationic N-terminal region, due to the presence of arginine and lysine residues that interact with lipopolysaccharides, glycosaminoglycans and DNA [80]. Upon cleavage of lactoferrin by pepsin in the stomach, different peptides with even stronger activity are produced, such as lactoferricins, which promote dissipation of the membrane electrical potential in *E. coli,* loss of pH gradient and subsequent cell death. However, the mechanisms of action responsible for the antimicrobial activity of lactoferrin are still being investigated. The anti-fungal activity of lactoferrin was tested *in vitro* in *Candida albicans* cells by Viejo-Díaz *et al.* [86],

in order to understand the mechanism of action and optimal conditions of lactoferrin activity. From these studies, it was possible to conclude that lactoferrin induces an efflux of K^+ ions, a decrease in the cytoplasmic pH and promotes membrane depolarization.

Andrés *et al.* [87] investigated a possible correlation between K^+ efflux and apoptotic cell death. In this study, *C. albicans* cells treated with human lactoferrin showed a set of apoptotic markers such as DNA degradation, phosphatidylserine externalization, mitochondrial membrane depolarization and reactive oxygen species (ROS) production. The results show a dependence between cell death and intracellular accumulation of ROS induced by lactoferrin and loss of mitochondrial membrane potential, indicating a key role of mitochondria in this death process. It was also shown that treatment with lactoferrin induces an efflux of K^+ ions mediated by K^+ channels (present in yeast) that triggers apoptosis in *C. albicans* cells. Later, Andrés *et al.* [84] studied the antimicrobial activity of lactoferrin and transferrin in *Pseudomonas aeruginosa* and *Lactococcus lactis* cells, with the aim of finding a common target of transferrins. These two types of bacteria undergo different mechanisms of proton gradient maintenance (ΔpH) and intracellular pH regulation (pH_i). The study of metabolic conditions allowed to find that the antibacterial effect of lactoferrin and transferrin depends on the cytoplasmic pH and metabolic pathway (aerobic or anaerobic) of the cells but does not depend on the cellular energetic state. Membrane permeabilization tests and electric potential assays were performed, showing a disruption of the plasma membrane and the lack of membrane potential when comparing with cells treated with a specific inhibitor of H^+-ATPase. This led to the assumption that the common target for lactoferrin was the proton efflux that generates a proton motion force and intracellular pH regulation, which both, depend on the activity of H^+-ATPase complex. Thus, two hypotheses were proposed for the mechanism of action of lactoferrin in H^+-ATPase (figure 1.10): (1) In *L. lactis* cells, intracellular pH regulation depends on proton pumping to the extracellular environment, and its inhibition by lactoferrin promotes a decrease of the intracellular pH, leading to cell death; (2) In *P. aeruginosa* cells, inhibition of the ATPase by lactoferrin induces the accumulation of protons in the periplasmatic space leading to cell death.

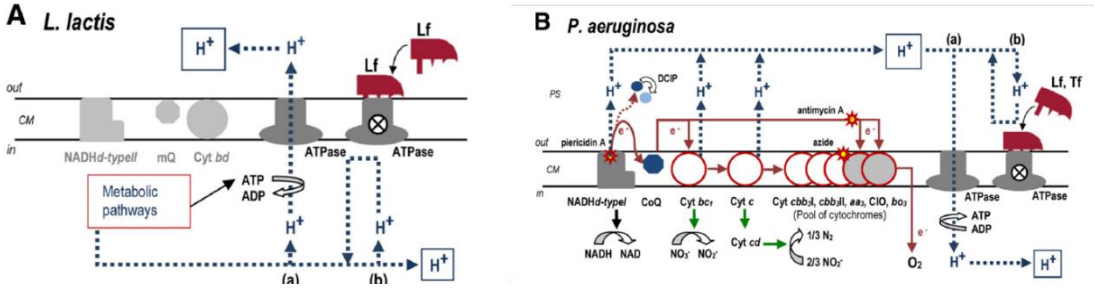

Figure 1.10. Possible mechanisms of action of lactoferrin and transferrin in the ATPase complex of *L. lactis* (A) and *P. aeruginosa* (B). Reproduced from Andrés *et al.* [84].

The interest in the apoptotic cell death induced by lactoferrin led to a further research on this subject. Acosta-Zaldívar *et al.* [91] studied the effect of lactoferrin in *Saccharomyces cerevisiae* to unveil the associated molecular mechanisms. The results showed that cells without metacaspase Yca1p were more resistant to lactoferrin than the wild type cells, suggesting the dependence on the metacaspase activation in the cell death induced by lactoferrin. Additionally, lactoferrin was found to induce several apoptotic markers such as chromatin condensation, while preserving plasma membrane integrity, ROS accumulation and release of cytochrome *c* to the cytosol. Later on, Pma1p, a P_{3A}-type ATPase, was identified as a specific target of lactoferrin [85]. As mentioned before, the control of intracellular pH is imperative for cell survival and depends on the transmembrane proton flux regulated by P-type ATPases, present in the plasma membrane, which translocate protons to the extracellular environment, and in the case of eukaryotes by V-type ATPases, that transport protons to the vacuolar/lysossomal lumen. Pma1p protein couples ATP hydrolysis to the extrusion of protons generating an electrochemical gradient that is essential to cellular homeostasis. The above-mentioned study demonstrated that lactoferrin decreased Pma1p activity, inhibiting proton pumping out of cell membrane, increased mitochondrial ATP production, and ultimately caused a perturbation in ionic homeostasis leading to cell death (figure 1.11). Two pathways associated with the inhibition of proton pump Pma1p by lactoferrin were anticipated: (1) cytoplasmic ionic events where intracellular accumulation of protons and subsequent decrease of intracellular pH promotes an efflux of K^+ ions out of the cell through potassium channels present in the cytoplasmic membrane; (2) mitochondrial ionic events where the loss of K^+ ions in mitochondrial matrix will lead to protons entry through mitochondrial ATPase, causing an increased production of ATP. Besides that, the established cytoplasmic and mitochondrial K^+/H^+ loop can trigger non-ionic events of apoptotic cell death. Summarising, the abovementioned studies allowed to conclude that lactoferrin induces an apoptosis-like phenotype in yeast associated with K^+-channel-mediated K^+ efflux, mitochondrial depolarization, intracellular ROS accumulation and inhibition of the H^+-ATPases (F-type ATPases and P-type ATPases), which causes a decrease of the intracellular pH, leading to cell death. Since lactoferrin is cytotoxic to yeast cells, new therapy approaches can be thought and designed to use this protein for the treatment of infections caused by *C. albicans* or even *S. cerevisiae* in immunocompromised patients, so, in this work, we tested lactoferrin-loaded magnetoliposomes against *S. cerevisiae* cells.

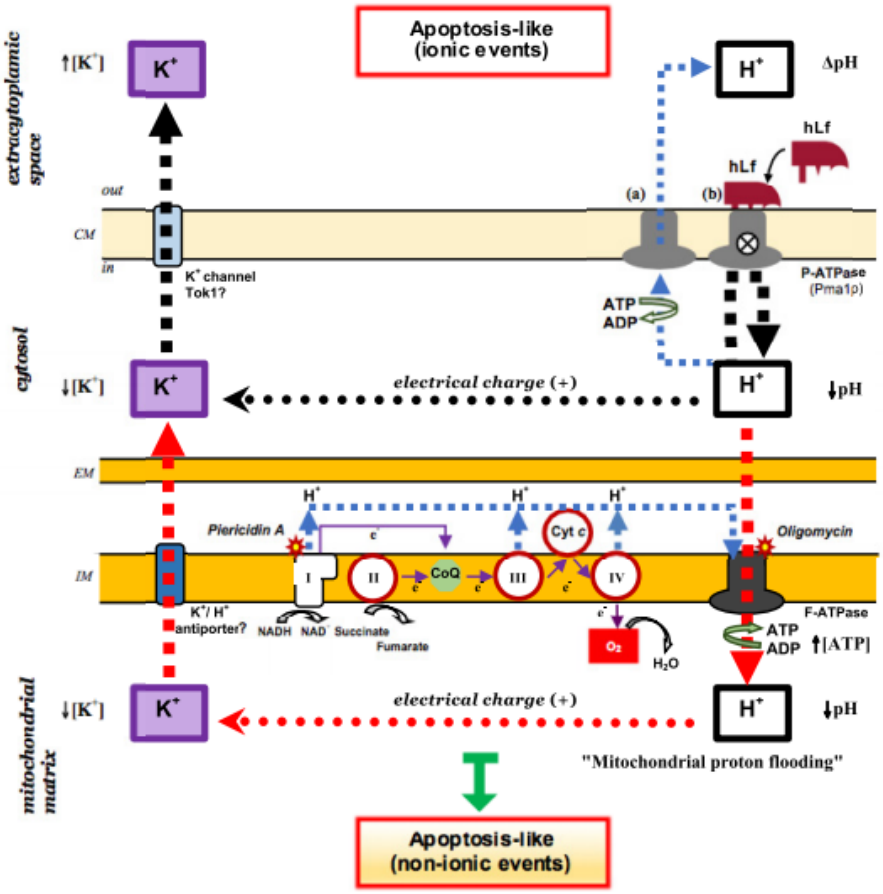

Figure 1.11. Schematic representation of the hypothesized mechanism of yeast apoptotic cell death induced by lactoferrin. (a) H^+-ATPase Pma1p; (b) inhibition of Pma1p by lactoferrin. Reproduced from [85].

1.6.2. Anticancer activity of lactoferrin

Despite the anti-fungal and antibacterial activities of lactoferrin, several *in vitro* and *in vivo* studies had already confirmed the anticancer potential of lactoferrin added extracellularly, which is capable of inhibiting tumor cells growth and reducing susceptibility to cancer, through cell cycle inhibition and induction of apoptosis [88]. In addition, the expression of lactoferrin gene is reduced in cancer cells and its overexpression can lead to their growth inhibition [92]. Cationic peptides derived from lactoferrin, like lactoferricin B, can induce mitochondrial membrane disruption and selectively attack tumor cells with more impact than the native protein [88]. Lactoferrin can block cell cycle in four different types of breast cancer cell lines (T-47D, MDA-MB-231, Hs578T and MCF-7) without affecting normal cells, indicating the selectivity of this protein to cancer cells [93]. Lactoferrin inhibits cell cycle progression in different cell

cycle phases depending on the cell type, but in all studies a decrease of cells in S phase, was observed, demonstrating the anti-proliferative activity of lactoferrin. Gibbons *et al.* [94] tested the effect of iron saturation in bovine lactoferrin (bLf) activity by studying the effect of apo-bLf (without Fe^{3+}) and Fe-bLf (>90% Fe^{3+}) against two breast cancer cell lines (MDA-MB-231 and MCF-7). Apo-bLf promoted higher cytotoxicity than Fe-bLf, which was associated with a decrease of cell proliferation and induction of apoptosis without affecting normal breast cells. The higher efficiency of apo-bLf is possibly due to its chelating properties, thus perturbating the normal iron metabolism function in breast cancer cells. The anticancer activity of apo-bLf and diferric-bLf was investigated in human epithelial cancer cells (HeLa) by Luzi *et al.* [95]. Diferric-bLf did not present effect in the concentration range tested (from 1 to 12.5 μM), while apo-bLf induced apoptosis associated to chromatin condensation and activation of caspases. NAD^+ concentration has a major role in apoptosis induction, being involved in redox homeostasis and oxidative stress processes that can lead to cell death [96]. It was also demonstrated that apo-bLf decreases NAD^+ levels with subsequent ROS production and decrease of glutathione (GSH) levels, responsible for antioxidant protection. Thus, it can be assumed the dependence of these cellular components on the apoptosis induction of lactoferrin in this type of cells [95]. Thus, lactoferrin can have different antitumoral activities depending on its iron saturation state or type of cancer cell.

Vacuolar H^+-ATPase (V-H^+-ATPase) was identified as a target of lactoferrin in highly metastatic cancer cells. It is present in acidic organelles (and in the plasma membrane of highly metastatic cancer cells) and, is involved in the maintenance of the optimal conditions for cancer cells' survival, such as pH homeostasis, acquisition of metastatic properties and acidification of tumor microenvironment. This proton pump exhibits a higher activity in highly metastatic than poorly metastatic cancer cells, making it a potential therapeutic target [90]. Pereira *et al.* [97] demonstrated that bLf can induce a 50% decrease of cell proliferation in highly metastatic breast cancer cells (Hs 578T) without significantly affecting poorly metastatic (T-47D) and non-tumorigenic breast cell lines (MCF-10-2A). Immunofluorescence against the c' subunit of the V-H^+-ATPase showed that the cellular localization of this proton pump is different for the three cell lines, being only located at the plasma membrane of Hs 578T cells. This observation, along with the higher basal extracellular acidification rate of Hs 578T cells demonstrate the recruitment of the V-H^+-ATPase to the plasma membrane. Intracellular and extracellular pH measurements of cells treated with bLf demonstrated that bLf induces intracellular acidification and inhibition of cell proliferation only on the highly metastatic cancer cells and not on the lowly metastatic and non-tumorigenic cells. These results show the selectivity of lactoferrin to highly metastatic cancer cells and suggest an inhibitory

mechanism of V-H^+-ATPase activity (figure 1.12). In this work, the proposed molecular mechanism underlying lactoferrin anticancer activity was the following: bLf binds and inhibits plasmalemmal V-H^+-ATPase promoting an intracellular acidification leading to apoptosis; in addition, internalization of the intact protein or derived peptides can occur, inhibiting lysosomal V-H^+-ATPase. In any case, lactoferrin promotes the up-regulation of pro-apoptotic proteins or down-regulation of anti-apoptotic proteins [97]. Therefore, the low cytotoxicity for non-tumorigenic cells and the capacity to reduce the tumor microenvironment acidity make this protein a strong candidate to alternative therapies against breast cancer cells. In 2018, Guedes *et al.* [98] tested the activity of bLf against the highly metastatic prostate cancer PC-3 and osteosarcoma MG-63 cell lines and compared it with the breast cancer MDA-MB-231 and non-tumorigenic bj-5ta cell lines. They showed that the sensitivity of the three highly metastatic cell lines to bLf was related with higher levels of V-ATPase at the plasma membrane, and that bLf acts as a specific inhibitor of this proton pump inducing intracellular acidification and apoptosis.

Given the lactoferrin effective anticancer activity against highly metastatic cancer cells derived from breast cancer, in this work, the developed nanosystems were tested against the highly metastatic cancer cell line Hs 578T. As a control of normal breast cells, the non-tumorigenic cell line MCF-10-2A was also studied.

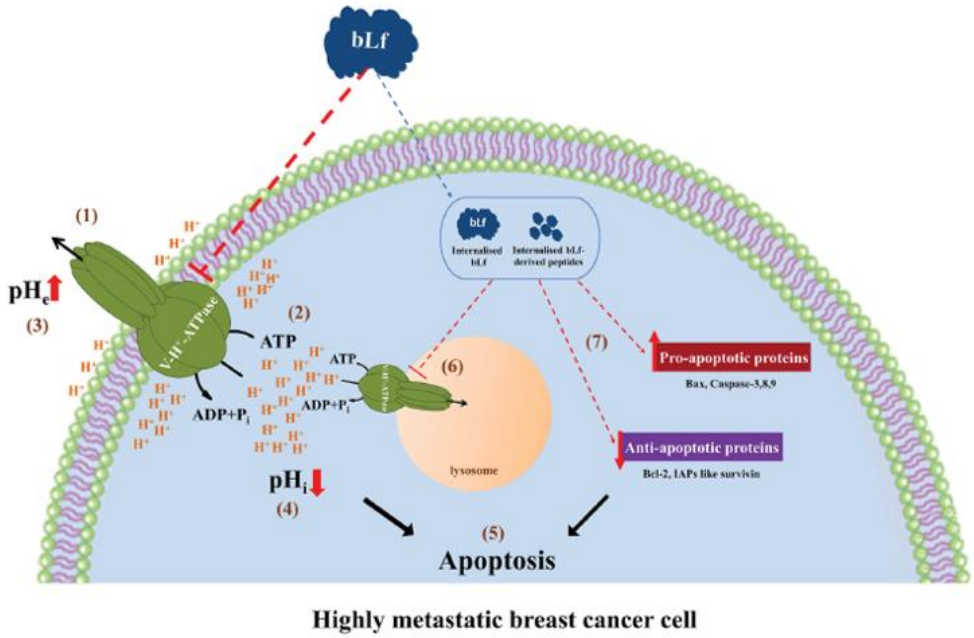

Figure 1.12. Hypothetical molecular mechanism of apoptotic induction of lactoferrin in highly metastatic breast cancer cells. (1) inhibition of V-H^+-ATPase proton pump by lactoferrin; (2) inhibition of hydrolytic activity of V-H^+-ATPase; (3) increase of extracellular pH due to blockage of proton extrusion; (4) intracellular acidification leading to apoptotic processes (5); (6) inhibition of lysosomal V-H^+-ATPase by lactoferrin and (7) modulation of apoptotic proteins that can lead to apoptosis. Reproduced from [97].

1.6.3. Lactoferrin delivery

As the study of therapeutic properties of lactoferrin grows, investigation focusing delivery systems incorporating this protein has been performed, to make possible its administration in patients in a non-invasive and painless way. Oral administration of lactoferrin has shown to be more effective than intravenous, subcutaneous and intraperitoneal ones, due to its safe use for a long period of time. However, this type of administration faces problems associated with proteolysis by digestive enzymes like pepsin and that issue must be considered [99]. Efficient transport systems are needed in order to deliver lactoferrin to its specific receptors and targets of interest. One possible strategy is encapsulation of lactoferrin in liposomes, increasing its permeability and absorption rate. The use of liposomes as lactoferrin delivery systems can increase uptake and accumulation of this protein in cancer cells, improving its anti-proliferative capacity [100,101]. Kanwar *et al.* [102] created a lactoferrin delivery system composed by a ceramic core of calcium phosphate covered with a thin film of chitosan and alginate shell (figure 1.13). When reaching small intestine, these alkaline nanocarriers are degraded and the alginate shell is released. Nanoparticles without alginate are absorbed by endocytosis entering the blood circulation and are delivered in tumor cells that have lactoferrin receptors for a specific binding.

The main advantage of being encapsulated in liposomes for oral administration is that lactoferrin is protected from gastrointestinal juices, maintaining its function until reaching target tissue. Lactoferrin can also be used as a specific ligand adsorbed to the liposomes surface [103,104]. Xu *et al.* [103] developed and tested lactoferrin modified PEGylated liposomes loaded with doxorubicin in hepatocellular carcinoma cells. Doxorubicin is the most used therapeutic agent for hepatocellular carcinoma treatment. However, it shows systemic toxicity that can be overcome with its encapsulation in a nanocarrier containing lactoferrin that selectively binds to asialoglycoprotein receptors (ASGRP), present in this type of cells. Functionalization of the surface of liposomes with lactoferrin can improve its uptake and therapeutic effect comparing to the bare or PEGylated ones. The improved therapeutic efficiency of lactoferrin when incorporated in nanocarriers, highlights the importance of a continuous research for new strategies capable of produce delivery nanosystems for different tissues where lactoferrin can act as a therapeutic agent.

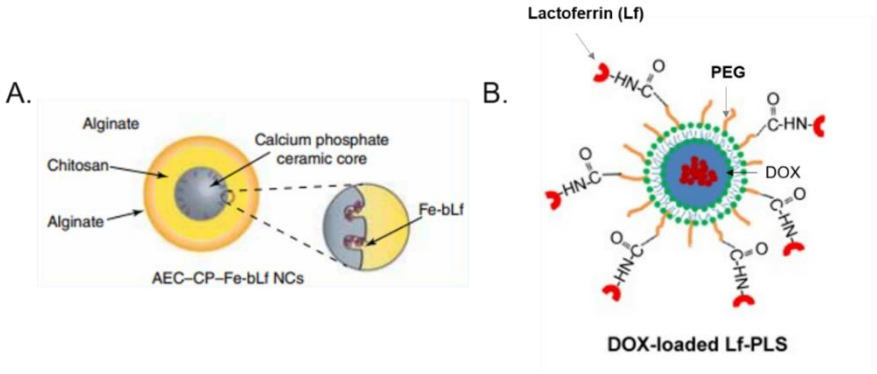

Figure 1.13. Schematic representation of AEC-CP-Fe-bLf nanocarriers (A) and lactoferrin modified PEGylated liposomes loaded with doxorubicin (DOX-loaded Lf-PLS) (B). A and B reproduced from [101] and [102], respectively.

1.7. References

[1] Singh, A. (2016). *Engineered nanoparticles*. 1st ed. Academic Press, 77-123.

[2] Khan, I., Saeed, K. and Khan, I. (2017). Nanoparticles: Properties, applications and toxicities. *Arabian Journal of Chemistry*, 1-24.

[3] Chen, G., Roy, I., Yang, C. and Prasad, P. (2016). Nanochemistry and Nanomedicine for Nanoparticle-based Diagnostics and Therapy. *Chemical Reviews*, 116, 2826-2885.

[4] Bhatia, S. (2016). *Natural Polymer Drug Delivery Systems: Nanoparticles, plants and algae.* 1st ed. Springer, 33-93.

[5] Cho, K., Wang, X., Nie, S., Chen, Z. and Shin, D. (2008). Therapeutic Nanoparticles for Drug Delivery in Cancer. *Clinical Cancer Research*, 14, 1310-1316.

[6] Wagner, V., Dullaart, A., Bock, A. and Zweck, A. (2006). The emerging nanomedicine landscape. *Nature Biotechnology*, 24, 211-1217.

[7] Riehemann, K., Schneider, S., Luger, T., Godin, B., Ferrari, M. and Fuchs, H. (2009). Nanomedicine-Challenge and Perspectives. *Angewandte Chemie International Edition*, 48, 872-897.

[8] Kim, B., Rutka, J. and Chan, W. (2010). Nanomedicine. *New England Journal of Medicine*, 363, 2434-2443.

[9] Mout, R., Moyano, D., Rana, S. and Rotello, V. (2012). Surface functionalization of nanoparticles for nanomedicine. *Chemical Society Reviews*, 41, 2539-2544.

[10] Lammers, T., Aime, S., Hennink, W., Storm, G. and Kiessling, F. (2011). Theranostic Nanomedicine. *Accounts of Chemical Research*, 44, 1029-1038.

[11] Duncan, R. and Gaspar, R. (2011). Nanomedicine(s) under the Microscope. *Molecular Pharmaceutics*, 8, 2101-2141.

[12] Issa, B., Obaidat, I., Albiss, B. and Haik, Y. (2013). Magnetic Nanoparticles: Surface Effects and Properties Related to Biomedicine Applications. *International Journal of Molecular Sciences*, 14, 21266-21305.

[13] Indira, T. and Lakshmi, P. (2010). Magnetic Nanoparticles - A Review. *International Journal of Pharmaceutical Sciences and Nanotechnology*, 3, 1035 - 1042.

[14] Zhu, K., Ju, Y., Xu, J., Yang, Z., Gao, S. and Hou, Y. (2018). Magnetic Nanomaterials: Chemical Design, Synthesis, and Potential Applications. *Accounts of Chemical Research*, 51, 404-413.

[15] Kolhatkar, A., Jamison, A., Litvinov, D., Willson, R. and Lee, T. (2013). Tuning the Magnetic Properties of Nanoparticles. *International Journal of Molecular Sciences*, 14, 15977-16009.

[16] Akbarzadeh, A., Samiei, M. and Davaran, S. (2012). Magnetic nanoparticles: preparation, physical properties, and applications in biomedicine. *Nanoscale Research Letters*, 7, 1-13.

[17] Yang, C., Hou, Y. and Gao, S. (2014). Nanomagnetism: Principles, nanostructures, and biomedical applications. *Chinese Physics B*, 23, 1-8.

[18] Thanh, N. (2012). *Magnetic nanoparticles*. 1st ed. CRC Press, 19-46.

[19] Gupta, A., Naregalkar, R., Vaidya, V. and Gupta, M. (2007). Recent advances on surface engineering of magnetic iron oxide nanoparticles and their biomedical applications. *Nanomedicine*, 2, 23-39.

[20] Khanna, L. and Verma, N. (2013). Synthesis, characterization and in vitro cytotoxicity study of calcium ferrite nanoparticles. *Materials Science in Semiconductor Processing*, 16, 1842-1848.

[21] Mahmoudi, M., Sant, S., Wang, B., Laurent, S. and Sen, T. (2011). Superparamagnetic iron oxide nanoparticles (SPIONs): Development, surface modification and applications in chemotherapy. *Advanced Drug Delivery Reviews*, 63, 24-46.

[22] Ali, A., Zafar, H., Zia, M., ul Haq, I., Phull, A., Ali, J. and Hussain, A. (2019). Synthesis, characterization, applications, and challenges of iron oxide nanoparticles. *Nanotechnology, science and applications*, 19, 46-67.

[23] Wu, W., He, Q. and Jiang, C. (2008). Magnetic Iron Oxide Nanoparticles: Synthesis and Surface Functionalization Strategies. *Nanoscale Research Letters*, 3, 397-415.

[24] Sun, S., Wei, C., Zhu, Z., Hou, Y., Venkatraman, S. and Xu, Z. (2014). Magnetic iron oxide nanoparticles: Synthesis and surface coating techniques for biomedical applications. *Chinese Physics B*, 23, 1-19.

[25] Dong, C., Wang, G., Shi, L., Guo, D., Jiang, C. and Xue, D. (2012). Investigation of the thermal stability of Mn ferrite particles synthesized by a modified co-precipitation method. *Science China Physics, Mechanics and Astronomy*, 56, 568-572.

[26] Doaga, A., Cojocariu, A., Amin, W., Heib, F., Bender, P., Hempelmann, R. and Caltun, O. (2013). Synthesis and characterizations of manganese ferrites for hyperthermia applications. *Materials Chemistry and Physics*, 143, 305-310.

[27] Wu, W., Wu, Z., Yu, T., Jiang, C. and Kim, W. (2015). Recent progress on magnetic iron oxide nanoparticles: synthesis, surface functional strategies and biomedical applications. *Science and Technology of Advanced Materials*, 16, 1-43.

[28] Mout, R., Moyano, D., Rana, S. and Rotello, V. (2012). Surface functionalization of nanoparticles for nanomedicine. *Chemical Society Reviews*, 41, 2539-2544.

[29] Tran, N. and Webster, T. (2010). Magnetic nanoparticles: biomedical applications and challenges. *Journal of Materials Chemistry*, 20, 8760-8767.

[30] Fang, J. (2015). Enhanced permeability and retention effect based nanomedicine, a solution for cancer. *World Journal of Pharmacology*, 4, 168-171.

[31] Greish, K. (2012). Enhanced permeability and retention effect for selective targeting of anticancer nanomedicine: are we there yet? *Drug Discovery Today: Technologies*, 9, 161-166.

[32] Singh, A. and Sahoo, S. (2014). Magnetic nanoparticles: a novel platform for cancer theranostics. *Drug Discovery Today*, 19, 474-481.

[33] Cole, A., Yang, V. and David, A. (2011). Cancer theranostics: the rise of targeted magnetic nanoparticles. *Trends in Biotechnology*, 29, 323-332.

[34] Revia, R. and Zhang, M. (2016). Magnetite nanoparticles for cancer diagnosis, treatment, and treatment monitoring: recent advances. *Materials Today*, 19, 157-168.

[35] Sahoo, B., Devi, K., Dutta, S., Maiti, T., Pramanik, P. and Dhara, D. (2014). Biocompatible mesoporous silica-coated superparamagnetic manganese ferrite nanoparticles for targeted drug delivery and MR imaging applications. *Journal of Colloid and Interface Science*, 431, 31-41.

[36] Yadollahpour, A., Asl, H. and Rashidi, S. (2017). Applications of Nanoparticles in Magnetic Resonance Imaging: A Comprehensive Review. *Asian Journal of Pharmaceutics*, 11, 1-7.

[37] Vuong, Q., Gillis, P., Roch, A. and Gossuin, Y. (2017). Magnetic resonance relaxation induced by superparamagnetic particles used as contrast agents in magnetic resonance imaging: a theoretical review. *Wiley Interdisciplinary Reviews: Nanomedicine and Nanobiotechnology*, 9, 1-22.

[38] Bao, Y., Sherwood, J. and Sun, Z. (2018). Magnetic iron oxide nanoparticles as T_1 contrast agents for magnetic resonance imaging. *Journal of Materials Chemistry C*, 6, 1280-1290.

[39] Tromsdorf, U., Bruns, O., Salmen, S., Beisiegel, U. and Weller, H. (2009). A Highly Effective, nontoxic T_1 MR Contrast Agent Based on Ultrasmall PEGylated Iron Oxide Nanoparticles. *Nano Letters*, 9, 4434-4440.

[40] Taboada, E., Rodríguez, E., Roig, A., Oró, J., Roch, A. and Muller, R. (2007). Relaxometric and Magnetic Characterization of Ultrasmall Iron Oxide Nanoparticles with High Magnetization. Evaluation as Potential T_1 Magnetic Resonance Imaging Contrast Agents for Molecular Imaging. *Langmuir*, 23, 4583-4588.

[41] Huang, G., Li, H., Chen, J., Zhao, Z., Yang, L., Chi, X., Chen, Z., Wang, X. and Gao, J. (2014). Tunable T_1 and T_2 contrast abilities of manganese-engineered iron oxide nanoparticles through size control. *Nanoscale*, 6, 10404-10412.

[42] Fortin, J., Gazeau, F. and Wilhelm, C. (2007). Intracellular heating of living cells through Néel relaxation of magnetic nanoparticles. *European Biophysics Journal*, 37, 223-228.

[43] Makridis, A., Topouridou, K., Tziomaki, M., Sakellari, D., Simeonidis, K., Angelakeris, M., Yavropoulou, M., Yovos, J. and Kalogirou, O. (2014). In vitro application of Mn-ferrite nanoparticles as novel magnetic hyperthermia agents. *J. Mater. Chem. B*, 2, 8390-8398.

[44] Hervault, A. and Thanh, N. (2014). Magnetic nanoparticle-based therapeutic agents for thermo-chemotherapy treatment of cancer. *Nanoscale*, 6, 11553-11573.

[45] Arruebo, M., Fernández-Pacheco, R., Ibarra, M. and Santamaría, J. (2007). Magnetic nanoparticles for drug delivery. *Nano Today*, 2, 22-32.

[46] Veiseh, O., Gunn, J. and Zhang, M. (2010). Design and fabrication of magnetic nanoparticles for targeted drug delivery and imaging. *Advanced Drug Delivery Reviews*, 62, 284-304.

[47] Sun, C., Du, K., Fang, C., Bhattarai, N., Veiseh, O., Kievit, F., Stephen, Z., Lee, D., Ellenbogen, R., Ratner, B. and Zhang, M. (2010). PEG-Mediated Synthesis of Highly Dispersive Multifunctional Superparamagnetic Nanoparticles: Their Physicochemical Properties and Function In Vivo. *ACS Nano*, 4, 2402-2410.

[48] De Jong, W. and Borm, P. (2008). Drug delivery and nanoparticles: Applications and hazards. *International Journal of Nanomedicine*, 3, 133-149.

[49] Alavi, M., Karimi, N. and Safaei, M. (2017). Application of Various Types of Liposomes in Drug Delivery Systems. *Advanced Pharmaceutical Bulletin*, 7, 3-9.

[50] Grimaldi, N., Andrade, F., Segovia, N., Ferrer-Tasies, L., Sala, S., Veciana, J. and Ventosa, N. (2016). Lipid-based nanovesicles for nanomedicine. *Chemical Society Reviews*, 45, 6520-6545.

[51] Bangham, A., Standish, M. and Watkins, J. (1965). Diffusion of univalent ions across the lamellae of swollen phospholipids. *Journal of Molecular Biology*, 13, 238-IN27.

[52] Bozzuto, G. and Molinari, A. (2019). Liposomes as nanomedical devices. *International Journal of Nanomedicine*, 10, 975-999.

[53] Akbarzadeh, A., Rezaei-Sadabady, R., Davaran, S., Joo, S., Zarghami, N., Hanifehpour, Y., Samiei, M., Kouhi, M. and Nejati-Koshki, K. (2013). Liposome: classification, preparation, and applications. *Nanoscale Research Letters*, 8, 1-9.

[54] Szoka, F. and Papahadjopoulos, D. (1978). Procedure for preparation of liposomes with large internal aqueous space and high capture by reverse-phase evaporation. *Proceedings of the National Academy of Sciences*, 75, 4194-4198.

[55] Li, J., Wang, X., Zhang, T., Wang, C., Huang, Z., Luo, X. and Deng, Y. (2019). A review on phospholipids and their main applications in drug delivery systems. *Asian Journal of pharmaceutical sciences*, 10, 81-98.

[56] Torchilin, V. (2005). Recent advances with liposomes as pharmaceutical carriers. *Nature Reviews Drug Discovery*, 4, 145-160.

[57] Gabizon, A. (2001). Pegylated Liposomal Doxorubicin: Metamorphosis of an Old Drug into a New Form of Chemotherapy. *Cancer Investigation*, 19, 424-436.

[58] Lu, Y. and Low, P. (2002). Folate-mediated delivery of macromolecular anticancer therapeutic agents. *Advanced Drug Delivery Reviews*, 54, 675-693.

[59] Ishida, O., Maruyama, K., Tanahashi, H., Iwatsuru, M., Sasaki, K., Eriguchi, M. and Yanagie, H. (2001). Liposomes bearing polyethyleneglycol-coupled transferrin with intracellular targeting property to the solid tumors in vivo. *Pharmaceutical Research*, 18, 1042-1048.

[60] Sriraman, S., Salzano, G., Sarisozen, C. and Torchilin, V. (2016). Anti-cancer activity of doxorubicin-loaded liposomes co-modified with transferrin and folic acid. *European Journal of Pharmaceutics and Biopharmaceutics*, 105, 40-49.

[61] Haemmerich, D. and Motamarry, A. (2018). Thermosensitive Liposomes for Image-Guided Drug Delivery. *Advances in Cancer Research*, 139, 121-146.

[62] Lee, J., Park, H., Oh, K. and Lee, E. (2018). pH-Responsive hyaluronated liposomes for docetaxel delivery. *International Journal of Pharmaceutics*, 547, 377-384.

[63] Soenen, S., Velde, G., Ketkar-Atre, A., Himmelreich, U. and De Cuyper, M. (2011). Magnetoliposomes as magnetic resonance imaging contrast agents. Wiley Interdisciplinary Reviews: *Nanomedicine and Nanobiotechnology*, 3, 197-211.

[64] Fattahi, H., Laurent, S., Liu, F., Arsalani, N., Elst, L. and Muller, R. (2011). Magnetoliposomes as multimodal contrast agents for molecular imaging and cancer nanotheragnostics. *Nanomedicine*, 6, 529-544.

[65] Martina, M., Fortin, J., Fournier, L., Ménager, C., Gazeau, F., Clément, O. and Lesieur, S. (2007). Magnetic Targeting of Rhodamine-Labeled Superparamagnetic Liposomes to Solid Tumors: In Vivo Tracking by Fibered Confocal Fluorescence Microscopy. *Molecular Imaging*, 6, 140-146.

[66] Pradhan, P., Giri, J., Rieken, F., Koch, C., Mykhaylyk, O., Döblinger, M., Banerjee, R., Bahadur, D. and Plank, C. (2010). Targeted temperature sensitive magnetic liposomes for thermo-chemotherapy. *Journal of Controlled Release*, 142, 108-121.

[67] Salvatore, A., Montis, C., Berti, D. and Baglioni, P. (2016). Multifunctional Magnetoliposomes for Sequential Controlled Release. *ACS Nano*, 10, 7749-7760.

[68] Kulshrestha, P., Gogoi, M., Bahadur, D. and Banerjee, R. (2012). In vitro application of paclitaxel loaded magnetoliposomes for combined chemotherapy and hyperthermia. *Colloids and Surfaces B: Biointerfaces*, 96, 1-7.

[69] Joniec, A., Sek, S. and Krysinski, P. (2016). Magnetoliposomes as Potential Carriers of Doxorubicin to Tumours. *Chemistry - A European Journal*, 22, 17715-17724.

[70] Hardiansyah, A., Huang, L., Yang, M., Liu, T., Tsai, S., Yang, C., Kuo, C., Chan, T., Zou, H., Lian, W. and Lin, C. (2014). Magnetic liposomes for colorectal cancer cells therapy by high-frequency magnetic field treatment. *Nanoscale Research Letters*, 9, 1-13.

[71] Rodrigues, A., Gomes, I., Almeida, B., Araújo, J., Castanheira, E. and Coutinho, P. (2014). Magnetoliposomes based on nickel/silica core/shell nanoparticles: Synthesis and characterization. *Materials Chemistry and Physics*, 148, 978-987.

[72] Rodrigues, A., Gomes, I., Almeida, B., Araújo, J., Castanheira, E. and Coutinho, P. (2015). Magnetic liposomes based on nickel ferrite nanoparticles for biomedical applications. *Physical Chemistry Chemical Physics*, 17, 18011-18021.

[73] Rodrigues, A., Ramos, J., Gomes, I., Almeida, B., Araújo, J., Queiroz, M., Coutinho, P. and Castanheira, E. (2016). Magnetoliposomes based on manganese ferrite nanoparticles as nanocarriers for antitumor drugs. *RSC Advances*, 6, 17302-17313.

[74] Rodrigues, A., Almeida, B., Rodrigues, J., Queiroz, M., Calhelha, R., Ferreira, I., Pires, A., Pereira, A., Araújo, J., Coutinho, P. and Castanheira, E. (2017). Magnetoliposomes as carriers for promising antitumor thieno[3,2-b]pyridin-7-arylamines: photophysical and biological studies. *RSC Advances*, 7, 15352-15361.

[75] Cardoso, B., Rio, I., Rodrigues, A., Fernandes, F., Almeida, B., Pires, A., Pereira, A., Araújo, J., Castanheira, E. and Coutinho, P. (2018). Magnetoliposomes containing magnesium ferrite nanoparticles as nanocarriers for the model drug curcumin. *Royal Society Open Science*, 5, 1-15.

[76] Tartaj, P., Morales, M., Veintemillas-Verdaguer, S., Gonz lez-Carre o, T. and Serna, C. (2003). The preparation of magnetic nanoparticles for applications in biomedicine. *Journal of Physics D: Applied Physics*, 36, 182-197.

[77] Rodrigues, A., Mendes, P., Silva, P., Machado, V., Almeida, B., Araújo, J., Queiroz, M., Castanheira, E. and Coutinho, P. (2017). Solid and aqueous magnetoliposomes as nanocarriers for a new potential drug active against breast cancer. *Colloids and Surfaces B: Biointerfaces*, 158, 460-468.

[78] Wang, X., Yang, R., Yuan, C., An, Y., Tang, Q. and Chen, D. (2018). Preparation of Folic Acid-Targeted Temperature-Sensitive Magnetoliposomes and their Antitumor Effects In Vitro and In Vivo. *Targeted Oncology*, 13, 1-14.

[79] Ammons, M. and Copié, V. (2013). Mini-review: Lactoferrin: a bioinspired, anti-biofilm therapeutic. *Biofouling*, 29, 443-455.

[80] Vogel, H. (2012). Lactoferrin, a bird's eye view. *Biochemistry and Cell Biology*, 90, 233-244.

[81] Moreno-Expósito, L., Illescas-Montes, R., Melguizo-Rodríguez, L., Ruiz, C., Ramos-Torrecillas, J. and de Luna-Bertos, E. (2018). Multifunctional capacity and therapeutic potential of lactoferrin. *Life Sciences*, 195, 61-64.

[82] Hwang, P., Zhou, N., Shan, X., Arrowsmith, C. and Vogel, H. (1998). Three-Dimensional Solution Structure of Lactoferricin B, an Antimicrobial Peptide Derived from Bovine Lactoferrin. *Biochemistry*, 37, 4288-4298.

[83] Viejo-Díaz, M., Andrés, M., Pérez-Gil, J., Sánchez, M. and Fierro, J. (2003). Potassium Efflux Induced by a New Lactoferrin-Derived Peptide Mimicking the Effect of Native Human Lactoferrin on the Bacterial Cytoplasmic Membrane. *Biochemistry (Moscow)*, 68, 217-227.

[84] Andrés, M. and Fierro, J. (2010). Antimicrobial Mechanism of Action of Transferrins: Selective Inhibition of H^+-ATPase. *Antimicrobial Agents and Chemotherapy*, 54, 4335-4342.

[85] Andrés, M., Acosta-Zaldívar, M. and Fierro, J. (2016). Antifungal Mechanism of Action of Lactoferrin: Identification of H^+-ATPase (P_3A-Type) as a New Apoptotic-Cell Membrane Receptor. *Antimicrobial Agents and Chemotherapy*, 60, 4206-4216.

[86] Viejo-Díaz, M., Andrés, M. and Fierro, J. (2004). Modulation of In Vitro Fungicidal Activity of Human Lactoferrin against *Candida albicans* by Extracellular Cation Concentration and Target Cell Metabolic Activity. *Antimicrobial Agents and Chemotherapy*, 48, 1242-1248.

[87] Andrés, M., Viejo-Díaz, M. and Fierro, J. (2008). Human Lactoferrin Induces Apoptosis-Like Cell Death in *Candida albicans*: Critical Role of K^+-Channel-Mediated K^+ Efflux. *Antimicrobial Agents and Chemotherapy*, 52, 4081-4088.

[88] Zhang, Y., Lima, C. and Rodrigues, L. (2014). Anticancer effects of lactoferrin: underlying mechanisms and future trends in cancer therapy. *Nutrition Reviews*, 72, 763-773.

[89] Mader, J. (2005). Bovine lactoferricin selectively induces apoptosis in human leukemia and carcinoma cell lines. *Molecular Cancer Therapeutics*, 4, 612-624.

[90] Sennoune, S., Bakunts, K., Martínez, G., Chua-Tuan, J., Kebir, Y., Attaya, M. and Martínez-Zaguilán, R. (2004). Vacuolar H^+-ATPase in human breast cancer cells with distinct metastatic potential: distribution and functional activity. *American Journal of Physiology-Cell Physiology*, 286, 1443-1452.

[91] Acosta-Zaldívar, M., Andrés, M., Rego, A., Pereira, C., Fierro, J. and Côrte-Real, M. (2015). Human lactoferrin triggers a mitochondrial- and caspase-dependent regulated cell death in *Saccharomyces cerevisiae*. *Apoptosis*, 21, 163-173.

[92] Hoedt, E., Hardivillé, S., Mariller, C., Elass, E., Perraudin, J. and Pierce, A. (2010). Discrimination and evaluation of lactoferrin and delta-lactoferrin gene expression levels in cancer cells and under inflammatory stimuli using *TaqMan* real-time PCR. *BioMetals*, 23, 441-452.

[93] Zhang, Y., Nicolau, A., Lima, C. and Rodrigues, L. (2014). Bovine Lactoferrin Induces Cell Cycle Arrest and Inhibits Mtor Signaling in Breast Cancer Cells. *Nutrition and Cancer*, 66, 1371-1385.

[94] Gibbons, J., Kanwar, J. and Kanwar, R. (2015). Iron-free and iron-saturated bovine lactoferrin inhibit survivin expression and differentially modulate apoptosis in breast cancer. *BMC Cancer*, 15, 1-16.

[95] Luzi, C., Brisdelli, F., Iorio, R., Bozzi, A., Carnicelli, V., Di Giulio, A. and Lizzi, A. (2017). Apoptotic effects of bovine apo-lactoferrin on HeLa tumor cells. *Cell Biochemistry and Function*, 35, 33-41.

[96] Xia, W., Wang, Z., Wang, Q., Han, J., Zhao, C., Hong, Y., Zeng, L., Tang, L. and Ying, W. (2009). Roles of NAD^+/ NADH and $NADP^+$ / NADPH in Cell Death. *Current Pharmaceutical Design*, 15, 12-19.

[97] Pereira, C., Guedes, J., Gonçalves, M., Loureiro, L., Castro, L., Gerós, H., Rodrigues, L. and Côrte-Real, M. (2016). Lactoferrin selectively triggers apoptosis in highly metastatic breast cancer cells through inhibition of plasmalemmal V-H^+-ATPase. *Oncotarget*, 7, 1-15.

[98] Guedes, J., Pereira, C., Rodrigues, L. and Côrte-Real, M. (2018). Bovine Milk Lactoferrin Selectively Kills Highly Metastatic Prostate Cancer PC-3 and Osteosarcoma MG-63 Cells In Vitro. *Frontiers in Oncology*, 8, 1-12.

[99] Onishi, H. (2011). Lactoferrin delivery systems: approaches for its more effective use. *Expert Opinion on Drug Delivery*, 8, 1469-1479.

[100] Roseanu, A., Florian, P., Moisei, M., Sima, L., Evans, R. and Trif, M. (2010). Liposomalization of lactoferrin enhanced its anti-tumoral effects on melanoma cells. *BioMetals*, 23, 485-492.

[101] Guan, R., Ma, J., Wu, Y., Lu, F., Xiao, C., Jiang, H. and Kang, T. (2012). Development and characterization of lactoferrin nanoliposome: cellular uptake and stability. *Nanoscale Research Letters*, 7(1), 1-6.

[102] Kanwar, J., Mahidhara, G. and Kanwar, R. (2012). Novel alginate-enclosed chitosan–calcium phosphate-loaded iron-saturated bovine lactoferrin nanocarriers for oral delivery in colon cancer therapy. *Nanomedicine*, 7, 1521-1550.

[103] Xu, Y., Guo, X., Tu, L., Zou, Q., Li, Q., Tang, C., Chen, B., Wu, C. and Wei, M. (2015). Lactoferrin-modified PEGylated liposomes loaded with doxorubicin for targeting delivery to hepatocellular carcinoma. *International Journal of Nanomedicine*, 10, 1-15.

[104] Chen, H., Qin, Y., Zhang, Q., Jiang, W., Tang, L., Liu, J. and He, Q. (2011). Lactoferrin modified doxorubicin-loaded procationic liposomes for the treatment of gliomas. *European Journal of Pharmaceutical Sciences*, 44, 164-173.

Chapter 2 – Techniques of analysis and characterization

2.1. Electromagnetic radiation

The electromagnetic radiation is a form of energy that behaves as a wave and as particle at the same time and it is composed by an alternating electric field and a magnetic field that can be described by the electric field vector $\vec{E}$, and the magnetic field vector $\vec{B}$, respectively [1,2]. The two vectors have sinusoidal waves that oscillate in a plane perpendicular to the magnetic field with direction of wave propagation (figure 2.1) [1,2]. Being described as a wave, electromagnetic radiation can be characterized by physical quantities like frequency and wavelength, which are related by the following equation [1,2]:

$$\nu = \frac{c}{\lambda} \tag{2.1}$$

where ν is the wave frequency (s^{-1}), c is the speed of light ($3x10^8$ $m.s^{-1}$) and λ is the wavelength (m).

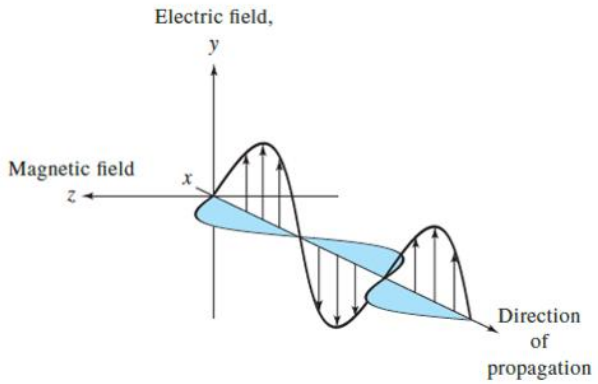

Figure 2.1. Schematic representation of propagation of electromagnetic radiation propagation. Reproduced from [1].

When radiation interacts with matter, processes like absorption, reflection, dispersion and luminescence can occur, which implies a discrete quantification of light. Therefore, it arises the need to consider light as particles, called photons. Photons energy, E, relates with wave frequency, ν, by equation 2.2 [1,2]:

$$E = h\nu = \frac{hc}{\lambda} \tag{2.2}$$

where h is Planck's constant ($6.6256x10^{-34}$ J.s).

From this equation, it can be inferred that shorter wavelengths are the more energetic and longer wavelengths have less energy. This relation can be graphically represented by an electromagnetic

spectrum, where the UV-visible region comprises the wavelength range of 200 to 700 nm (figure 2.2) [1,2].

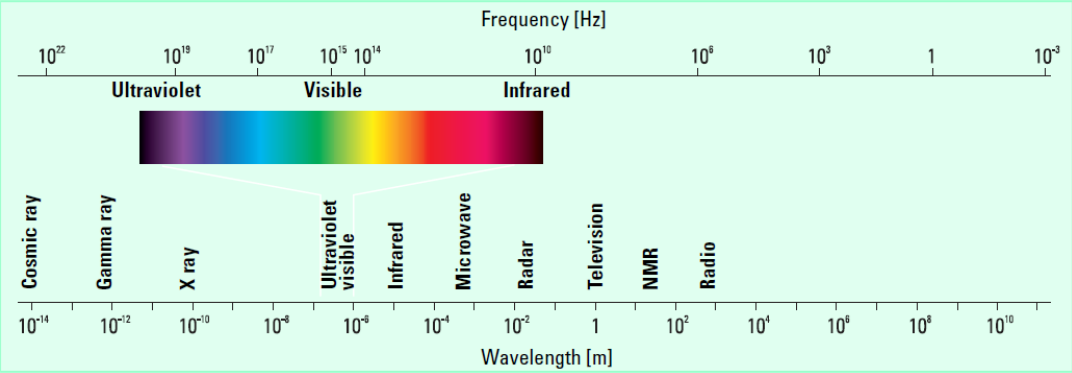

Figure 2.2. Representation of the electromagnetic spectrum. UV-Visible region is between wavelengths 200 to 700 nm. Besides UV and visible radiation, there is radiation with higher energy like X-ray, gamma-ray and others with less energy such as microwave and radio waves. Reproduced from [2].

2.2. UV-Visible spectroscopy

When electromagnetic radiation interacts with matter (solid, liquid or gas state), part of this radiation is selectively absorbed by molecules, that are promoted to a higher energy state or excited state. Atoms, molecules and ions have discrete energy levels with transition energies of the same order of magnitude as the UV-Visible radiation energy. If the photons energy, E, equals or is higher than the energy difference between the ground state and excited state of a molecule, ΔE, then the photon excites an electron from the ground state to a higher energy level, a process that is called absorption. The amount of energy that is absorbed can be calculated by the Bohr equation [1,2]:

$$\Delta E = E_1 - E_0 = h\nu \qquad (2.3)$$

Therefore, through absorption spectroscopy, it is possible to characterize a sample in terms of its chemical composition, as the absorbed frequencies are characteristic of a certain atom or group of atoms.

The total energy of a molecule includes the rotational energy, which comes from the rotation of the molecules around their centers of mass; vibrational energy, the result of vibrations between atoms or groups of atoms, and electronic energy that results from the motion of electrons around the nucleus. Each electronic state has a group of several rotational states, and the latter, in turn have several vibrational states [1,3]. Electronic transitions occur from the lower vibrational state to the excited state. Absorption spectra of molecules are composed of bands, each one correspondent to an electronic transition (figure 2.3). The peaks that compose these bands are related to the vibrational states that belong to each

electronic transition. Electronic transitions with lower energy have larger wavelengths and, in the contrary, the ones with higher energy have shorter wavelengths [1,3,4].

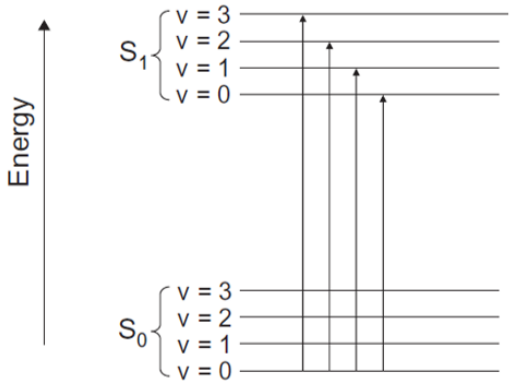

Figure 2.3. Schematic representation of electronic states (S_0, S_1) and respective vibrational energy levels (v=0, v=1, v=2, v=3) of a molecule. Reproduced from [4].

These electronic transitions occur from an occupied ground state to an empty excited state which is related to the existence of molecular orbitals: bonding (π and σ), non-bonding (n) and anti-bonding (π^* and σ^*). A σ bond can be formed from two s atomic orbitals, one s and one p atomic orbital or two p atomic orbitals that are aligned in the same symmetry axis [3]. A π bond is formed from two p atomic orbitals that are overlapped. The non-bonding orbitals are formed from non-bonding electrons of heteroatoms like oxygen and nitrogen (figure 2.4.A) [3].

In general, the energy of bonding orbitals is the lowest, followed by non-bonding orbitals and then anti-bonding orbitals with the highest energy. Possible energy transitions are represented in figure 2.4.B, however, not all transitions are allowed in the accessible UV region. The less probable transitions are $\sigma \rightarrow \sigma^*$ and $\pi \rightarrow \sigma^*$, because they require energies of vacuum UV. In UV-Vis spectroscopy, the most common transitions are from non-bonding or bonding orbitals n and π, respectively, to anti-bonding π^* orbitals ($n \rightarrow \pi^*$, $\pi \rightarrow \pi^*$). This is because the energy of these transitions has wavelengths between 200 and 700 nm. When molecules are in the ground state, two orbitals are considered: HOMO and LUMO orbitals [3,4].

A. B.

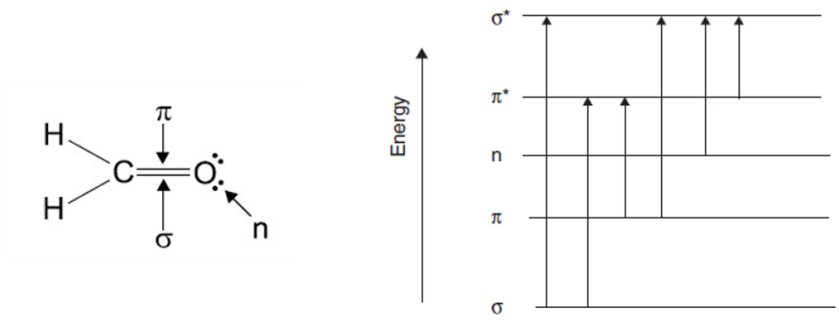

Figure 2.4. A. Formaldehyde chemical structure and existent molecular orbitals. **B.** Schematic representation of ordered molecular orbitals energies and respective electronic transitions. A and B reproduced from [3] and [4], respectively.

In ground state, the sum of electron spins is equal to zero, so the multiplicity, M, is 1 (M=2S+1), the molecule being in a singlet state. Usually, when an electron is promoted to a molecular orbital with higher energy, it maintains its spin and a singlet-singlet transition occurs. However, a spin change can happen in the excited state, causing parallel spins in the molecule. In this case, multiplicity is 3 and the molecule is in triplet state, which has lower energy than the corresponding excited singlet state. The intensity of the absorption bands in a spectrum is related with the probability of electronic transitions. If a transition is allowed, then it is more probable to occur, and a higher intensity is seen in the respective band. The higher the spatial overlay of molecular orbitals, the more likely a transition may occur, and because of that, transitions $\pi \rightarrow \pi^*$ are allowed by symmetry, while $n \rightarrow \pi^*$ are forbidden. Singlet-singlet and triplet-triplet transitions are allowed by spin, but transitions from singlet state to triplet state and vice-versa are forbidden [3,4].

2.2.1. Lambert-Beer law

Absorption spectroscopy consists in the phenomenon of absorption of light by a sample when the incident wavelength has the same energy as the transition energy of the molecule that is being excited. Then, the intensity of transmitted light (I) is lower than the intensity of the incident light (I_0). This decrease in energy is described by an exponential law [4,5]:

$$I(\lambda) = I_0 \exp\left(-\alpha_\lambda l\right) \tag{2.4}$$

where α_λ is the absorption coefficient (cm^{-1}) and l is the path length of the sample.

Spectrophotometers measure the absorbed light in terms of transmittance (T_λ), which is the ratio between I and I_0 (equation 2.5), or absorbance (A_λ), which is the negative logarithmic function of transmittance (equation 2.6) [4,5].

$$T_\lambda = \frac{I_\lambda}{I_0} \tag{2.5}$$

$$A_\lambda = -log_{10} T_\lambda \tag{2.6}$$

The amount of absorbed light is proportional to the concentration of the species present in the sample (equation 2.7) [1,5].

$$\alpha_\lambda = 2.303 \varepsilon_\lambda c \tag{2.7}$$

where ε_λ is the molar absorption coefficient and c is the concentration of the sample.

Lambert-Beer law relates the measured absorbance with concentration of the sample [1,5]:

$$\log\left(\frac{I_0}{I}\right) = A_\lambda = \varepsilon_\lambda \times c \times l \tag{2.8}$$

The molar absorption coefficient, ε_λ, measures the efficiency of the electronic transitions of molecules present in the sample and it is influenced by environment conditions. Therefore, the higher ε_λ, the more efficient will be the transition. Absorbance of molecules varies with the used solvent, so it is important to first measure the absorbance of the solvent alone, so it could be discounted from the absorbance of the sample. Then, the measured absorbance corresponds to the subtraction of the solvent absorbance (A_b), or "blank", from the absorbance of the species present in the sample (A_s) (equation 2.9) [5].

$$A\,(\lambda) = A_s - A_b = \log\left(\frac{I_0}{I}\right) - log - \left(\frac{I_0}{I_b}\right) = \log\left(\frac{I_b}{I}\right) \tag{2.9}$$

There are two types of spectrophotometers: single beam and double-beam spectrophotometers. In a single beam configuration, baseline spectrum is acquired first and only then the sample is analyzed, sequentially. Transmittance can be calculated taking the ratio of the intensity of the sample against the intensity of baseline. In a double-beam spectrophotometer the monochromatic light is divided in two paths by a rotating mirror or a beam-splitter and one beam pass through the sample cuvette and the other through the solvent cuvette (figure 2.5). Finally, the beam is focused by a second mirror onto the detector.

This configuration allows to directly obtain transmittance values and reduce sensitivity to variations in temperature, voltage or lamp intensity [1].

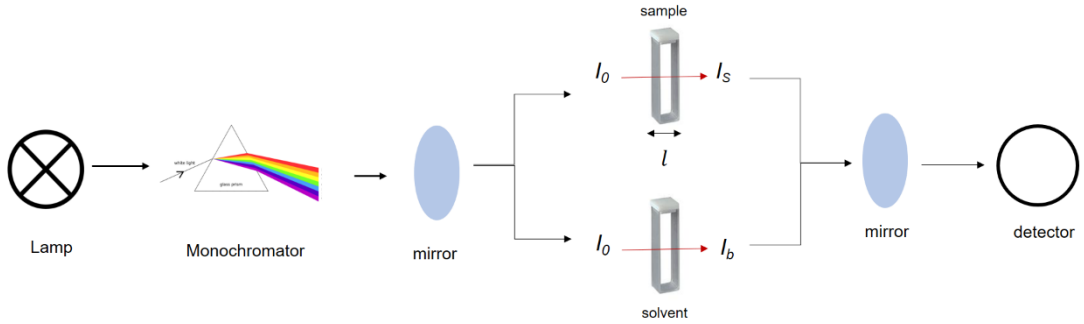

Figure 2.5. Schematic representation of a double-beam spectrophotometer.

2.3. Fluorescence spectroscopy

The absorption process leads to an electronic transition of the molecule from the ground state, S_0, to the vibrational levels of the singlet excited states S_1, S_2 or above. The instability of the excited state promotes the de-excitation of the molecule to the ground and a loss of energy. De-excitation can occur through intramolecular processes, that include radiative and non-radiative energy loss and intermolecular processes. Luminescence is a radiative process with emission of light from de-excitation of electronically excited molecules, and it is divided in fluorescence and phosphorescence. Fluorescence is the emission of light that comes mostly from $S_1 \rightarrow S_0$ relaxation and phosphorescence is also a radiative de-excitation from the triplet state T_1. In solution, the transfer of excess of energy of the excited molecule to the surrounding solvent molecules during collisions results in a loss of energy through non-radiative processes like internal conversion and vibrational relaxation, with lifetimes of 10^{-11}-10^{-9} s and 10^{-12} -10^{-10} s, respectively, which are faster than fluorescence (10^{-10} -10^{-7} s). Internal conversion is a transition between two electronic states of the same spin multiplicity and is commonly followed by vibrational relaxation to the lowest vibrational state. The efficiency of internal conversion explains why fluorescence occurs mostly from the lowest vibrational state of the electronically excited state S_1 and consequent emission at higher wavelengths than absorption. A transition from singlet state S_1 to triplet state T_1, called intersystem crossing, is also possible resulting in phosphorescence emission. This process is slow (10^{-6} - 1 s) and is predominately a forbidden transition with rate constants much lower than non-radiative de-excitation. However, intersystem crossing can occur when a molecule undergoes a spin-orbital coupling, that can result from the presence of heavy atoms, and phosphorescence is favored when the system is at low temperatures or in a rigid medium [3]. The Perrin-Jablonsky diagram (figure 2.6) is a useful way to

represent these events. The horizontal lines represent electronic and vibrational levels and the vertical arrows represent the electronic transitions between the molecule states [3,6,7].

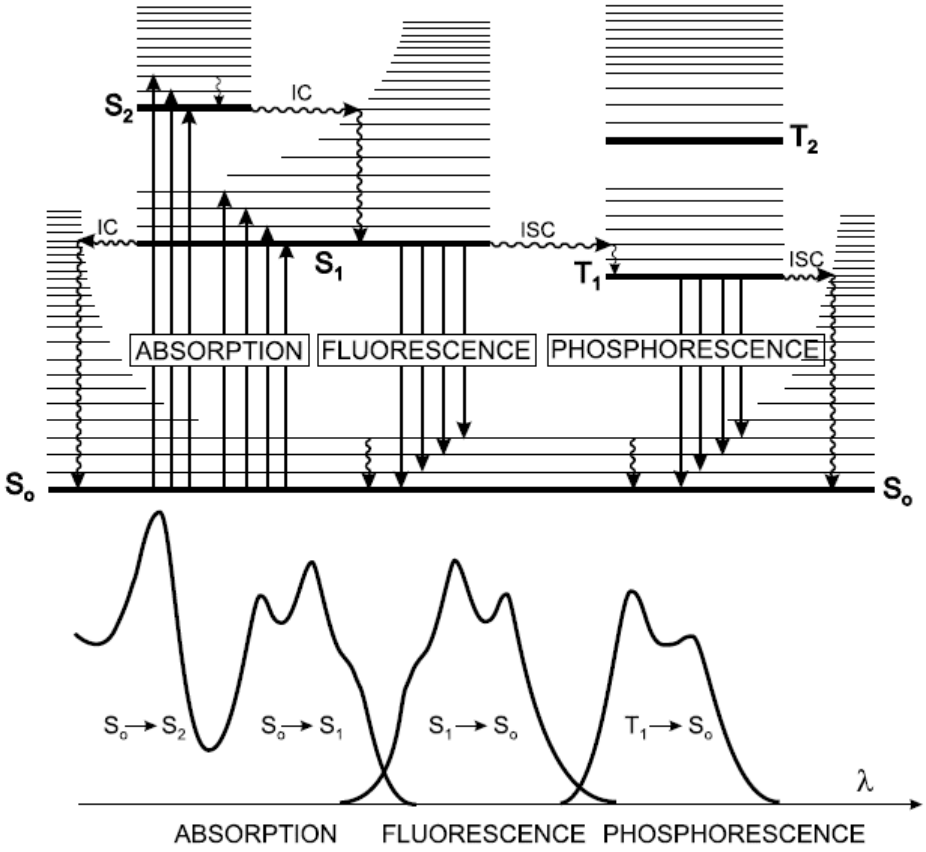

Figure 2.6. Representation of Perrin-Jablonski diagram and corresponding relative positions of absorption, fluorescence and phosphorescence spectra. IC: internal conversion, ISC: intersystem crossing. Reproduced from [3].

In general, the fluorescence emission is a mirror image of the absorption spectrum, if the energetic difference between vibrational levels of the ground and excited states is similar [3]. The gap between the maximum wavelengths of absorption and fluorescence is called Stokes' shift [3]. The 0-0 transition not always has the same energy for absorption and fluorescence. The excited state of the molecule can have a different solvation state when compared to the ground state and, after excitation, undergoes a reorientation of the solvent to an excited state in equilibrium. The emission occurs to a non-equilibrium ground state with higher energy, which results in a transition 0-0 of lower energy than the one of absorption [6,8].

2.3.1. Fluorescence lifetime and quantum yield

Excited state lifetime measures how long a molecule can be in an excited state before returning to the ground state. Deactivation processes can be described by first-order rate constants: k_r and k_{nr} for radiative (fluorescence and phosphorescence) and non-radiative processes (internal conversion and intersystem crossing), respectively. The inverse of the sum of the rate constants is the lifetime of the excited state S_1 (τ_S) or triplet state T_1 (τ_T) [3]:

$$\tau_S = \frac{1}{k_r^S + k_{nr}^S} \tag{2.10}$$

$$\tau_T = \frac{1}{k_r^T + k_{nr}^T} \tag{2.11}$$

The efficiency of the emission is measured by the fluorescence quantum yield, Φ_F, which is described by the ratio of photons that emit fluorescence to the total of photons absorbed (equation 2.12) [3]:

$$\Phi_F = \frac{k_r^S}{k_r^S + k_{nr}^S} = k_r^S \tau \tag{2.12}$$

It can be concluded that the fluorescence quantum yield is proportional to the lifetime of the excited state [3]. However, intermolecular processes of de-excitation can occur, caused by collision with other molecules. The process in which fluorescence is decreased is called quenching, and the molecules that are responsible for increasing the rate of deactivation of an electronically-excited state, are called quenchers. The presence of oxygen or heavy atoms decreases the intensity of fluorescence and, therefore, the fluorescence quantum yield. In the presence of quenchers, quantum yield is defined by [3,4,6,7]:

$$\phi_{F_q} = \frac{k_r}{k_r + k_{nr} + k_q[Q]} \tag{2.13}$$

where k_q is the quenching process rate constant and [Q] is the concentration of the quencher. The ratio between ϕ_F and ϕ_{F_q} is given by equation 2.14 [3,6],

$$\frac{\phi_F}{\phi_{F_q}} = \frac{I_0}{I} = 1 + k_q[Q]\tau_0 = 1 + K_{SV}[Q] \tag{2.14}$$

which is called the Stern-Volmer equation, where I_0 and I are the observed fluorescent intensities in the absence and in the presence of quencher and K_{SV} is the Stern-Volmer constant. K_{SV} can be determined plotting the ratio I/I_0 against the quencher concentration [3,6].

2.3.2. Förster resonance energy transfer (FRET)

Besides collisional quenching, fluorescence can be reduced by electronic energy transfer. Förster resonance energy transfer (FRET) involves a non-radiative energy transfer from an excited donor fluorophore to a ground-state acceptor fluorophore and depends on the spectral overlap between the donor emission and acceptor excitation [3,6,8]. This process occurs through dipole-dipole coupling between donor and acceptor, so the extent of energy transfer depends on the sixth power of the distance between the two molecules [3,7,8]. During FRET, it can be observed a decrease in donor emission coupled with an increase of acceptor fluorescence (figure 2.7).

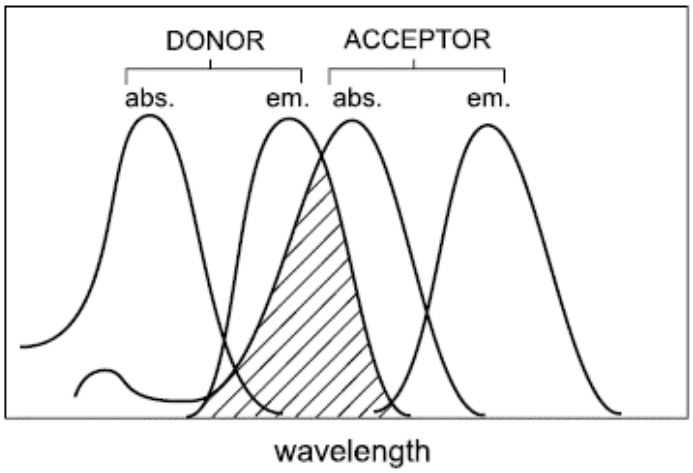

Figure 2.7. Representation of the spectral overlap between donor emission and acceptor excitation, a required condition to the occurrence of FRET. Reproduced from [3].

FRET efficiency, Φ_{FRET}, can be calculated taking the ratio of the donor integrated fluorescence intensities in the presence, F_{DA}, or absence of acceptor, F_D (equation 2.15) [9].

$$\Phi_{FRET} = 1 - \frac{F_{DA}}{F_D} \tag{2.15}$$

The Förster equation (equation 2.16) relates FRET efficiency with Förster radius, R_0, which is the distance at which the energy transfer is 50% efficient [5,6], and the distance between donor and acceptor, *r*:

$$\Phi_{FRET} = \frac{R_0^6}{R_0^6 + r^6} \tag{2.16}$$

R_0 can be obtained by the spectral overlap, J(λ), between the donor emission and acceptor absorption, according to the following equations (equations 2.17 and 2.18) [5,9]:

$$R_0 = 0.2108[k^2 \Phi_D^0 n^{-4} J(\lambda)]^{1/6} \quad (2.17)$$

$$J(\lambda) = \int_0^\infty I_D(\lambda)\varepsilon_A(\lambda)\lambda^4 d\lambda \quad (2.18)$$

where k^2 is a factor describing the orientation of the donor and acceptor dipoles, Φ_D^0 is the fluorescence quantum yield of the donor in the absence of acceptor, n is the refraction index of the medium, $I_D(\lambda)$ is the normalized fluorescence spectrum of the donor and $\varepsilon_A(\lambda)$ is the molar absorption coefficient of the acceptor.

The fluorescence quantum yield of the energy donor, Φ_D^0, in magnetoliposomes is determined by the standard method [10]:

$$\Phi_D = \frac{A_r F_s n_s^2}{A_s F_r n_r^2} \Phi_r \quad (2.19)$$

where A is the absorbance at the excitation wavelength, F the integrated emission area and n the refraction index of the solvents used. Subscripts refer to the reference (r) or sample (s).

2.3.3. Fluorescence anisotropy

Unlike natural light, the electric field of a polarized light oscillates along a given direction. Fluorophores have an absorption transition moment, M_A, with a certain angle from the electric vector $\vec{E}$ of the incident light. Molecules that have their transition moment oriented close to the electric vector of the incident polarized light are preferentially excited, a process called photoselection [3]. Fluorescence emission of fluorophores will be anisotropic because their orientation distribution is anisotropic. Anisotropy measurements can give us information on the molecular mobility in a medium, fluidity of membranes, size and shape of proteins, because during the lifetime of excited state, molecules can undergo changes in their transition moment and lead to depolarization of fluorescence, which changes anisotropy values [3,7]. In most cases, the incident light is vertically polarized, and fluorescence is observed parallel and at 90° to the propagation direction of the incident beam. A photomultiplier with a polarizer in front of it, that rotates to the desired angle, measures the fluorescence intensities of the vertically (I_{II}) and horizontally ($I_{\perp}$) polarized emission, when the sample is excited with vertically polarized light (figure 2.8) [3,11].

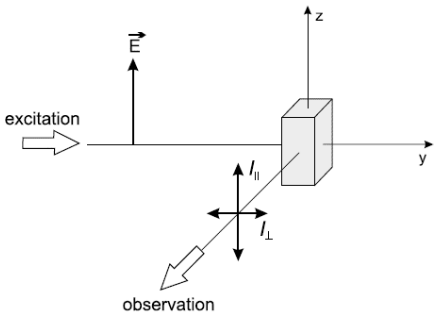

Figure 2.8. Schematic representation of the configuration for fluorescence anisotropy measurements. The sample is excited with a vertically polarized incident light and fluorescence is observed in direction O_x. $I_{\parallel}$ and $I_{\perp}$ components are measured rotating a polarizer with a parallel and perpendicular angle to the incident light, respectively. Reproduced from [3].

Fluorescence anisotropy (r) and polarization (p) represent the same phenomena but are calculated with different equations (equations 2.20 and 2.21, respectively):

$$r = \frac{I_{\parallel} - GI_{\perp}}{I_{\parallel} + 2GI_{\perp}} \tag{2.20}$$

$$p = \frac{I_{\parallel} - GI_{\perp}}{I_{\parallel} + GI_{\perp}} \tag{2.21}$$

G is a correction parameter that reflects the sensitivity of the system to differently polarized light and is calculated taking the ratio between fluorescence intensities perpendicular (I_{HV}) and parallel (I_{HH}) to the horizontally polarized incident light (equation 2.22) [11]:

$$G = \frac{I_{HV}}{I_{HH}} \tag{2.22}$$

A parameter that has strong influence in anisotropy values is the rotational diffusion during the fluorescence lifetime of the fluorophores. If lifetime is much shorter than rotation, then the fluorophore will rotate fewer times between the times of absorption and emission, leading to a higher anisotropy value [7,11]. In fluid solutions, the fluorescence lifetime of the fluorophore (τ) is much longer than rotation time, thus promoting a complete depolarization and low anisotropy values [7,11]. The relation between fluorescence anisotropy (r) and rotational correlation time of the macromolecule (θ_{rot}) is described by Perrin Equation (equation 2.23) [11]:

$$r = \frac{r_0}{1 + \frac{\tau}{\theta_{rot}}} \tag{2.23}$$

where r_0 is the anisotropy in the absence of rotational diffusion, usually $r_0 \leq 0.4$.

The rotational time of the fluorophore is proportional to the hydrodynamic volume (V) of the molecule according to Stokes-Einstein-Debye equation, which give us information on the size of the molecule (equation 2.24) [11]:

$$\theta_{rot} = \frac{\eta V}{k_B T} \tag{2.24}$$

where η is viscosity of the medium, k_B is the Boltzmann's constant and T is the temperature.

2.3.4. Spectrofluorometer instrumentation

The components needed to fluorescence measurements in spectrofluorometers are like those of the spectrophotometer (figure 2.9). These instruments can record both excitation and emission spectra [5]. Excitation spectra can be obtained fixing an emission wavelength and scanning the relative emission of the fluorophore at each excitation wavelength. This instrument uses, commonly, a xenon lamp that irradiates the sample and contains two monochromators [7]. The excitation monochromator selects the excitation wavelength and the emission monochromator, that detects fluorescence, is perpendicular to the light source [5,7]. The excitation light is divided in two beams by a beam splitter before passing through the sample, reflecting part of the excitation light to a reference cell [7]. The fluorescence emission of the sample is detected by a photomultiplier and information is displayed in graphical form. For anisotropy measurements, polarizers are placed in front of both excitation and emission monochromators.

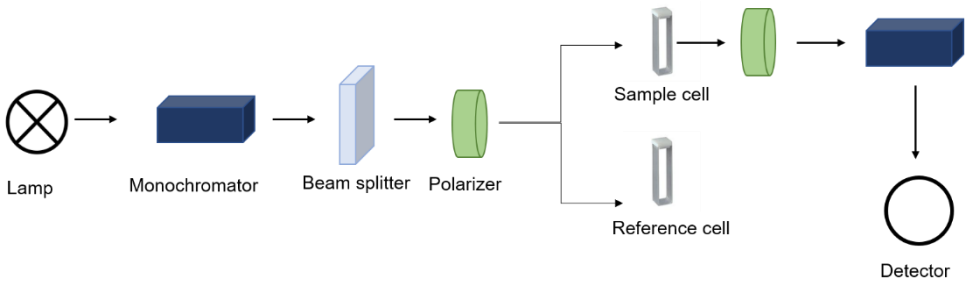

Figure 2.9. Schematic representation of the fluorescence spectroscopy instrumentation.

2.4. X-ray diffraction (XRD)

Diffraction occurs when waves of a certain radiation interact with a crystal lattice and are scattered in different directions [12]. The interference of scattered waves produces an observable pattern from which it can be deduced the arrangement of atoms in a crystal structure [12,13]. X-ray is the most used radiation because it has a wavelength of about 1 Å, which is on the same length scale as the atomic electron clouds [12]. An X-ray diffractometer consists in an X-ray source, a sample area and a detector (figure 2.10) [12]. A heated filament produces electrons that hit a metal target removing electrons from inner layers of atoms leading to de-excitation of electrons of the higher layers that emit X-ray photons [12,13]. The most common metal targets are copper anodes with a wavelength of 1.54 Å [13,14]. The periodicity of a crystal lattice is defined by atomic planes that have a certain distance between them. The diffracted rays can be constructive or destructive and give information about the orientation of the atomic planes [12,13]. The destructive interference occurs when diffracted waves cancel each other in different directions, but a constructive interference results in a single wave in a given direction from added scattered waves [12,13]. The conditions for a constructive interference to happen are described by Bragg's law (equation 2.25):

$$n\lambda = 2d\ \sin\theta \tag{2.25}$$

where n denotes the order of the reflection, λ is the wavelength of X-ray, d is the distance between atomic planes and θ is one-half the angle between the incident and scattered beams. The sample is scanned through a range of 2θ angles and the obtained peaks represent the different planes in the crystal lattice, allowing to study structural properties of different materials, crystallographic orientations and crystal dimensions by comparison of d values with standard reference patterns [13,14].

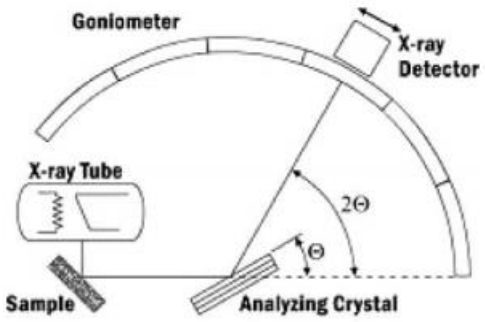

Figure 2.10. Schematic representation of an X-ray diffraction system. Reproduced from [14].

The grain size can be obtained from the parameters of the higher intensity peak by Scherrer's equation (equation 2.26):

$$L = \frac{K\,\lambda}{\Delta 2\theta \cos(\theta_B)} \tag{2.26}$$

where K is a constant associated to the shape of the crystals, λ is the wavelength of x-ray, $\Delta 2\theta$ is the full width at half maximum and θ_B the chosen Bragg peak. K=0.9 if the grains have spherical shape.

X-ray diffraction is a non-destructive technique that can be used for identification and characterization of crystalline materials, determination of predominant orientation in a crystal structure and evaluation of sample purity [14]. Besides that, it allows to obtain fast identification of an unknown mineral, requires minimal sample preparation and can be used to determine texture, size and degree of crystallinity of a sample [14].

2.5. Transmission electron microscopy (TEM)

Electron microscopy is a high-resolution technique based on wave-like behavior of electrons. Unlike light microscopy, that has a limit of resolution smaller than about 100 nm, electron microscopy allows the high voltage acceleration of electrons producing smaller wavelengths of 1 pm to 40 pm and a spatial resolution of about 0.1 nm [15]. In electron microscopy, electromagnetic lenses focus electron beams that interact with the specimen and a vacuum environment is required to avoid undesired scattering of electrons [15]. There are three types of electron microscopy, the scanning electron microscopy (SEM), transmission electron microscopy (TEM) and a hybrid version, scanning transmission electron microscopy (STEM) [15]. The main differences rely on the configuration of the microscopes. SEM microscopy is used to visualize material surfaces, whereas in TEM the electron beam passes through the sample and is collected in a parallel detector [12,15]. TEM is a technique that allows the internal analysis of ultrathin samples and imaging at the atomic level. This technique is very sensitive requiring controlled conditions like a vibration-free environment and constant temperature. The basic components of a TEM microscope comprise the electron gun, electromagnetic lenses and a detection system (figure 2.11). An 80-300 kV voltage accelerates electrons in the electron gun, producing an electron beam that is focused by the condenser lenses before interaction with the specimen. The transmitted electrons are focused by an objective lens forming a diffraction pattern that is magnified by projector lenses onto a detector that can be a CCD (charged coupled device) camera or photographic film [6,15]. There are different TEM imaging modes like bright-field imaging where the scattered electrons are blocked and the image is formed from

unscattered electrons and increased thickness or mass appear dark in the image; electron diffraction is used to obtain crystallographic information about the sample like crystal orientation and lattice parameters, through a diffraction pattern formed by elastically scattered electrons; STEM is a hybrid mode of TEM and SEM, where the focused electron beam is scanned across the specimen and the transmitted electrons are collected in a parallel detector. A high angle annular dark field (HAADF) detector that collects electrons incoherently scattered through very high angles, can be placed. When electrons hit the sample, it can occur inelastic scattering and electrons with lower energy, like X-rays, can be emitted and detected by an EDX (Energy Dispersive X-ray analysis) detector used to identify the elemental composition of materials [15].

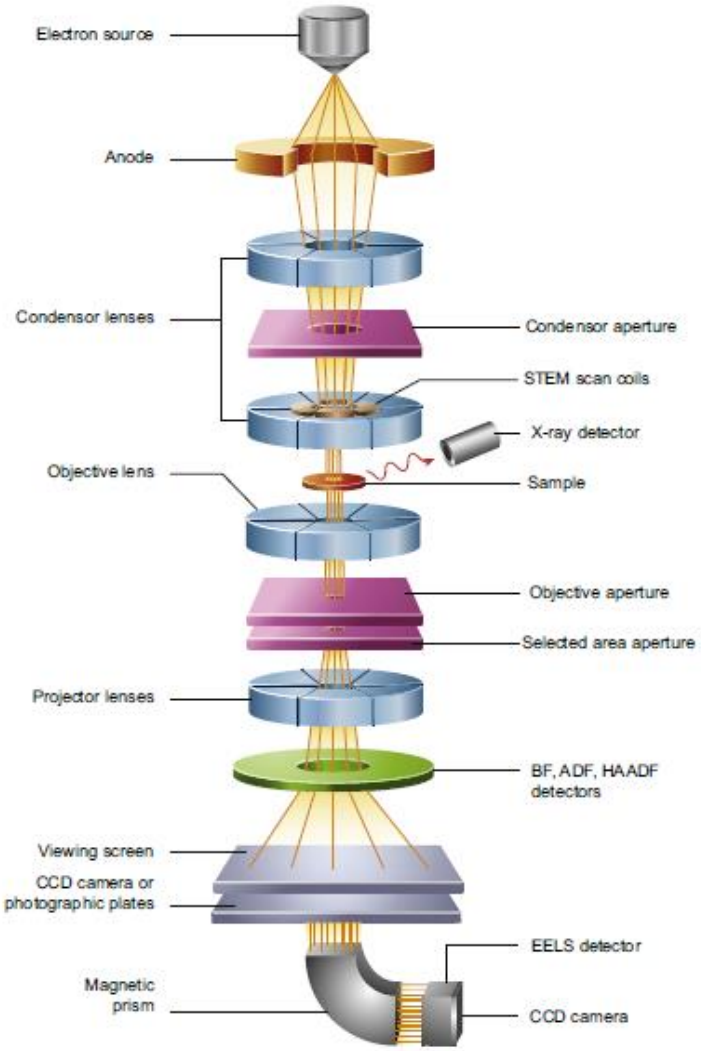

Figure 2.11. Schematic representation of a TEM microscope configuration. Reproduced from [15].

2.6. Dynamic light scattering (DLS)

Dynamic light scattering, or photo-correlation spectroscopy, is used to analyze particles or macromolecules suspended in a liquid medium based on the fluctuations of local concentration caused by the Brownian motion [6,12]. This technique is used to obtain information about the distribution of particle sizes in solutions [6,12]. A laser beam that passes through a sample is scattered in all directions as a function of the size and shape of the particles and the intensity of the scattered light is detected [12,16]. The resultant constructive and destructive interferences cause intensity fluctuations of the scattered light, giving rise to a large or small intensity, respectively [12,16,17]. In a simpler way, smaller particles will cause faster intensity fluctuations because they move more quickly than larger ones. The most common way to analyze these dynamic fluctuations is to use a time correlation function that relates the orientation or position of a particle with time and allows to obtain the diffusion coefficient of macromolecules [12,16]. The intensity fluctuations are measured through an intensity correlation function, $g_2(\tau)$, that results from a Gaussian approximation of the photon counting [16]:

$$g_2(\tau) = B + \beta|g_1(\tau)|^2 \tag{2.27}$$

where B is the baseline (~1), β is the coherence factor that depends on detector area, optical alignment, and scattering properties of particles and $g_1(\tau)$ is the electric field correlation factor which varies for monodisperse and polydisperse systems and is dependent on a decay constant, Γ:

$$\Gamma = -D_\tau q^2 \tag{2.28}$$

where $q = \frac{4\pi\eta}{\lambda}\sin(\frac{\theta}{2})$ is the Bragg wave vector. For monodisperse systems equation (2.27) can rewritten as:

$$g_2(\tau) = 1 + \beta e^{-2D_\tau q^2 \tau} \tag{2.29}$$

From equation (2.28) it is possible to obtain the translational diffusion coefficient, D_τ, and therefore the hydrodynamic radius (R_h) of a particle, through the Stokes-Einstein equation:

$$D_\tau = \frac{k_B T}{6\pi\eta R_h} \tag{2.30}$$

where k_B is the Boltzmann constant (1.38064852 × 10^{-23} J/K), T is the absolute temperature and η is the viscosity of the medium.

A conventional DLS system is mainly composed by a laser, a cell containing the suspension, a correlator and two detectors that are placed at 90° or 12.8° (forwardscattering) and 173° (backscattering) (figure 2.12.A) [17]. The instrument generates a correlogram, i.e., a raw correlation function plotted against delay time (τ), that gives information about mean size of particles and polydispersity of the sample (figure 2.12.B) [17].

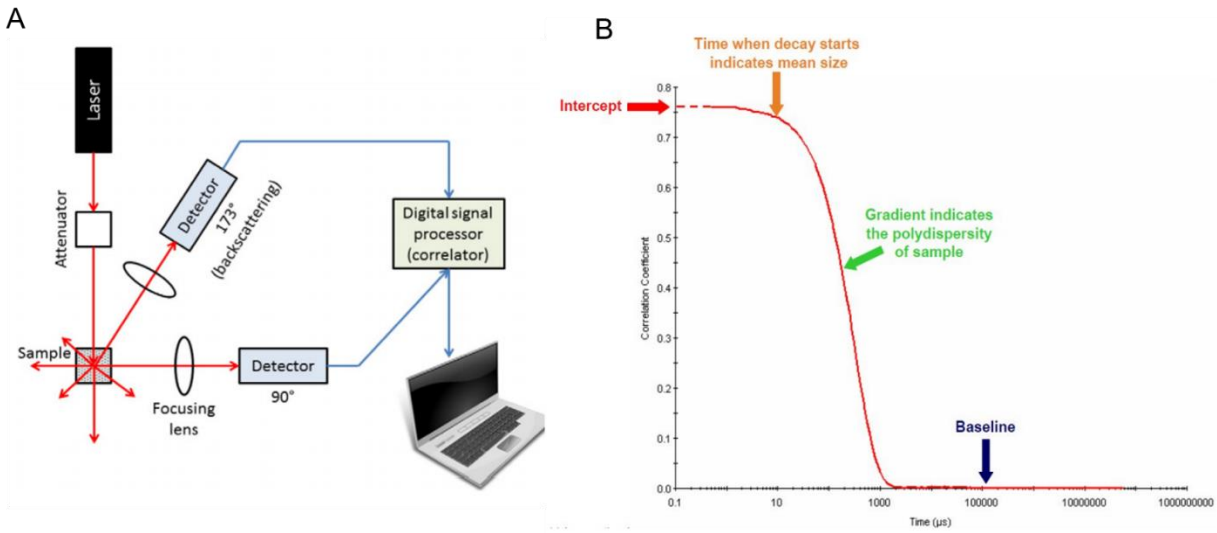

Figure 2.12. A. Instrumental set up for DLS analysis. **B.** Example of correlogram obtained by DLS analysis. A and B reproduced from [14] and [17], respectively.

Determination of parameters such as the size of particles and heterogeneity of the sample is usually achieved using two correlation function fitting models – the cumulants method and the CONTIN (*constrained regularization method for inverting data*) method [16,17]. The main difference between these two mathematical algorithms is that, in the first, a single exponential fit is applied to the correlation function, that gives an average hydrodynamic radius (Z-average size) and an estimate of the polydispersity index (PDI), instead of the CONTIN algorithm that is preferred for polydisperse systems where a multiple exponential is fitted to the correlation function to give a distribution of particle sizes [16,17,18]. Polydispersity index is a parameter obtained from the cumulants analysis of a correlation function that works like a standard deviation for a Gaussian distribution of sizes [18]. Usually, when PDI≤0.1, the sample is considered monodisperse and when PDI>0.4 the sample is polydisperse and the cumulants fit is not suitable [17].

2.7. Zeta-Potential

When a charged particle is in suspension, a double layer of ions or molecules with opposite and the same charge starts developing on the particle surface, which is called the electric double layer (EDL). The inner layer, or Stern layer, that contains ions with opposite charge to that of the particle (counter-ions), along with the diffuse layer form the EDL (figure 2.13). The diffuse layer grows beyond the Stern layer because of the electrostatic field from charged particles and comprises the slipping plane [17,19]. When an electric field is applied to the solution, the dispersant particles move to the opposite electrode, creating a potential between particles surface and the dispersing liquid, that decreases with distance from particles. The slipping plane works like an interface between Stern layer, that moves with particles, and the surrounding ions within the diffusion layer. The potential at the slipping plane is the zeta-potential (ZP) [17,19].

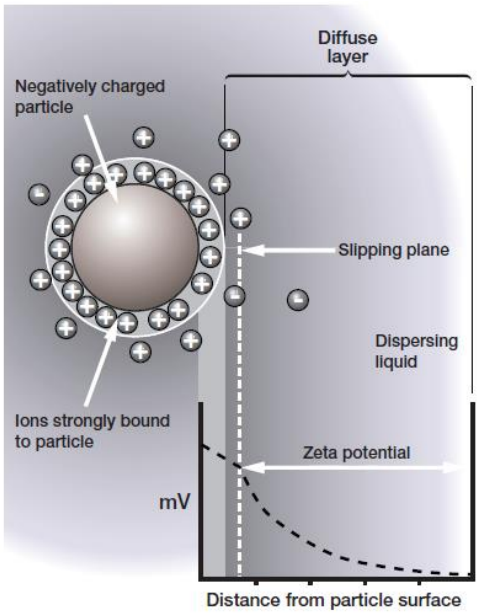

Figure 2.13. Representation of a negatively charged particle with Stern layer strongly bound to its surface and a diffuse layer composed by positive and negative ions that comprises the slipping plane. The potential at the slipping plane is the zeta potential. Reproduced from [19].

There are several factors that influence zeta potential, like the solution pH, ionic strength and concentration. It's usual to evaluate ZP variation with pH to determine isoelectric point of a solution, the pH where ZP becomes zero, and evaluate its colloidal stability. If the pH is too close to the isoelectric point, then particles will tend to agglomerate [17]. Commonly, the threshold ZP value established for colloidal systems is ±30 mV for stable nanosuspensions [20,21]. Higher values of ZP can cause instability of colloids, due to attractive van der Waals forces between particles that cannot be overcome by repulsive

forces [17,21]. Zeta potential is obtained by electrophoretic light scattering (ELS) that measures the electrophoretic mobility in an electrophoresis experiment [17]. The frequency of an incident light beam is different from the scattered light frequency of a mobile particle, causing a frequency shit or Doppler shift, that is proportional to the particle velocity. Electrophoretic mobility (μ_e) can be determined knowing particle velocity (V/μm.s^{-1}) and the electric field strength (E/volt.cm^{-1}) [17] :

$$\mu_e = \frac{V}{E} \tag{2.31}$$

Knowing the electrophoretic mobility, ZP can be calculated through Henry's equation [17]:

$$\mu_e = \frac{2\varepsilon_r \varepsilon_0 \zeta f(Ka)}{3\eta} \tag{2.32}$$

where ε_r is the dielectric constant, ε_0 is permittivity of vacuum, ζ is zeta potential, $f(Ka)$ is Henry's function and η is viscosity of the medium at experimental temperature.

2.8. Superconducting quantum interference device (SQUID)

SQUID is a highly sensitive magnetic flux detector that uses Josephson effect and the phenomena of flux quantization. The Josephson effect occurs when a loop of superconducting wire (at the superconducting state) is interrupted by a resistive barrier (Joseph junctions or "weak links") and electrons can tunnel through it to the next superconductive region without ceasing the flux [22]. Commercial SQUIDs are usually dc SQUIDs that consists of two Josephson junctions connected in parallel on a superconducting loop with an input coil (SQUID sensor) inductively coupled to it (figure 2.14.A) [22,23]. This device allows to determine several magnetic properties of the material by performing magnetic measurements [22,24]. A superconducting magnet creates a magnetic field over the sample, and changes in the magnetic flux are induced in a detection coil, so magnetization curves can be obtained [22,24]. When the temperature is fixed and the magnetization is measured with different applied magnetic fields, it can be obtained a hysteresis loop (figure 2.14.B) [24]. This type of plot allows to determine saturation magnetization (M_S), which is the maximum magnetization reached by the material when all the magnetic moments are aligned with the external field, the remanent magnetization (M_r), which is the amount of magnetization that remains at zero field, and the coercive field (H_c) that determines the field needed to apply in order to complete demagnetization of the sample [24].

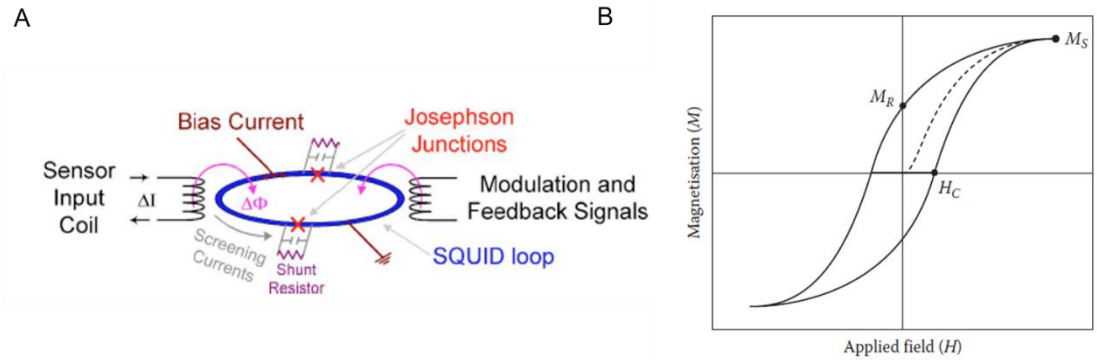

Figure 2.14. A. Schematic representation of the main components of a dc SQUID (dual junction SQUID loop). **B**. Example of a hysteresis loop and the main parameters, the saturation magnetization (M_S), the remanent magnetization (M_r) and the coercive field (H_c). A and B reproduced from [22] and [24], respectively.

In zero-field cooling (ZFC) and field-cooling (FC) experiments, the magnetization is measured with increasing temperature (figure 2.15). In a ZFC experiment, after heating up the sample to a suitable temperature, to ensure that its initial state is superparamagnetic, the sample is cooled down without magnetic field to a minimum value (T_{min}). Then, the magnetization (M_{ZFC}) is measured with increasing temperatures under the action of an external magnetic field. In a FC experiment, the sample is cooled down to T_{min} under a constant magnetic field and then, like ZFC experiment, magnetization is measured with increasing temperatures [24]. The blocking temperature (T_B) or irreversibility temperature (T_{irr}) is the temperature where the two branches of ZFC and FC experiments separate [24].

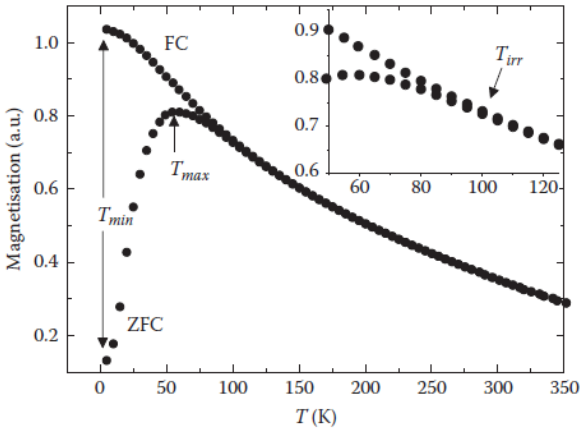

Figure 2.15. Example of ZFC and FC curves. Inset: The point from which the two branches separate is the irreversibility temperature (T_{irr}). Reproduced from [24].

2.9. Wide-field Fluorescence Microscopy

Fluorescence microscopy is one of the most used techniques for observation and analysis of structure and function of biological samples. This type of microscopy requires the use of fluorophores or fluorochromes which absorb incident light and re-emit it with higher wavelength [25,26]. The main advantages that fluorescence microscopy can offer are the high contrast and space resolution, specificity and selectivity of fluorescent labelling, and sensitivity of detection [25,26]. A whole plethora of fluorescent probes, with different excitation and emission wavelength range, is now available for the study of several structural and physiological parameters of cells like biophysical behavior of membranes [27], enzyme activity [28,29], membrane potential [30,31] and detection of subcellular compartments [32,33,34]. It is important to note that the high image contrast provided by fluorescence microscopes comes from their specialized components and mode of operation (figure 2.16.A). In general, a mercury or halogen lamp emits the excitation light, which in turn is reflected toward the sample by a dichroic mirror, that reflects the chosen exciting wavelength and allows the passage of the fluorescence emission. Excitation and emission filters are incorporated in the filter block (figure 2.16.B), in order to select the excitation wavelength and the emitted fluorescence bands, respectively, allowing the use of a wide range of fluorescent probes [25,35]. Finally, the resulting fluorescence can be observed by eye or captured with a camera resulting in an image in which the whole sample is illuminated [35].

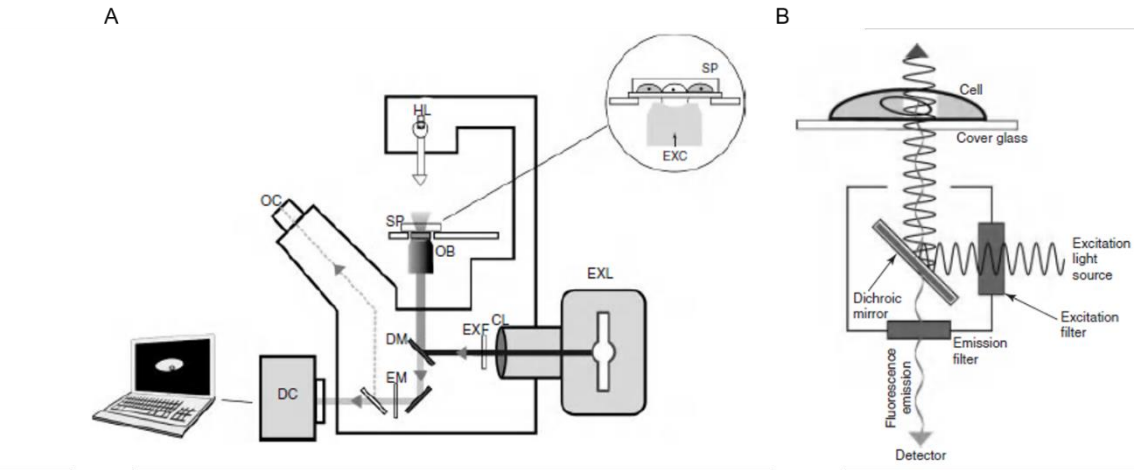

Figure 2.16. A. Schematic representation of an inverted fluorescence microscope. The specimen (SP) is illuminated by a halogen lamp (HL). The dichroic mirror (DM) reflects the exciting light from the excitation light source (EXL), that passes through the collector lens (CL) and excitation filter (EXF). The resulting image is magnified in the objective lens (OB) and fluorescence is selected in the emission filter (EM) which can be observed in the eyepiece (OC) or captured by a digital camera (DC). **B.** Schematic diagram of a filter block. A and B reproduced from [25].

2.10. References

[1] Skoog, D., Holler, F. and Crouch, S. (2018). *Principles of instrumental analysis*. 7th ed., Cengage Learning, 120-353.

[2] Owen, T. (2000). *Fundamentals of modern UV-Visible spectroscopy*. Agilent Technologies, 1-148.

[3] Valeur, B. (2002). *Molecular fluorescence: Principles and Applications*. Wiley-VCH, 1-154.

[4] Wardle, B. (2010). *Principles and Applications of Photochemistry*. John Wiley & Sons, 1-117.

[5] Shanker, N. and Bane, S. (2008). Basic Aspects of Absorption and Fluorescence Spectroscopy and Resonance Energy Transfer Methods. *Biophysical Tools for Biologists, Volume One: In Vitro Techniques*, 213-242.

[6] Campbell, I. (2012). *Biophysical techniques*. Oxford: Oxford University Press, 139-206.

[7] Lakowicz, J. (2006). *Principles of fluorescence spectroscopy*. 3rd ed. Springer, 1-381.

[8] Clapp, A., Medintz, I. and Mattoussi, H. (2006). Cover Picture: Förster Resonance Energy Transfer Investigations Using Quantum-Dot Fluorophores. *ChemPhysChem*, 7, 47-57.

[9] Rodrigues, A., Mendes, P., Silva, P., Machado, V., Almeida, B., Araújo, J., Queiroz, M., Castanheira, E. and Coutinho, P. (2017). Solid and aqueous magnetoliposomes as nanocarriers for a new potential drug active against breast cancer. *Colloids and Surfaces B: Biointerfaces*, 158, 460-468.

[10] Crosby, G. and Demas, J. (1971). Measurement of photoluminescence quantum yields. Review. *The Journal of Physical Chemistry*, 75, 991-1024.

[11] Zhang, H., Wu, Q. and Berezin, M. (2015). Fluorescence anisotropy (polarization): from drug screening to precision medicine. *Expert Opinion on Drug Discovery*, 10, 1145-1161.

[12] Zaccai, N., Serdyuk, I. and Zaccai, G. (2007). *Methods in molecular biophysics*. 1st ed. Cambridge University Press, 625-903.

[13] Tadano, S. and Giri, B. (2011). X-ray diffraction as a promising tool to characterize bone nanocomposites. *Science and Technology of Advanced Materials*, 12, 1-11.

[14] Bunaciu, A., Udriştioiu, E. and Aboul-Enein, H. (2015). X-Ray Diffraction: Instrumentation and Applications. *Critical Reviews in Analytical Chemistry*, 45, 289-299.

[15] Hübschen, G., Altpeter, I., Tschuncky, R. and Herrmann, H. (2016). *Materials characterization using nondestructive evaluation methods*. 1st ed., MA: Woodhead Publishing, an imprint of Elsevier, 17-43.

[16] Stetefeld, J., McKenna, S., Patel, T. (2016). Dynamic light scattering: a practical guide and applications in biomedical sciences. *Biophysical Reviews*, 8, 409-427.

[17] Bhattacharjee, S. (2016). DLS and zeta potential – What they are and what they are not? *Journal Of Controlled Release*, 235, 337-351.

[18] Arzenšek, D. (2010). *Dynamic light scattering and application to proteins in solutions* (Seminar). University of Ljubljana, 1-19.

[19] Malvern, I (2004). *Zetasizer Nano Series User Manual*. Malvern Instruments Ltd, 10-14.

[20] Agrawal, Y. and Patel, V. (2011). Nanosuspension: An approach to enhance solubility of drugs. *Journal of Advanced Pharmaceutical Technology & Research*, 2, 81-89.

[21] Xu, R. (2000). *Particle Characterization: Light Scattering Methods*. 1st ed. Springer, 308-318.

[22] Fagaly, R. (2006). Superconducting quantum interference device instruments and applications. *Review of Scientific Instruments*, 77, 1-46.

[23] Clarke, J. and Braginski, A. (2004). *The SQUID handbook*. 1st ed., Wiley-VCH, 1-26.

[24] Thanh, N. and Thanh, N. (2012). *Magnetic Nanoparticles*. 1st ed., Taylor and Francis, 1-18.

[25] Kubitscheck, U. (2013). *Fluorescence Microscopy*. 1st ed., Wiley-VCH, 97-111.

[26] Mondal, P. and Diaspro, A. (2014). *Fundamentals of fluorescence microscopy*. 1st ed. Springer, 102-107.

[27] Yamada, K., Toyota, T., Takakura, K., Ishimaru, M. and Sugawara, T. (2001). Preparation of BODIPY probes for multicolor fluorescence imaging studies of membrane dynamics. *New Journal of Chemistry*, 25, 667-669.

[28] Rehm, M., Düßmann, H., Jänicke, R., Tavaré, J., Kögel, D. and Prehn, J. (2002). Single-cell Fluorescence Resonance Energy Transfer Analysis Demonstrates That Caspase Activation during Apoptosis Is a Rapid Process. *Journal of Biological Chemistry*, 277, 24506-24514.

[29] Ntziachristos, V., Tung, C., Bremer, C. and Weissleder, R. (2002). Fluorescence molecular tomography resolves protease activity *in vivo*. *Nature Medicine*, 8, 757-761.

[30] Scaduto, R. and Grotyohann, L. (1999). Measurement of Mitochondrial Membrane Potential Using Fluorescent Rhodamine Derivatives. *Biophysical Journal*, 76, 469-477.

[31] Adams, D. and Levin, M. (2012). Measuring Resting Membrane Potential Using the Fluorescent Voltage Reporters $DiBAC_4$ (3) and CC2-DMPE. *Cold Spring Harbor Protocols*, 2012, 459-464.

[32] Dikalov, S. and Harrison, D. (2014). Methods for Detection of Mitochondrial and Cellular Reactive Oxygen Species. *Antioxidants & Redox Signaling*, 20, 372-382.

[33] Hunter, P., Craddock, C., Di Benedetto, S., Roberts, L. and Frigerio, L. (2007). Fluorescent Reporter Proteins for the Tonoplast and the Vacuolar Lumen Identify a Single Vacuolar Compartment in Arabidopsis Cells. *Plant Physiology*, 145, 1371-1382.

[34] Drummen, G. (2012). Fluorescent Probes and Fluorescence (Microscopy) Techniques — Illuminating Biological and Biomedical Research. *Molecules*, 17, 14067-14090.

[35] Sanderson, M., Smith, I., Parker, I. and Bootman, M. (2014). Fluorescence Microscopy. *Cold Spring Harbor Protocols*, 2014, 1-36.

Chapter 3 - Materials and methods

3.1. Nanoparticles preparation

Manganese ferrite nanoparticles were synthesized by coprecipitation method, as previously described [1], in a 5 mL aqueous solution. First, an aqueous solution containing 612 μL of NaOH 50% solution was prepared and heated to 90 ºC. Then, two aqueous solutions, each one containing 500 μL of $MnSO_4.H_2O$ 1 M and 500 μL of $FeCl_3.6H_2O$ 2 M were prepared and mixed. The mixture was added drop by drop to the previously warmed NaOH solution under magnetic stirring. The manganese ferrite nanoparticles are formed after two hours at 90 ºC. In the end of each process, nanoparticles were washed several times by magnetic decantation, dried and stored.

3.2. Magnetoliposomes preparation

3.2.1. Aqueous magnetoliposomes (AMLs)

Aqueous magnetoliposomes are formed by entrapping the synthesized magnetic nanoparticles in liposomes, using the ethanolic injection method [2]. A chloroform solution of egg yolk phosphatidylcholine (Egg-PC) 10 mM, from Avanti Polar Lipids, and a methanol solution of cholesterol 10 mM, from Sigma Aldrich, were used to lipid vesicle formation in an 8:2 ratio. The lipid mixture (2 mM) in ethanol was injected, under stirring, in a dispersion of magnetic nanoparticles $2x10^{-4}$ M in ultrapure water at room temperature (above the melting transition temperature of Egg-PC, -18 ºC [3]). Then, the ferrofluid was washed with water and purified by ultracentrifugation to remove all the non-encapsulated nanoparticles. AMLs with lactoferrin (bLf) were prepared by ethanolic injection method as well, this method being considered suitable for protein entrapment [4]. Lactoferrin 21% iron-saturated, from DMV (Veghel, The Netherlands), in water solution with a concentration of 100 μM (5%) was added to the aqueous solution containing magnetic nanoparticles, promoting the entrapment of lactoferrin in the aqueous core of the AMLs [5].

3.2.2. Solid magnetoliposomes (SMLs)

Solid magnetoliposomes (SMLs) were prepared by a method previously developed [6]. An Egg-PC and cholesterol 10 mM mixture (8:2) in methanol was used to produce the lipid bilayer around magnetic nanoparticles with a final concentration of 2 mM. 40 μL of nanoparticles solution $2x10^{-4}$ M were dispersed in an ultrasonicator for 1 min at 195 W. Then, 6 mL of chloroform were added, resulting in a solution

with a floating water bubble that contains the nanoparticles cluster (figure 3.1). After vigorous agitation, 600 μL of the lipid solution were added to form the first lipid layer, under vortexing. The particles were washed twice by magnetic decantation with pure water, in order to remove the lipid that was not attached to the nanoparticles. The second layer was formed by injection of the remaining 600 μL of lipid solution, under vortexing. The resulting SMLs were then washed and purified with pure water by centrifugation.

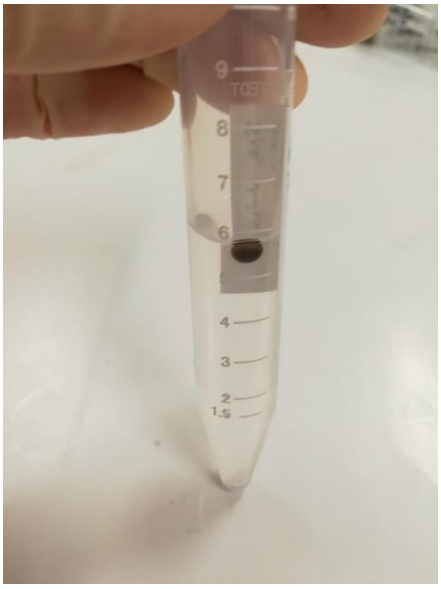

Figure 3.1. Preparation of solid magnetoliposomes. The water bubble contains the manganese ferrite nanoparticles cluster.

3.2.3. SMLs with lactoferrin

First, 10 mL of a chloroform solution containing DSPE-PEG_{2000} and CDI at a molar ratio 1:10 was prepared. The reaction was performed at 60 ºC for 2 hours and under stirring. SMLs were prepared by the method described above except for the second lipid layer, which was formed by injection of a CDI activated PEG with Egg-PC/cholesterol solution (1:1 molar ratio) under vortexing at 0°C [7]. Then, the SMLs were washed and bLf was added with a concentration of 100 μM at 0 ºC [7]. The mixture was kept at 4°C overnight. Then, the resulting SMLs were washed, purified by magnetic separation and resuspended in 3 mL of water. The conjugation reaction of lactoferrin to SMLs is represented in figure 3.2. First, CDI reacts with hydroxyl groups of PEG to form an active intermediate with a leaving imidazole group. In the presence of a primary amine containing molecule, the nucleophile attacks the carbonyl group of the intermediate, promoting the exit of imidazole and the formation of a carbamate linkage.

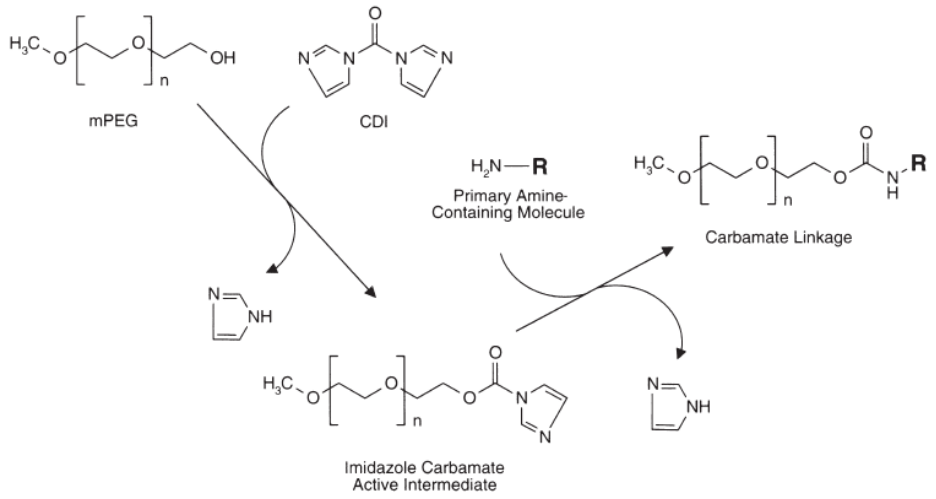

Figure 3.2. Schematic representation of the chemical pathways involved in the conjugation reaction between SMLs and lactoferrin promoted by CDI. Reproduced from [8].

3.3. Giant Unilamellar Vesicles (GUVs) preparation

The lipid egg-PC was used for GUVs preparation, using a previously described method [9,10]. 250 μL of an Egg-PC chloroform solution 20 mM were dried under an ultrapure nitrogen stream to form a thin film. Then, 40 μL of water were added to the lipid film and the dispersion was incubated at 45 ºC for 15 min. After that, it was added 5 mL of a glucose aqueous solution 0.1 M and the mixture was incubated again at 37 ºC for 2 hours. Finally, the GUVs suspension was centrifugated at 20 ºC, 12000 rpm, for 30 min.

3.4. Structural characterization

3.4.1. X-ray diffraction (XRD)

The crystalline structure of $MnFe_2O_4$ nanoparticles was characterized by the X-ray diffraction (XRD) technique, using a PAN'alytical X'Pert PRO diffractometer (at UME-UTAD), at room temperature with Cu K_α radiation (λ=1.5418 Å), in a Bragg-Brentano configuration. X-ray diffraction (XRD) patterns were analyzed with FullProf program by employing Rietveld refinement technique and using the Fd-3m:2 space group [11]. The crystallographic structure of Si was adopted as a structural model in the Rietveld refinement. The background was described using a 6-coefficent polynomial function and the diffraction profile was modeled by a pseudo-Voigt peak shape function (Thompson-Cox-Hastings pseudo-Voigt). The expression used in Rietveld method to correct the full width at half maximum (FWHM) is defined as:

$$FWHM^2 = U\,tan^2\theta + V\,tan\theta + W \quad (3.1)$$

where U, V and W are peak shape parameters.

3.4.2. Transmission electron microscopy

HR-TEM (High Resolution Transmission Electron Microscopy) images of manganese ferrite and solid magnetoliposomes were recorded using a Transmission Electron Microscope JEOL JEM 2010F operating at 200 kV coupled to an Electron Dispersive Spectroscopic analyzer (EDS) at C.A.C.T.I (Centro de Apoio Científico e Tecnolóxico á Investigación), Vigo, Spain. For the solid magnetoliposomes, a negative staining was employed, using a 2% aqueous solution of ammonium molybdate tetrahydrate. 20 μL of sample and 20 μL of staining solution were mixed and a drop of the mixture was placed onto a Formvar grid, held by tweezers. After 20 s, almost all the solution was removed with filter paper and left dry.

3.4.3. Superconducting Quantum Interference Device (SQUID) measurements

Magnetic measurements were performed in a Superconducting Quantum Interference Device (SQUID) magnetometer (Quantum Design MPMS5XL), at room temperature, applying magnetic fields up to 5.5 T. The magnetization hysteresis loop measurements were carried out by fixing the temperature and measuring the magnetization at a series of different applied magnetic fields.

3.4.4. Dynamic light scattering (DLS) and ELS (electrophoretic light scattering) measurements

Egg-PC/cholesterol (8:2) magnetoliposomes without and with bLf (5%) were prepared by the method described in section 3.2, in order to perform DLS and ELS measurements and obtain their mean size, PDI (polydispersity index) and zeta-potential. For DLS experiments, aliquots of 1.5 mL of the prepared samples were filtered (0.45 μm) and placed in a disposable polystyrene cell and measured at 25 ºC using a Zetasizer Nano ZS (Malvern Instruments) with a He-Ne laser of λ= 632.8 nm and a detector angle of 173º (backscattering). Zeta-potential was also obtained using Zetasizer Nano ZS, and for this experiment, samples were placed in a 0.75 mL folded capillary cell. All samples were suspended in ultrapure water, with a refractive index n= 1.33. Three independent measurements were performed for each sample.

3.5. Spectroscopic measurements

UV-Visible absorption measurements were carried out in a Shimadzu UV-3600 Plus UV-Vis-NIR spectrophotometer and fluorescence spectra were recorded in Fluorolog 3 spectrofluorimeter, equipped with double monochromators in both excitation and emission and a temperature-controlled cuvette holder.

3.5.1. Fluorescence quantum yield

Fluorescence quantum yield of bLf (acting as the energy donor in FRET experiments) in water was determined by the standard method [12,13], in which the unknown fluorescence efficiency of a molecule is related to that of a standard or reference. The absorption and emission bands of lactoferrin overlap those of tryptophan, as this fluorescent molecule is present in proteins, so it was chosen as reference molecule. Absorption and fluorescence spectra of solutions of both tryptophan and bLf were obtained and used in equation 3.2,

$$\Phi_{F_s} = \frac{A_r F_s n_s^2}{A_s F_r n_r^2} \Phi_{F_r} \tag{3.2}$$

where Φ_F is fluorescence quantum yield, A is the absorbance at the excitation wavelength (270 nm), F is the integrated emission area and n the refraction index of the solvents used (in this case, ultrapure water in both sample and reference solutions). Subscripts s and r refer to the standard and reference, respectively. Absorbance at the excitation wavelength was measured below 0.1 to avoid inner filter effects [12].

3.5.2. Förster Resonance Energy Transfer (FRET) measurements

The formation of the lipid bilayer around manganese ferrite nanoparticles in SMLs was investigated by Förster Resonance Energy Transfer (FRET). For that purpose, the lipophilic probe 1,6-diphenyl-1,3,5-hexatriene (DPH) was included in the first lipid layer, while bLf was included in the second lipid layer. FRET efficiency can be defined as the proportion of donor molecules that transfer their excess energy to acceptor molecules and it was calculated by taking the ratio of donor integrated fluorescence intensities in the presence (F_{DA}) and in the absence (F_D) of acceptor (equation 3.3) [14].

$$\Phi_{FRET} = 1 - \frac{F_{DA}}{F_D} \tag{3.3}$$

The distance between donor and acceptor molecules was determined through the FRET efficiency (equation 3.4),

$$r_{AD} = R_0 \left[\frac{1-\Phi_{FRET}}{\Phi_{FRET}}\right]^{1/6} \quad (3.4)$$

where R_0 is the Förster radius (equation 3.5) and is obtained by the spectral overlap, J(λ) (equation 3.6), between the donor emission and the acceptor absorption (with R_0 in Å, λ in nm, ε_A (λ) in M^{-1} cm^{-1}) [14],

$$R_0 = 0.2108[k_D^2 \Phi_D^0 n^{-4} J(\lambda)]^{1/6} \quad (3.5)$$

$$J(\lambda) = \int_0^\infty I_D(\lambda)\varepsilon_A(\lambda)\lambda^4 \, d\lambda \quad (3.6)$$

where k^2= 2/3 is the orientational factor assuming random orientation of the fluorophores, Φ_D^0 is the fluorescence quantum yield of the donor in the absence of energy transfer, n is the refraction index of the medium, $I_D(\lambda)$ is the fluorescence spectrum of the donor normalized so that $\int_0^\infty I_D(\lambda)\, d\lambda$=1, and $\varepsilon_A(\lambda)$ is the molar absorption coefficient of the acceptor.

3.6. Lactoferrin encapsulation efficiency

The encapsulation efficiency, EE (%), of bLf in magnetoliposomes was determined through absorption measurements. For this purpose, a calibration curve was made using several concentrations of bLf in ultrapure water. First, a 250 μM bLf solution was prepared and successive dilutions were made to obtain 12 other standard solutions with concentrations of 62.5 μM to 1.35 μM. Absorbance of all samples was measured in the wavelength range 200-600 nm and ultrapure water was used as blank. A calibration curve was constructed by plotting maximum absorbance *versus* bLf concentration. A linear regression was fitted to the data, allowing to determine bLf concentration in a sample if its absorbance is known. AMLs and SMLs were prepared as described in section 3.2, in which 100 μM of bLf were added. After that, magnetic separation was performed to obtain the supernatants containing protein that was not encapsulated, and their absorbances were measured. The EE (%) was determined using equation 3.7. Three independent measurements were performed for each type of magnetoliposomes and standard deviations (SD) were calculated.

$$EE\ (\%) = \frac{[bLf]_t - [bLf]_{non-encapsulated}}{[bLf]_t} \quad (3.7)$$

where $[bLf]_t$ is the total concentration of lactoferrin that was added in magnetoliposomes preparation and $[bLf]_{non\text{-}encapsulated}$ is the concentration of lactoferrin present in the supernatant or non-encapsulated.

3.7. Assays with non-tumorigenic and cancer breast cells

3.7.1. Cell lines and culture conditions

Hs 578T cells were grown in Dulbecco's modified Eagle's medium (DMEM) containing 10% fetal bovine serum (FBS) and 1% zellshield, while MCF-10-2A cells were grown in DMEM-F12 supplemented with 5% horse serum, 1% zellshield, 20 ng/ml epidermal growth factor (EGF), 100 ng/ml cholera toxin, 0.01 mg/ml insulin and 500 ng/ml hydrocortisone. The cell lines were maintained at 37 °C in a humidified atmosphere with 5% CO_2. For experiments with cells, AMLs and SMLs were prepared by the same method as described in section 3.2, but a concentration of 5 mM of lipid, $5x10^{-3}$ M of nanoparticles and 250 μM of lactoferrin (5%) were added. The final concentration of these magnetoliposomes solutions will be considered as 5x and all volumes of sample used in these experiments were taken from those solutions.

3.7.2. Assessment of cells proliferation by Sulforhodamine B (SRB) assay

Firstly, the effect of unloaded AMLs was studied. For this experiment, cells were seeded in a 6 well-plate (V_f of each well= 1500 μL) at a concentration of $1x10^5$ cells/mL. The unloaded AMLs solution (5×) was resuspended in DMEM and added to cells with increasing volumes of 30 μL (0.1×), 75 μL (0.25×), 150 μL (0.5×), 300 μL (1×) and 600 μL (2×), and then incubated at 37 °C for 48 h. The second experiment consisted in the study of the effect of unloaded and bLf-loaded (250 μM) AMLs and SMLs in MCF-10-2A and Hs 578T cells. For these experiments, cells were seeded in a 24 well-plate (V_f of each well= 500 μL) at a concentration of $8.5x10^4$ cells/mL for Hs 578T cells and $2x10^5$ cells/mL for MCF-10-2A cells. 200 μL (2×) and 400 μL (4×) of AMLs and SMLs were added to cells and incubated at 37 °C for 48 h. After this incubation period, cells were washed with 1x PBS, fixed with ice-cold 1% acetic acid in methanol (1.5 mL) and kept at -20 °C for 90 min. After removing the fixation solution, the plates were draw and cells were then incubated with 0.5% (w/v) SRB in 1% acetic acid for 90 min at 37°C. Next, cells were washed with 1% acetic acid and SRB was dissolved in 10 mM Tris for 10 minutes at room temperature. Two samples of 200 μL for each condition were transferred to a 96-well plate and absorbance was read at 540 nm in a microplate reader (SpectraMax Plus, Molecular Devices). Results were normalized to the control which was considered to have 100% cell proliferation.

3.7.3. Study of the internalization of magnetoliposomes in cells by fluorescence microscopy

Cells were incubated with unloaded and bLf-loaded AMLs and SMLs as described in section 3.7.2 and visualized in a DM-5000B upright fluorescence microscope (Leica Microsystems), after 48h. For that purpose, the lipid bilayers of magnetoliposomes were labeled with the hydrophobic dye Nile Red (from Fluka).

3.8. Experiments with yeast cells

3.8.1. Culture conditions

S. cerevisiae cells were grown in YPD medium (1% yeast extract, 2% peptone, 2% glucose) to a final optical density at 640 nm ($OD_{640\ nm}$) of 0.7. After reaching this OD, cells were centrifugated at 5000 rpm for 3 min and resuspended in 10 mM Tris-HCl pH 7.4 buffer to a final OD_{640nm} of 0.5. After treatment with different conditions and incubation for different timepoints, cells were prepared for spots assay. For the first experiment, AMLs and SMLs were prepared with 1mM of lipid, $1x10^{-4}$ M of nanoparticles and 20 μM of lactoferrin (2%) (stock solution of 1×). For the second experiment, AMLs and SMLs were prepared with 5 mM of lipid, $5x10^{-3}$ M of nanoparticles and 250 μM of bLf (5%). The final concentration of the latter magnetoliposomes solutions will be considered as 5×.

3.8.2. Yeast spots assay

Two different experiments were performed. First, 13 conditions were tested with different dilutions of control (only cells), AMLs, AMLs with bLf 20 μM (2%), SMLs and SMLs with bLf 20 μM (2%) solutions (table 3.1) with incubation times of 0, 90 and 240 minutes. A control consisting of a bLf aqueous solution was used with a concentration of 5 μM. In the second experiment four conditions were tested: unloaded AMLs and SMLs and bLf-loaded AMLs and SMLs (AMLs+bLf and SMLs+bLf). Yeast cells were grown and when exponential growth phase was reached, magnetoliposomes were added in a 1:1 cell suspension/magnetoliposomes suspension ratio. For spots assay, at each incubation time point, aliquots of 100 μL were taken to OD measurement and to an eppendorf filled with 900 μL of water to obtain the first dilution (10^{-1}). Consecutive dilutions were performed from the initial solution, resulting in other three dilutions (10^{-2}, 10^{-3}, 10^{-4}). 5 μL of each eppendorf were dropped to petri dishes with YPD medium and agar (figure 3.3). Petri dishes were incubated at 30 ºC for about 24 hours and placed in the ChemiDoc-It®^{TS2} imaging system to obtain images of the grown cultures.

Table 3.1. Different conditions used to test unloaded and bLf-loaded AMLs and SMLs in yeast cells. c-: control without lactoferrin.

Dilutions	c-	AML/SML	AML/SML+bLf
1:2	2500 µL ultrapure H_2O + 2500 µL cells	2500 µL AML/SML + 2500 µL cells	2500 µL AML/SML+bLf + 2500 µL cells
1:5	1000 µL ultrapure H_2O + 4000 µL cells	1000 µL AML/SML + 4000 µL cells	1000 µL AML/SML+bLf + 4000 cells
1:10	500 µL ultrapure H_2O + 4500 µL cells	500 µL AML/SML + 4500 µL cells	500 µL AML/SML+bLf + 4500 µL cells
1:20	250 µL ultrapure H_2O + 4750 µL cells	250 µL AML/SML + 4750 µL cells	250 µL AML/SML+bLf + 4750 µL cells

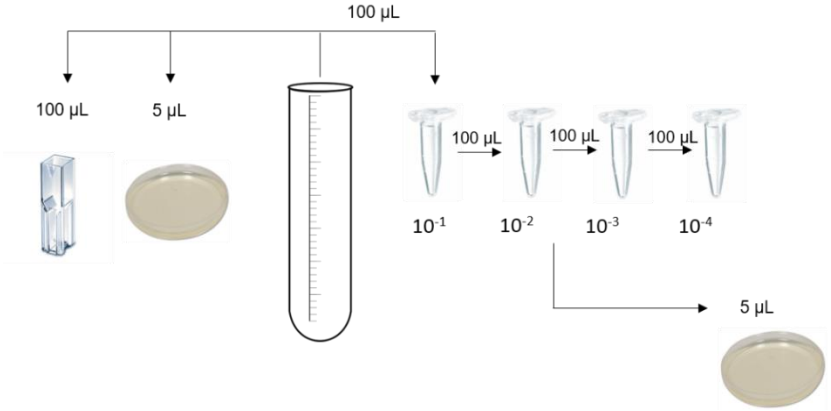

Figure 3.3. Schematic representation of the method used to test yeast cell capability to grow under certain conditions.

3.8.3. Thermal treatment of lactoferrin

In order to assess if bLf can be manipulated at high temperatures and maintain its antifungal activity, yeast cells were incubated at 30 ºC with agitation (200 rpm) with bLf 5 µM at room temperature and bLf 5 µM previously heated at 60 ºC and 90 ºC, for 90 min. A control was made with cells without bLf. Spots assay was then performed as described in section 3.8.2.

3.9. References

[1] Rodrigues, A., Ramos, J., Gomes, I., Almeida, B., Araújo, J., Queiroz, M., Coutinho, P. and Castanheira, E. (2016). Magnetoliposomes based on manganese ferrite nanoparticles as nanocarriers for antitumor drugs. RSC Advances, 6, 17302-17313.

[2] Kremer, J., Van der Esker, M., Pathmamanoharan, C. and Wiersema, P. (1977). Vesicles of variable diameter prepared by a modified injection method. *Biochemistry*, 16, 3932-3935.

[3] Li, J., Wang, X., Zhang, T., Wang, C., Huang, Z., Luo, X. and Deng, Y. (2015). A review on phospholipids and their main applications in drug delivery systems. *Asian Journal of Pharmaceutical Sciences*, 10, 81-98.

[4] Wang, C. and Huang, Y. (2003). Encapsulating Protein into Preformed Liposomes by Ethanol Destabilized Method. *Artificial Cells, Blood Substitutes, and Biotechnology*, 31, 303-312.

[5] Ishikado, A., Imanaka, H., Takeuchi, T., Harada, E. and Makino, T. (2005). Liposomalization of Lactoferrin Enhanced its Anti-inflammatory Effects via Oral Administration. *Biological & Pharmaceutical Bulletin*, 28, 1717-1721.

[6] Rodrigues, A., Gomes, I., Almeida, B., Araújo, J., Castanheira, E. and Coutinho, P. (2015). Magnetic liposomes based on nickel ferrite nanoparticles for biomedical applications. *Physical Chemistry Chemical Physics*, 17, 18011-18021.

[7] Padiya, K., Gavade, S., Kardile, B., Tiwari, M., Bajare, S., Mane, M., Gaware, V., Varghese, S., Harel, D. and Kurhade, S. (2012). Unprecedented "In Water" Imidazole Carbonylation: Paradigm Shift for Preparation of Urea and Carbamate. *Organic Letters*, 14, 2814-2817.

[8] Hermanson, G. (2013). *Bioconjugate techniques*. 3rd ed. Acad. Press, Amsterdam, 827-828.

[9] Tamba, Y., Terashima, H., Yamazaki, M. (2011). A membrane filtering method for the purification of giant unilamellar vesicles, *Chemistry and Physics of Lipids*, 164, 351-358.

[10] Tanaka, T., Tamba, Y., Masum, S. M., Yamashita, Y., Yamazaki, M. (2002). La^{3+} and Gd^{3+} induce shape change of giant unilamellar vesicles of phosphatidylcholine, *Biochimica et Biophysica Acta*, 1564, 173-182.

[11] Kumar, L., Kumar, P., Narayan, A. and Kar, M. (2013). Rietveld analysis of XRD patterns of different sizes of nanocrystalline cobalt ferrite. *International Nano Letters*, 3, 1-12.

[12] Fery-Forgues, S., Lavabre, D. (1999). Are Fluorescence Quantum Yields So Tricky to Measure? A Demonstration Using Familiar Stationery Products. *Journal of Chemical Education*, 76, 1260-1265.

[13] Rurack, K. (2008). Fluorescence Quantum Yields: Methods of Determination and Standards. *Standardization and Quality Assurance in Fluorescence Measurements I*, 5, 101-145.

[14] Valeur, B. (2002). *Molecular fluorescence: Principles and Applications*. Wiley-VCH, Weinheim, 1-154.

4.1. Manganese ferrite nanoparticles characterization

Structural and magnetic properties of ferrite nanoparticles are largely influenced by the preparation method [1]. Here, manganese ferrite nanoparticles were prepared by co-precipitation method, in which $MnSO_4.H_2O$ and $FeCl_3.6H_2O$ were used as salt precursors and the temperature of reaction was 90 ºC.

4.1.1. UV/Visible absorption

The UV/Visible absorption spectrum of manganese ferrite nanoparticles is shown in figure 4.1. A broad absorption band characteristic of this type of nanoparticles [2], evidencing a strong absorption in the UV/visible range, is observed. The band gap energy (E_g) can be obtained using the Tauc plot, that is described by the following equation (equation 4.1) [2]:

$$(\alpha h\nu)^n \propto (h\nu - E_g) \tag{4.1}$$

where α is the absorption coefficient, h is the Planck's constant, ν is the light frequency and n refers to the nature of the transition, being equal to 2 for a direct semicondutcor and ½ for an indirect one. A linear relation was obtained for n= ½ as already reported by Rodrigues *et al.* [2], indicating the indirect semiconductor nature. The linear fitted curve of $(\alpha h\nu)^n$ was extrapolated to energy axis at α=0 [3] and the value of band gap energy obtained for manganese ferrite nanoparticles was 1.08 eV, in accordance with a previous reported value of 0.98 eV [2,3] (figure 4.1).

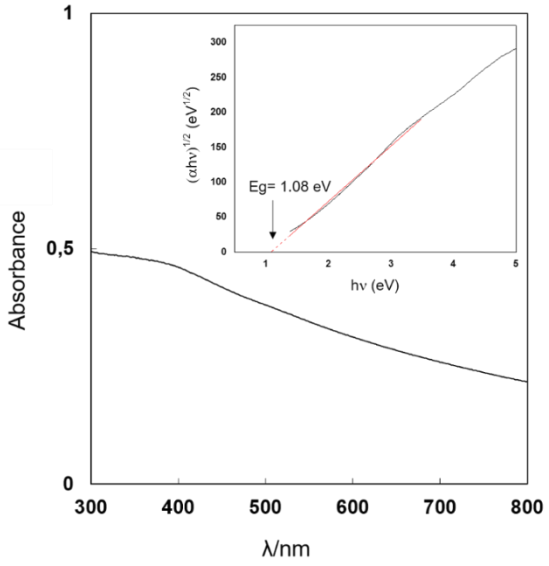

Figure 4.1. Absorption spectrum of manganese ferrite nanoparticles. Inset: Tauc plot of manganese ferrite nanoparticles.

4.1.2. X-ray diffraction (XRD) analysis

XRD diffraction pattern confirms the synthesis of manganese ferrite nanoparticles and shows well-defined peaks, evidencing a crystalline structure, even without calcination as previously reported [2]. Characteristic diffraction peaks and respective reflection planes of manganese ferrite nanoparticles are observed at 2θ=29.9° (2 2 0), 35.1° (3 1 1), 36.7° (2 2 2), 42.6° (4 0 0), 52.9° (4 2 2), 56.4° (5 1 1) and (3 3 3), and 62.0° (4 4 0), indicating the formation of a spinel structure (figure 4.2) [4,5]. Rietveld analysis was performed, allowing to estimate a particle size of 14.5 ± 0.8 nm, suggesting that nanoparticles are single domain. Although R_f factor was higher than the ones reported before [2], a low value for the fitting quality parameter (χ^2=1.40) was achieved, meaning that a good refinement was performed.

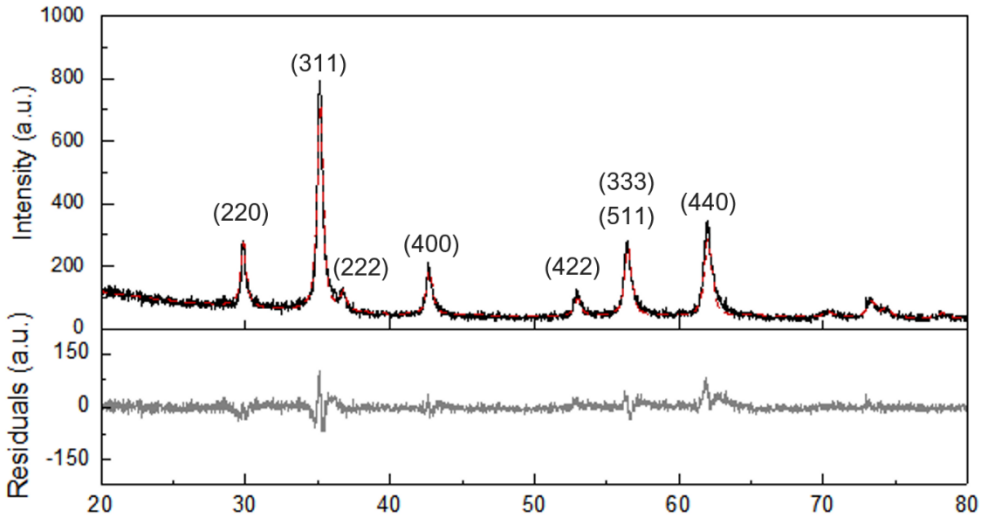

Figure 4.2. X-ray diffraction pattern of manganese ferrite nanoparticles.

4.1.3. Transmission Electron Microscopy (TEM)

Transmission electron microscopy images enable the analysis of size, shape and agglomeration degree of nanoparticles. A TEM image of the prepared manganese ferrite nanoparticles is shown in figure 4.3. As it can be observed, the sample contains almost spherical agglomerates of nanoparticles. The average size was determined using ImageJ software, and the values found were in the range of 9 – 21 nm. A mean value of 14.5 ± 6 nm was calculated, which is in good agreement with the size obtained from XRD results and thus confirming that these nanoparticles are magnetic single domain and exhibit superparamagnetic behavior.

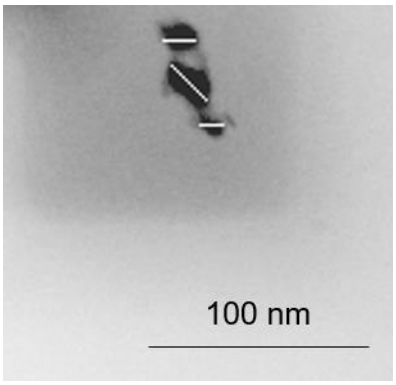

Figure 4.3. Transmission electron image of manganese ferrite nanoparticles prepared by co-precipitation method.

4.1.4. Magnetic properties

A magnetization hysteresis loop of manganese ferrite nanoparticles, which relates the induced magnetic moment (M) with the applied magnetic field (H), was obtained using a SQUID magnetometer at room temperature (figure 4.4). Values of saturation magnetization (M_s), remanent magnetization (M_r) and coercive field (H_c) are summarized in table 4.1. A high value of M_s was obtained (M_S= 55 emu g^{-1}), despite being slightly lower than the ones reported before for manganese ferrite nanoparticles (58 – 74 emu g^{-1}) [6-9]. This decrease in magnetization and high coercivity (H_c=38.83 Oe) could be due to magnetocrystalline anisotropy and surface spin disorders that interfere with the alignment of spins in superparamagnetic nanoparticles [8-10].

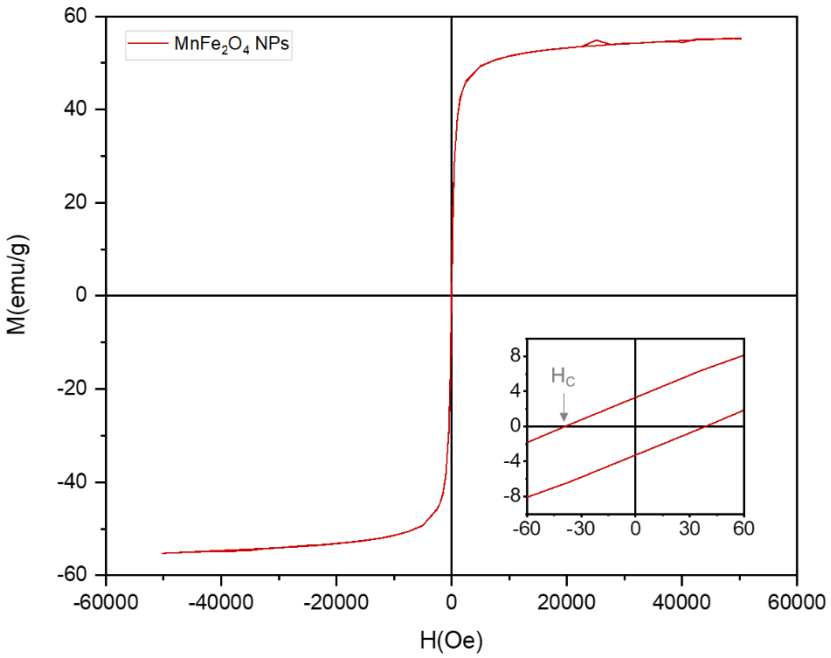

Figure 4.4. Magnetization hysteresis loop of manganese ferrite nanoparticles. Inset: Enlargement of the loop in the low field region. H_C: coercive field.

The presence of superparamagnetic behavior was inferred by taking the ratio between M_r and M_s, which is the magnetic squareness value of the hysteresis cycle. A magnetic squareness value below 0.1 means that 90% of magnetization is lost when the applied magnetic field is removed and that the material is superparamagnetic [11,12]. The magnetic squareness value obtained for the prepared manganese ferrite nanoparticles is 0.06, indicating that these nanoparticles present superparamagnetic behavior at room temperature. This feature is considered of major importance for biomedical applications, such as the use for nanodelivery systems, because when applying an external magnetic field, magnetic nanoparticles can be guided to a specific target and remain in that location after the removal of the magnetic field, allowing to reduce non-specific toxicity [13-15].

Table 4.1. Coercivity (H_C), magnetization saturation (M_S), remanent magnetization (M_r) and magnetic squareness value (M_r/M_S) for manganese ferrite nanoparticles.

H_c (Oe)	M_S (emu g^{-1})	M_r (emu g^{-1})	M_r/M_S
38.83	55.21	3.36	0.06

4.2. Characterization of bovine lactoferrin (bLf)-loaded magnetoliposomes

4.2.1. Incorporation of bLf in magnetoliposomes

Both aqueous and solid magnetoliposomes containing bLf were prepared. The lipid bilayer was composed by a mixture of Egg-PC and cholesterol in an 8:2 molar ratio. Cholesterol was used in this formulation because it is known to improve liposomal stability and modulate membrane fluidity [16]. Although several studies use the thin-film hydration method for encapsulation of proteins [17,18], the ethanolic injection method was chosen to prepare bLf-loaded AMLs, as this method is also suitable for protein encapsulation, is easier to use and does not require the use of toxic solvents such as chloroform [19].

On the other hand, bLf-loaded SMLs were obtained through a bioconjugation reaction between PEG molecules and bLf, after incubation. The choice of this strategy was motivated by the fact that SMLs solid core does not allow the encapsulation of a molecule with such big dimensions as a protein. Thus, an innovative method reported by Padiya *et al.* [20] was used to perform an imidazolecarbonylation of an amine in water. This way, conjugation of PEGylated SMLs with bLf in water is possible. Schematic representations of the expected configuration of the prepared magnetoliposomes with bLf are represented in figure 4.5.

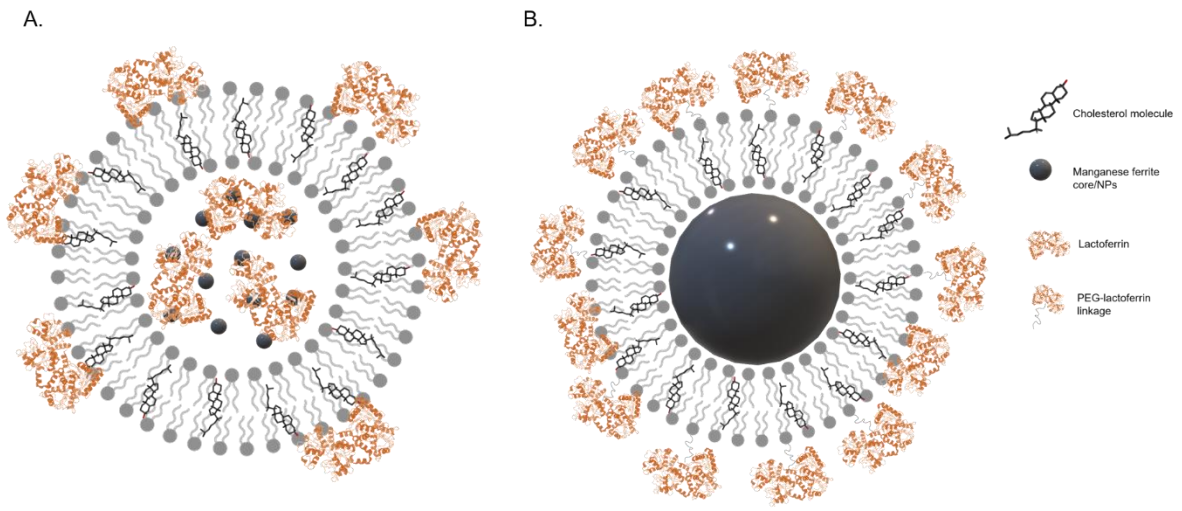

Figure 4.5. Schematic representation of bLf-loaded aqueous magnetoliposomes (A) and solid magnetoliposomes (B). In AMLs, bLf is entrapped in the aqueous core but can be also adsorbed in the inner and outer lipid layers by electrostatic interactions. In SMLs, free amino groups of bLf are conjugated to the carboxylic groups of PEGylated lipid.

4.2.2. Fluorescence emission of bLf in magnetoliposomes

The incorporation of bLf in both AMLs and SMLs was monitored by fluorescence emission. UV absorption and emission bands are due to the presence of fluorescent amino acids like tryptophan, phenylalanine and tyrosine [21]. Figure 4.6 shows the fluorescence spectra of bLf (6 μM) in liposomes (without magnetic nanoparticles), in AMLs and SMLs. The obtained emission bands at λ=325 nm correspond to bLf fluorescence, indicating that this protein is present in the nanosystems. It can be observed a strong quenching effect of fluorescence emission by the magnetic nanoparticles, as previously reported for fluorescent drugs encapsulated in magnetoliposomes [2,22], which also indicates that bLf is incorporated in magnetoliposomes. The quenching effect is slightly higher in SMLs, however very similar in both types of magnetoliposomes, indicating that bLf is, in average, in an analogous location in both types of magnetoliposomes, probably at the water/bilayer interface.

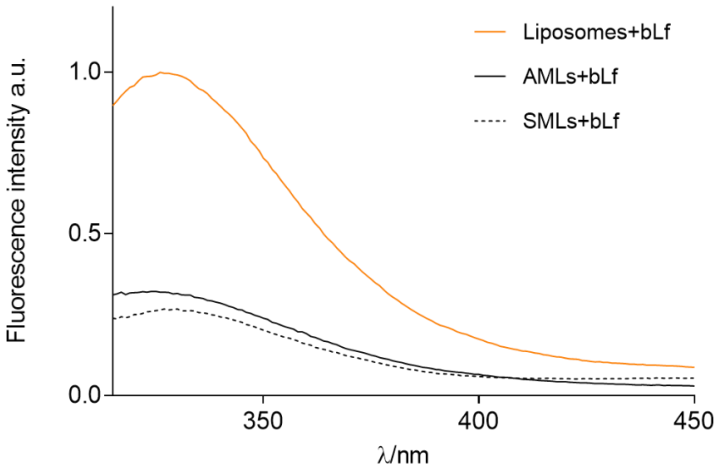

Figure 4.6. Fluorescence spectra of bLf-loaded liposomes (without magnetic nanoparticles) and bLf-loaded magnetoliposomes (λ_{exc}=270 nm).

4.2.3. Formation of the lipid bilayer in solid magnetoliposomes

The formation of the lipid bilayer in SMLs was confirmed by FRET assays, considering that this bilayer is constructed, layer by layer, around a cluster of magnetic nanoparticles [2,22]. For that purpose, the membrane probe DPH (1,6-diphenylhexatriene) was included in the first lipid layer, acting as the energy acceptor, while bLf was incorporated together with the second (outer) lipid layer, acting as the energy donor.

Fluorescence spectra of SMLs with both DPH and bLf and with only bLf were obtained, exciting only the energy donor, bLf (figure 4.7). Comparing the emission of SMLs with both bLf and DPH with the emission of SMLs with only bLf, it can be observed a decrease in bLf fluorescence around 345 nm and the presence of DPH fluorescence in the wavelength range of 450 – 490 nm. This effect is caused by the direct energy transfer from bLf to DPH. To confirm that DPH emission results from excitation of bLf only, emission of SMLs with only DPH was obtained using the same excitation wavelength as the one used to excite bLf (λ_{exc}=270 nm). The emission of DPH is negligible in this case, supporting the fact that the DPH fluorescence observed in SMLs with both fluorophores is a result of energy transfer from bLf. The calculated fluorescence quantum yield (Φ_D^0) of bLf using equation 3.2 was 0.05±0.02. A FRET efficiency of 39% and a donor-acceptor distance (r) of 3.6 nm were calculated from equations 3.3 to 3.6. This donor-acceptor distance is in accordance with one already obtained for SMLs containing magnetite nanoparticles [22], which is smaller than the usual thickness of a biological membrane (7-9 nm) [23], indicating the proximity of the two fluorophores and evidencing the formation of the lipid bilayer.

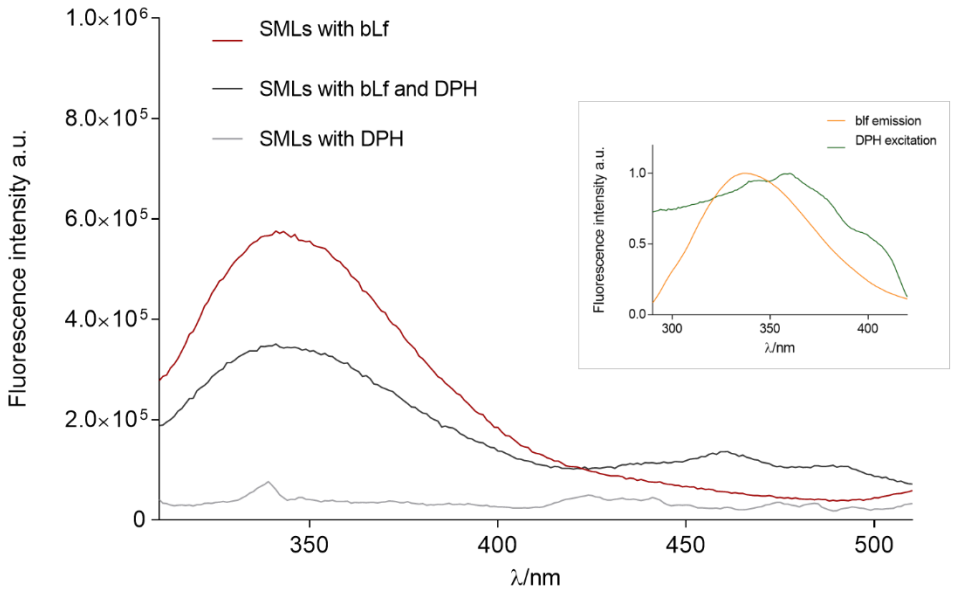

Figure 4.7. Fluorescence spectra (λ_{exc}=270 nm) of Egg-PC/chol (8:2) SMLs based on $MnFe_2O_4$ nanoparticles containing only DPH (100 μM), only bLf (100 μM) and SMLs containing both DPH and bLf. Inset: Spectral overlap (spectra are normalized) between bLf emission and DPH excitation.

4.2.4. Interaction of bLf-loaded magnetoliposomes with model membranes

Interaction of bLf-loaded AMLs and SMLs with Giant Unilamellar Vesicles (GUVs), working as cell membrane models, was evaluated through fluorescence measurements. If magnetoliposomes interact with GUVs, a larger membrane would be formed by fusion [22], and distance between bLf and magnetic nanoparticles will increase, with a corresponding decrease of fluorescence quenching caused by the nanoparticles. Comparing bLf emission in AMLs and SMLs before and after interaction with GUVs, it can be observed an increase of bLf fluorescence in both formulations after interaction, indicating an unquenching effect that arises from the increase in distance between bLf and magnetic nanoparticles, which confirms fusion of bLf-loaded AMLs and SMLs with GUVs (figure 4.8).

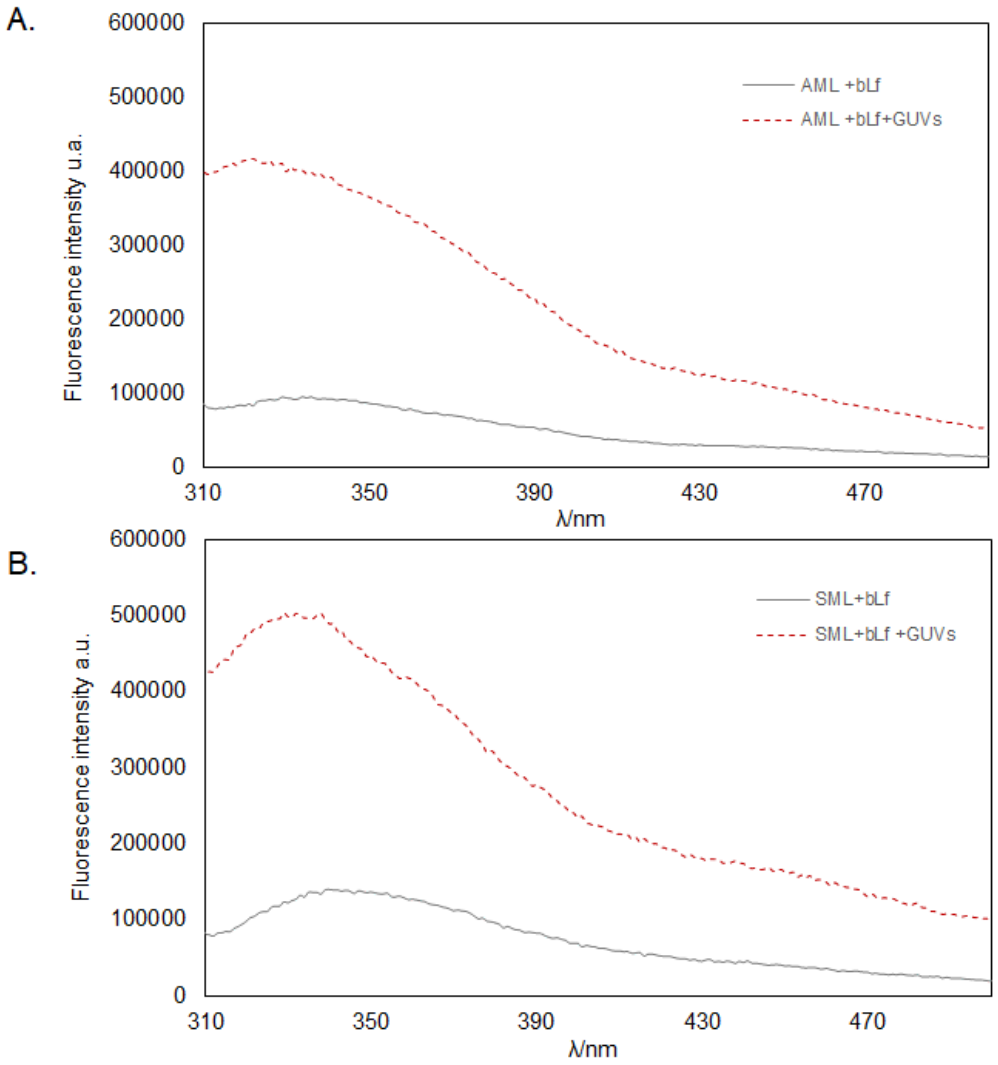

Figure 4.8. Fluorescence spectra of bLf (100 μM)-loaded AMLs (A) and SMLs (B) before and after interaction with GUVs.

4.2.5. Encapsulation efficiency of bLf

The encapsulation efficiency of bLf in magnetoliposomes was assessed by UV/Visible absorption spectroscopy measurements. Absorption spectra of bLf standard solutions in ultrapure water with concentrations from 1.35 μM to 62.5 μM were obtained (figure 4.9). The wavelength corresponding to maximum intensity was found to be 282 nm. A calibration curve was constructed plotting absorbance (at λ=282 nm) *versus* bLf concentration (figure 4.10). A linear trend line was fitted to the data and equation 4.2 was obtained. The determination coefficient (R^2) was close to unity (R^2=0.9992), which means that absorbance is proportional to concentration, in this bLf concentration range.

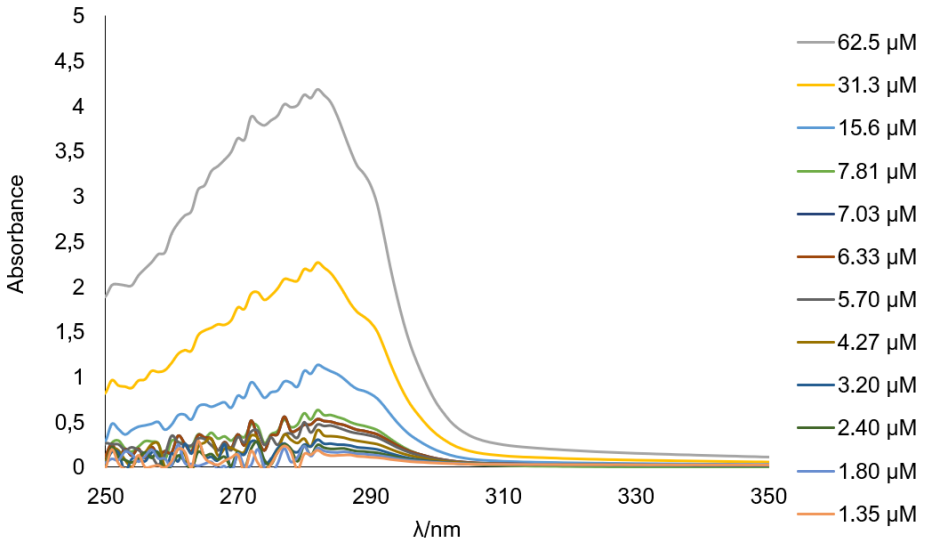

Figure 4.9. Absorption spectra of bLf solutions with different concentrations.

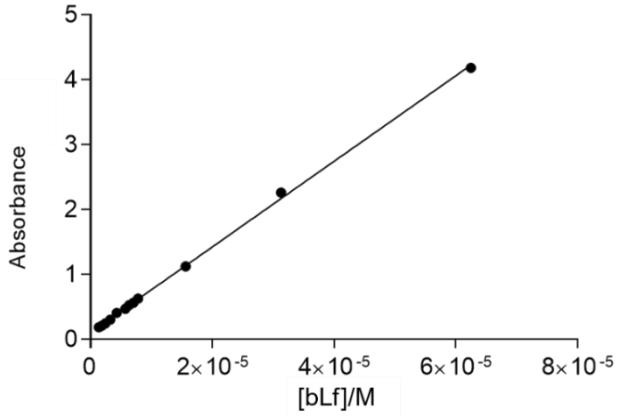

Figure 4.10. Calibration curve for bLf quantification in magnetoliposomes.

$$y = 65893x + 0.109 \qquad (4.2)$$

Absorbances at λ=282 nm of supernatants of each magnetoliposomes solution containing bLf were obtained and the calculated encapsulation efficiencies of both AMLs and SMLs, with the respective bLf concentrations, are listed in table 4.2. AMLs show an encapsulation efficiency higher than the ones reported before for bLf-loaded liposomes [19,24]. In the case of SMLs, bLf was not encapsulated, but the association efficiency was calculated similarly. SMLs present lower values of EE% than AMLs, indicating that the latter can transport a larger amount of bLf. Other explanation could be the low efficiency of conjugation between the protein and PEG molecules.

Table 4.2. Encapsulation efficiencies (EE%) and final bLf concentrations in bLf-loaded AMLs and SMLs. Values represent mean ± SD (standard deviation) of three independent experiments.

	EE (%) ± SD	$[bLf]_f$ (μM)
AMLs+bLf	62 ± 8	62
SMLs+bLf	44 ± 20	44

4.2.6. Fluorescence anisotropy of bLf in magnetoliposomes

Fluorescence anisotropy measurements of bLf-loaded magnetoliposomes were carried out to achieve a better understanding on the location of bLf in liposomes and magnetoliposomes (table 4.3). Anisotropy values are strongly influenced by the rotational diffusion of fluorophores in a certain environment. Thus, in a viscous environment, the fluorophore will rotate more slowly than in a fluid solution, resulting in higher anisotropy values (for the same excited-state lifetime) [25].

bLf anisotropies in the highly viscous solvent glycerol (viscosity around 1000 cP [26]) and in water were also measured for comparison with lipid membranes, that exhibit lower viscosities (100-200 cP [27,28]) than glycerol. In water, the fluorescence anisotropy is expected to be negligible for a small molecule but can be significant for a large protein molecule like bLf. Low values of fluorescence anisotropies may also be justified by the fact that Egg-PC has a melting transition temperature of -18 °C [29], being in its fluid phase at room temperature, resulting in smaller rotational correlation times of the fluorophore. Fluorescence anisotropy of bLf in AMLs is slightly lower than the one obtained for liposomes and only slightly higher than the value in water. These values allow to infer that bLf in AMLs is, in average, located in a water-rich and fluid environment. On the other hand, bLf in SMLs shows a higher fluorescence anisotropy when compared to AMLs and liposomes, which was expected, as bLf is conjugated with the SMLs PEG layer, this implying a hindered rotation. The relatively low r value in glycerol (considering the viscosity of this solvent), indicates that, probably, bLf is denaturated in this highly viscous fluid or that intramolecular interactions occur, leading to a fluorescence depolarization.

Table 4.3. Fluorescence anisotropy values (r) of bLf incorporated in different solvents and nanosystems.

Environment	r
Liposomes	0.142
AMLs	0.123
SMLs	0.145
Water	0.114
Glycerol	0.170

4.2.7. Dynamic light scattering (DLS) and electrophoretic light scattering (ELS) measurements

Magnetoliposomes were prepared with the same method described before. Dynamic Light Scattering and Electrophoretic Light Scattering measurements were performed to obtain information about size and charge parameters such as hydrodynamic size, polydispersity index (PdI) and surface charge, which are important factors that influence the pharmacokinetics of nanocarriers. These parameters are obtained mainly from two different approaches that are used to fit the autocorrelation function, the cumulants fit and CONTIN (*constrained regularization method for inverting data*) fit [30]. While the cumulants analysis provides mean values of diffusion coefficients, the CONTIN method fits multiple exponential equations to the autocorrelation function giving rise to a particle diameter distribution [30,31]. Table 4.4 describes the obtained mean hydrodynamic size, polydispersity index and zeta potential of unloaded and bLf-loaded magnetoliposomes.

Table 4.4. Mean values of hydrodynamic size, polydispersity index and zeta potential of unloaded and bLf-loaded AMLs and SMLs. SD: Standard Deviation of three independent measurements.

	Hydrodynamic size ± SD (nm)	PdI ± SD	Zeta potential ± SD (mV)
AML	92 ± 11	0.196 ± 0.05	-15.3 ± 2
AML+ bLf	148 ± 23	0.220 ± 0.06	-10.9 ± 0.9
SML	107 ± 16	0.185 ± 0.04	-21.4 ± 3
SML+ bLf	164 ± 31	0.232 ± 0.08	-2.1 ± 0.8

The obtained hydrodynamic sizes for AMLs and SMLs without bLf are in accordance with the ones reported before for magnetoliposomes (aqueous and solid) of the same lipids and similar nanoparticles [2,22,32]. Both bLf-loaded AMLs and SMLs present larger sizes than the ones without the protein, as expected, this being a further indication of bLf incorporation, as seen in previous studies of liposomes incorporating lactoferrin [33-35]. The higher PdI values in bLf-loaded magnetoliposomes indicate that these nanosystems have a larger size distribution. Zeta potential values for AMLs and SMLs without bLf are significantly negative, as already reported for similar liposome formulations (without magnetic nanoparticles) [36]. Both bLf-loaded AMLs and SMLs show a much less negative zeta potential comparing to the ones without protein, due to the positively charged lactoferrin surface, also confirming the incorporation of lactoferrin [33,35]. Therefore, the bLf-loaded magnetoliposomes exhibit slightly negatively charged surfaces. It has been demonstrated that nanoparticles with slightly negative surface charges have a higher affinity for tumor cells and tend to accumulate more efficiently in tumor vasculature [37,38], which supports the use of these type of nanosystems for cancer therapy.

4.3. Biological activity of bLf-loaded magnetoliposomes

To address whether the biological activity of bLf could be improved by incorporation in magnetoliposomes, we first used yeast as a simple eukaryotic cell model. Indeed, it was previously shown that *Saccharomyces cerevisiae*, like mammalian cell lines, undergoes an apoptotic-like cell death process and exhibits typical cellular markers of mammalian apoptosis upon treatment with bLf [39-41]. Since during magnetoliposomes preparation, bLf can be exposed to relatively high temperatures (above 40 ºC), depending on the lipid used, the influence of temperature on the activity of this protein was evaluated before assessing its activity against yeast cells.

4.3.1. bLf activity is affected by high temperatures

Lactoferrin is sensitive to high temperatures, undergoing denaturation above 60 ºC. Two denaturation temperatures were reported, one at 60 ºC and the other at 90 ºC, which result from different heat sensitivities of the N and C lobes of lactoferrin, respectively [42,43]. It was shown by Bengoechea *et al.* [42] that when lactoferrin is heated at a temperature between the two denaturation temperatures, the N lobe unfolds while the C lobe remains intact, and when it is heated with temperatures above 90 ºC, it undergoes a complete irreversible denaturation. Additionally, Paulsson *et al.* [44] demonstrated that the thermal peaks at 60 ºC and 90 ºC correspond to the apo- and holo-forms of lactoferrin, respectively.

The need of heating during liposome preparation is because some lipids require manipulation at temperatures higher than the melting transition temperature (T_m). In order to study the influence of temperature increase on bLf biological activity, yeast cells were incubated with bLf pre-heated at 60 ºC and 90 ºC and the effect was compared with that of bLf at room temperature. Spot assay analysis (figure 4.11) shows that after 90 minutes of treatment, the activity of both heated bLf samples is affected. However, a slight difference in cell density can be observed between the two temperatures, being bLf heated at 60 ºC more affected than the one heated at 90 ºC. Heat treatment at 60 ºC did not produce a significant yeast cell death, which possibly results from denaturation of the N lobe. The N-terminus of lactoferrin is known to contain sequences of amino acids with potent antimicrobial activity, such as lactoferricin B and lactoferrampin [45,46]. Denaturation of N lobe can lead to conformational changes and inactivation of these peptides. On the other hand, when lactoferrin is heated at 90 ºC, the protein is almost completely denatured, but it shows higher antifungal activity than when is heated at 60 ºC. A possible explanation to this could be the fact that complete denaturation of bLf can cause its unfolding and expose of antifungal peptides [45,47,48]. These results demonstrate that in the preparation of

magnetoliposomes, lipids (or lipid mixtures) with low phase transition temperature, like Egg-PC, used in this work, are more suitable for conjugation with bLf.

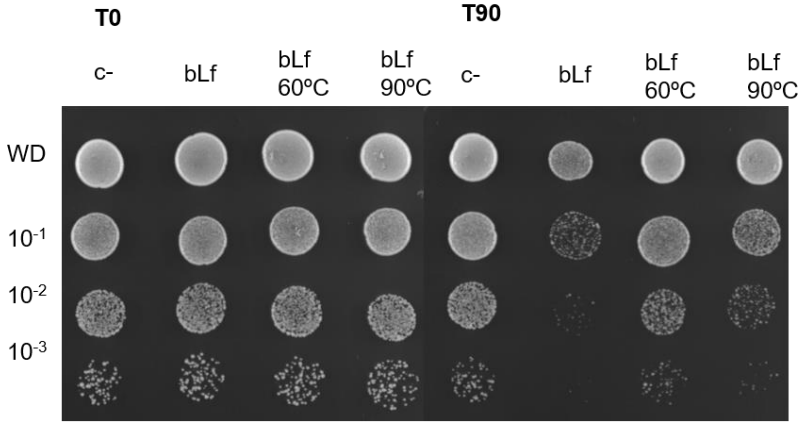

Figure 4.11. Spot assay analysis of *S. cerevisiae* growth on YPD medium incubated with unheated bLf 5 μM (bLf), bLf pre-heated at 60 ºC (bLf 60 ºC) or at 90 ºC (bLf 90 ºC). A control consisting of yeast cells not submitted to heating is also shown (c-). Abbreviations: WD – without dilution.

4.3.2. bLf-loaded magnetoliposomes do not affect yeast cells viability

For these experiments, two controls were performed: a negative control consisting of cells without addition of any compound and a positive control of cells incubated with free bLf 5 μM. First, four different dilutions (1:2, 1:5, 1:10, 1:20) of unloaded and bLf-loaded magnetoliposomes were prepared from a stock solution 1× and tested in yeast cells. As it can be observed in figure 4.12, free bLf is capable of inducing yeast cell death after 90 min. In contrast, any of the prepared dilutions of both unloaded and bLf-loaded AMLs and SMLs affected yeast survival (figure 4.13.A and 4.13.B). These results suggested that the amount of bLf-loaded in magnetoliposomes was not enough to induce cell death. In the next experiment, it was chosen the dilution 1:2 (highest concentration) to test the influence of a higher concentration of both magnetoliposomes (stock 5×) and bLf (250 μM). However, bLf-loaded magnetoliposomes, even with a bLf loading of about 50 times higher than the positive control concentration, did not affect yeast cell growth in comparison with unloaded magnetoliposomes (figure 4.14). One explanation for this behavior could be the lack of internalization of magnetoliposomes due to the occurrence of agglomerates (high PdI values) that difficult their passage through the cell wall or plasma membrane of yeast cells.

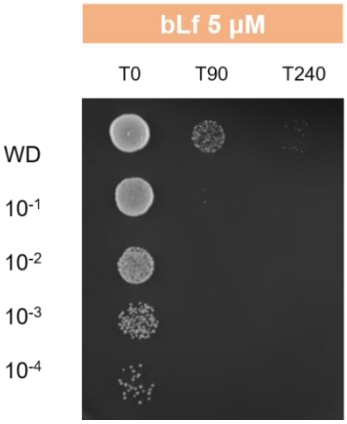

Figure 4.12. Effect of free bLf on *S. cerevisiae* growth on YPD medium. Yeast cells incubated with bLf 5 µM for 0 (T0), 90 (T90) and 240 (T240) min.

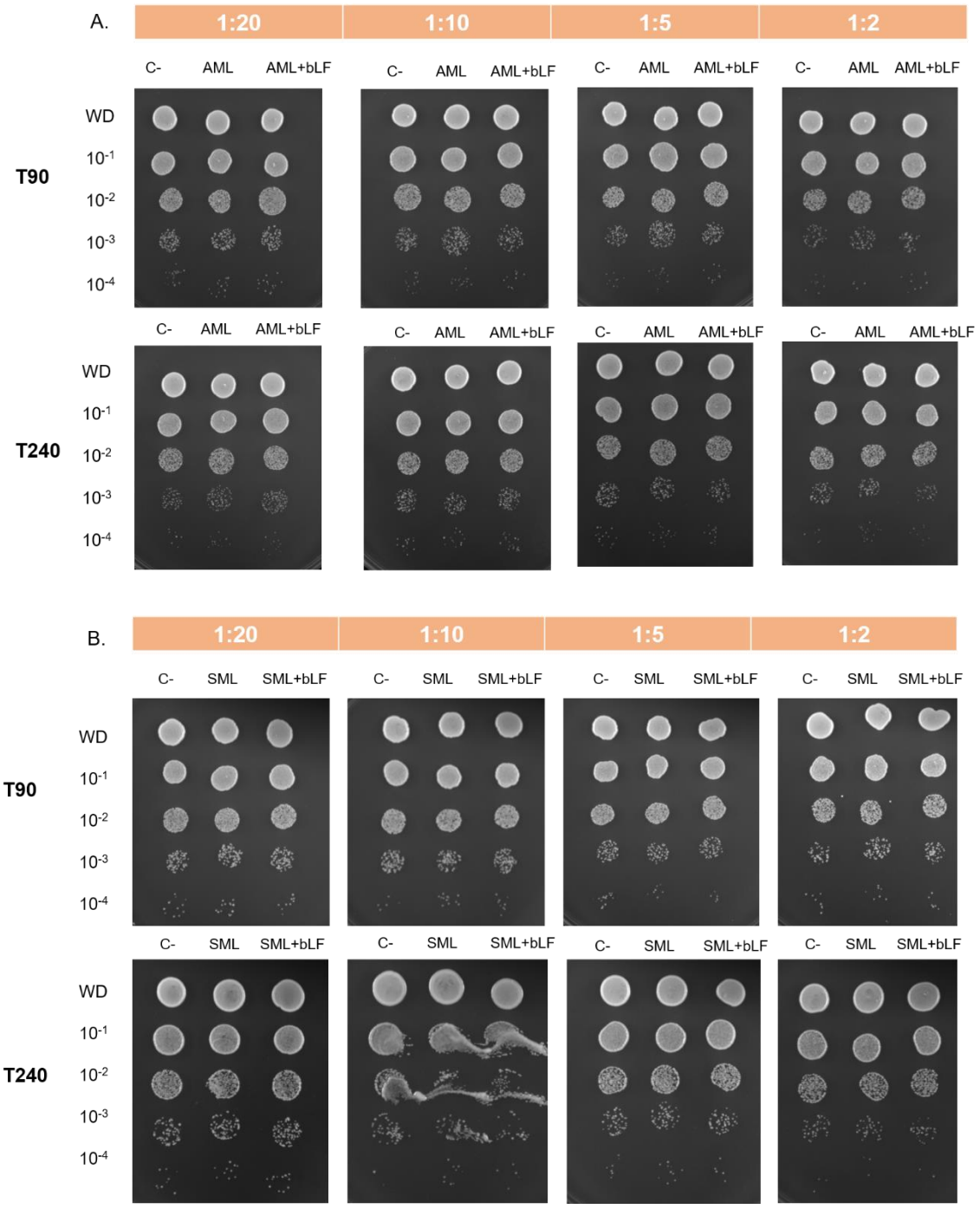

Figure 4.13. Effect of bLf-loaded magnetoliposomes on *S. cerevisiae* growth on YPD medium. Yeast cells were incubated with unloaded and bLf (20 μM)-loaded AMLs (A) and SMLs (B) (from stock 1×), at timepoints 90 min and 240 min. For each incubation, control solutions with only cells were used to compare with other conditions.

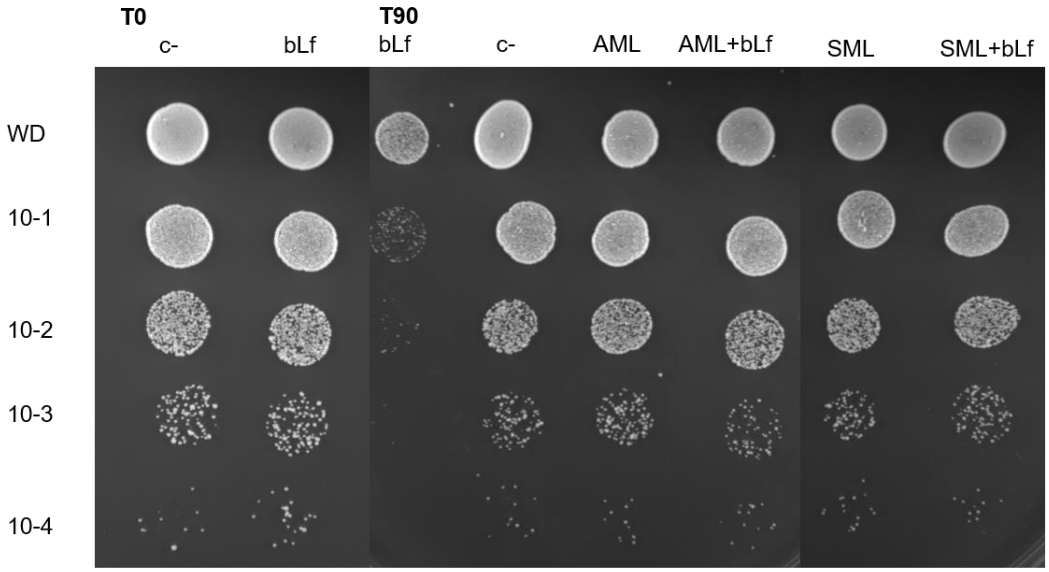

Figure 4.14. Effect of bLf-loaded magnetoliposomes on *S. cerevisiae* growth on YPD medium. Cells were incubated with unloaded AMLs (AML), AMLs loaded with bLf 250 μM (AML+bLf), unloaded SMLs (SML) and SMLs loaded with bLf 250 μM (SML+bLf), all taken from stock 5×. Controls with only cells (c-) and cells incubated with bLf 5 μM. Abbreviations: WD – without dilution.

4.3.3. Effect of bLf-loaded magnetoliposomes in non-tumorigenic cells and breast cancer cells

Since the developed bLf-loaded magnetoliposomes revealed no activity against *S. cerevisiae*, we sought to test their activity against the human breast cancer cell line Hs 578T and the non-tumorigenic breast cell line MCF-10-2A, to evaluate if the well-known bLf anticancer activity [49-51] could be maintained/enhanced when incorporated in these nanosystems. The two selected breast cell lines were chosen because their sensitivity and resistance to bLf was previously demonstrated [49].

The first step was to study the *in vitro* cytotoxicity of the unloaded magnetoliposomes and to select the concentration range most suitable for further experiments using the sulforhodamine B (SRB) assay. Sulforhodamine B is a bright-pink dye that binds to protein content of the cells through its sulfonic acid groups and basic amino acid residues [52]. The binding of SRB is stoichiometric, thus the amount of dye retained by the cells is directly proportional to the cell mass, making possible to assess the cytotoxicity effects of a given compound of interest.

Results showed that unloaded AMLs did not present any toxic effect on the highly metastatic breast cancer cells Hs 578T (figure 4.15.A), as well as on the non-tumorigenic cell line MCF-10-2A (figure 4.15.C). The same was observed for unloaded SMLs (figure 4.15.B and 4.15.C). Unloaded AMLs and SMLs are

therefore suitable for testing in these type of cancer cells, as they do not show any cytotoxic effect, for the concentrations tested. It is noteworthy that they are not toxic to the non-tumorigenic cells, which makes them biocompatible and opens the possibility to explore, in the future, these nanosystems for therapeutic applications. These results are in accordance with the previously reported non-toxicity of similar nanosystems (containing also $MnFe_2O_4$ nanoparticles) in primary non-tumor cells [53].

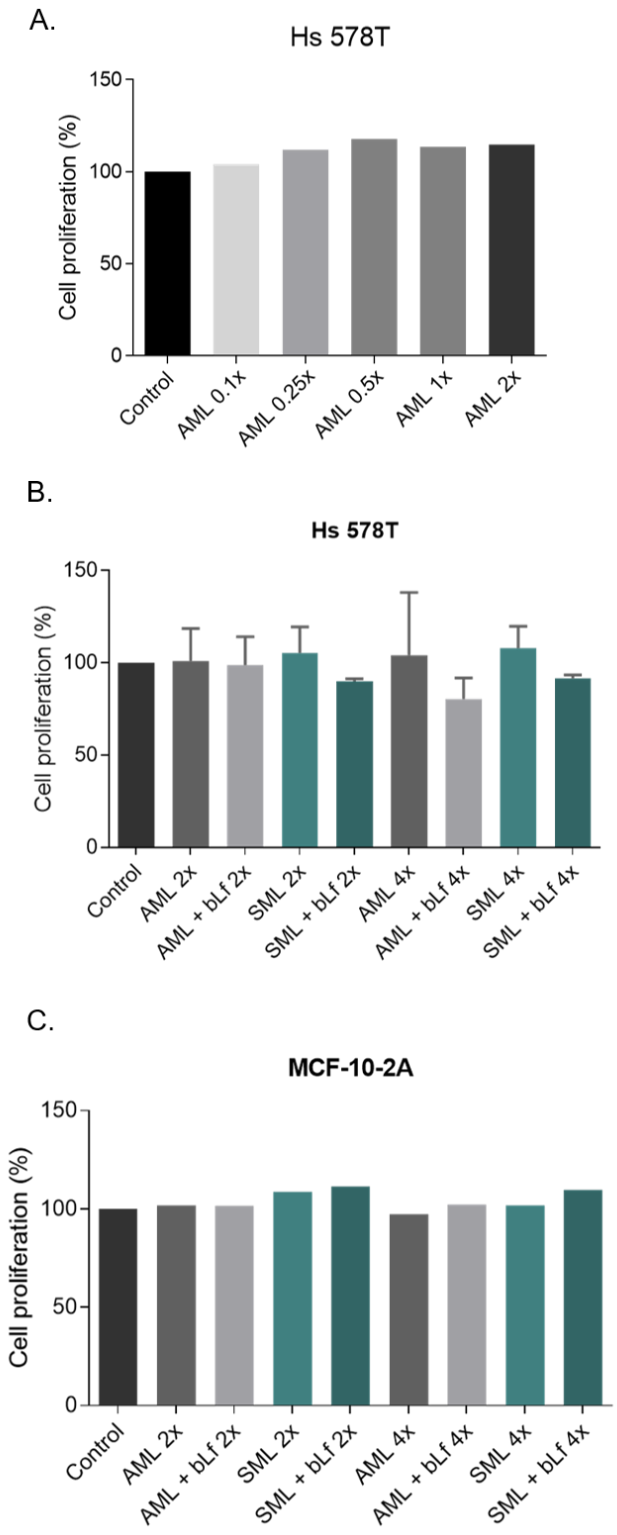

Figure 4.15. Effect of unloaded and bLf-loaded magnetoliposomes on cell proliferation of breast cancer cells and non-tumorigenic breast cell lines. A. Analysis of cell proliferation of Hs 578T with different concentrations of AMLs for 48h. The different dilutions of magnetoliposomes were obtained from a stock of 5×. **B**. Analysis of cell proliferation of Hs 578T incubated with unloaded and bLf-loaded AMLs 2× and 4×, and with unloaded and bLf-loaded SMLs 2× and 4×, for 48h. **C.** Analysis of cell proliferation of MCF-10-2A cells in the same conditions as in B. For all three experiments, proliferation was estimated by the SRB assay in relation to untreated cells (considered to have 100% proliferation). Values in A and C represent one experiment and in B represent mean ± SD of two independent experiments.

The next experiment consisted in analyzing the effect of bLf (250 μM)-loaded magnetoliposomes (AMLs+bLf and SMLs+bLf), on the proliferation of the Hs 578T and MCF-10-2A cells. Though, AMLs+bLf 2× did not show any effect on cell proliferation, AMLs+bLf 4× promoted a cell proliferation decrease of about 24%, while SMLs+bLf 2× and 4× caused a similar decrease of about 15%, after 48h of treatment (figure 4.15.B). These results were unexpected since in accordance with the recognized anticancer activity of bLf, a 50% decrease of cell proliferation with 175 μM free bLf, was previously reported [49]. Low cytotoxic effects were also obtained by Pereira *et al*. [54], which studied the inhibitory activity of drug-loaded magnetoliposomes on breast cancer cells.

bLf-loaded SMLs showed a slightly lower cytotoxicity than bLf-loaded AMLs, possibly due to their low association efficiency but also to the presence of PEG molecules. It was already reported that liposomal formulations modified with PEG decrease the release of drugs from nanocarriers and difficult liposome-cell interactions due to steric hindrance conferred by PEGylation [55-57]. bLf-loaded AMLs 4× showed a slight decrease in cell viability when compared with the 2× sample, suggesting that activity of bLf is dose-dependent when incorporated in these magnetoliposomes. The preserved stability and the absence of a triggered release may explain the low cytotoxic activity by bLf-loaded magnetoliposomes. In fact, these magnetic nanosystems were designed for a triggered release by local heating (and corresponding increase of membrane fluidity), promoted by the application of an alternating magnetic field (AMF) [54]. Therefore, in future experiments, the bLf-loaded magnetoliposomes (without the application of AMF) will act as control. Cell proliferation of MCF-10-2A did not decreased after exposure to bLf-loaded AMLs and SMLs, which is in agreement with the resistance of these cells to bLf [49,51]. One might not forget the influence that manganese ferrite nanoparticles can have on lactoferrin. Mahmoudi *et al.* [58] reported that the interaction of human transferrin with superparamagnetic iron oxides can lead to irreversible conformational changes of the protein from a compact to an open structure, associated to the release of iron. In order to assess if conformational changes promoted by magnetic nanoparticles have influence in the cytotoxic activity of lactoferrin, cell viability studies in which cells are incubated with nanoparticles with adsorbed lactoferrin, must be performed.

4.3.4. Unloaded and bLf-loaded AMLs and SMLs are internalized by breast cancer cells and non-tumorigenic breast cancer cells

To address whether the reduced or absence of cytotoxicity of bLf-loaded AMLs and SMLs against Hs 578T and MCF-10-2A cells was due to a reduced internalization of both types of magnetoliposomes, their cellular uptake was monitored by fluorescence microscopy. For that purpose, the hydrophobic dye Nile Red was incorporated in the lipid membranes of AMLs and SMLs before incubation of Hs 578T and MCF-10-2A cells, for 48h. Nile Red is usually used to detect lipid content in the cytoplasm because of its intense fluorescence in lipidic environment [62]. Bright-field images of cells incubated with unloaded AMLs show the typical dark agglomerates of manganese ferrite nanoparticles localized in the cell's cytoplasm (figure 4.16, white arrows), suggesting internalization of magnetoliposomes, after 48 h, in accordance with previous studies [59-61].

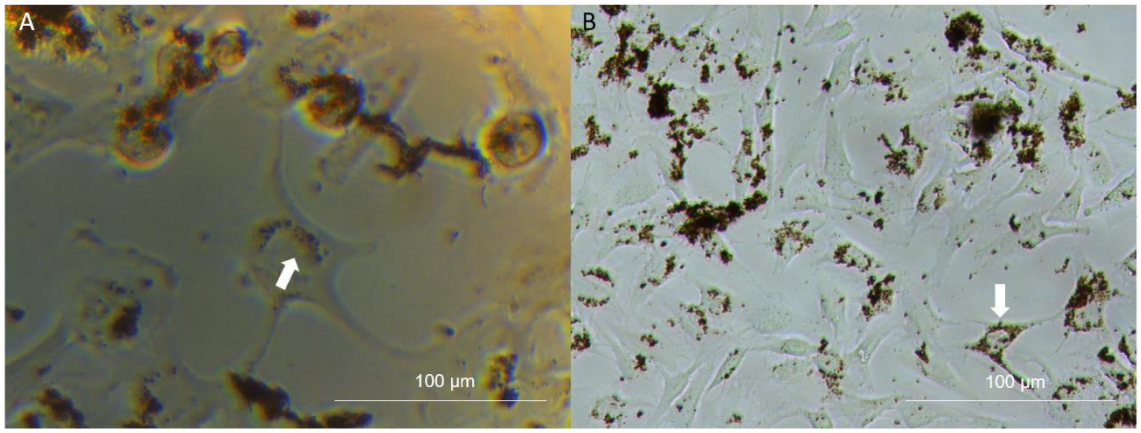

Figure 4.16. Bright-field photomicrographies of *in vitro* Hs 578T cells uptake of unloaded AMLs with objective ampliations of 40x (A) and 20x (B). White arrows evidence the presence of dark agglomerates of manganese ferrite nanoparticles.

Fluorescence images show a common diffuse staining with occurrence of some punctual brighter spots in the cytoplasm [63] which co-localize with nanoparticles agglomerates in bright-field images, evidencing magnetoliposomes internalization in both types of cells (figure 4.17). A higher number of cells with fluorescence is observed for AMLs, demonstrating a higher internalization efficiency than that of SMLs. As mentioned before, the lower internalization of SMLs could be due to the presence of PEG molecules that difficult interaction with cell membrane. Besides that, bLf-loaded SMLs showed the highest hydrodynamic size in DLS measurements, which can difficult their cellular uptake. Also, it is possible that SMLs undergo a different cellular uptake behavior, via receptor-mediated binding of bLf that is linked to PEG molecules in the surface of SMLs [64]. Although several studies demonstrated an improved cellular uptake with lactoferrin-modified liposomes comparing with plain liposomes [31,33,64,65], both unloaded

and bLf-loaded magnetoliposomes have similar fluorescence occurrence, suggesting that, in this case, the presence of bLf did not enhanced the cellular uptake. Internalization of unloaded and bLf-loaded magnetoliposomes also occur for MCF-10-2A cells. However, as concluded before, bLf-loaded magnetoliposomes did not promote cytotoxic effects in this cell line, indicating that their internalization does not affect the viability of MCF-10-2A cells and can effectively target breast cancer cells trough bLf. Internalization of both bLf-loaded AMLs and SMLs in Hs 578T cells is observed, however their cytotoxic effect was not demonstrated. This leads to the assumption that bLf loaded in magnetoliposomes is not fully active or, more probably, is not being effectively released. This last hypothesis corroborates the already mentioned need of a triggered release by rising of temperature, with application of an external magnetic field, or pH-stimulated release of liposomal content [66]. Several studies have demonstrated that internalization of nanoparticles occur via endocytosis ending up inside of endosomes in the cytosol [67-71]. The red fluorescent spots can be related with transport of labeled magnetoliposomes inside cytoplasmic vesicles. Indeed, it was previously reported before that nanoparticles with modified surface and liposomes promote a caveolae and clathrin-mediated endocytosis [70,72]. In addition, it was demonstrated that cellular uptake of bLf-modified liposomes is enhanced through receptor-mediated endocytosis [65]. Therefore, these could be the mechanisms of magnetoliposomes internalization in the cells under study.

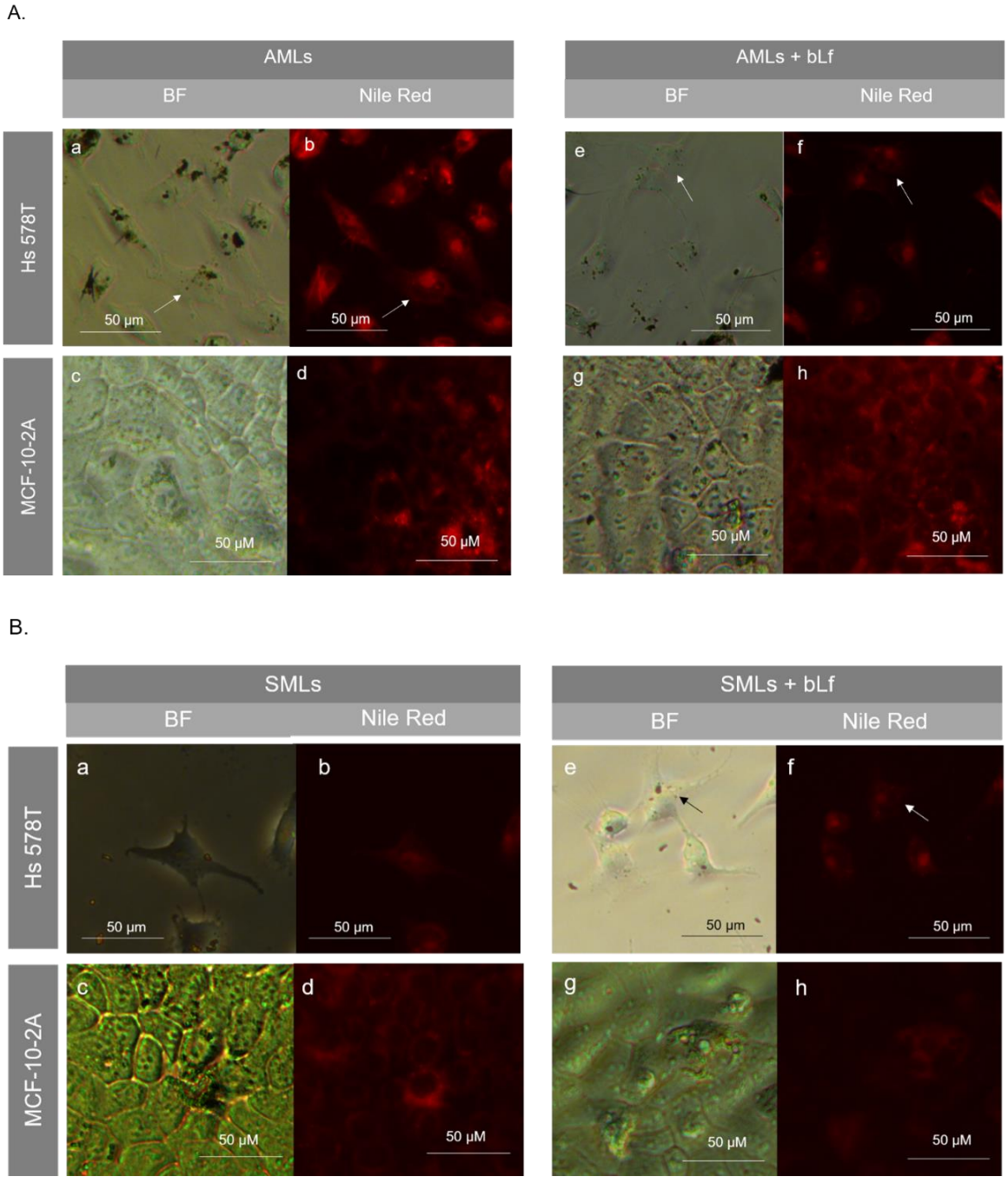

Figure 4.17. Analysis of AMLs and SMLs internalization in breast cancer and non-tumorigenic cell lines. Bright-field (BF) (a, c, e, g) and fluorescence photomicrographies (b, d, f, h) of *in vitro* Hs 578T and MCF-10-2A cells after incubation with unloaded and bLf-loaded AMLs (A) and SMLs (B), for 48h. The red fluorescence is from Nile Red. Arrows indicate the colocalized nanoparticles agglomerates with bright red spots.

4.4. References

[1] Ahmed, M., Okasha, N. and El-Dek, S. (2008). Preparation and characterization of nanometric Mn ferrite via different methods. *Nanotechnology*, 19, 1-6.

[2] Rodrigues, A., Ramos, J., Gomes, I., Almeida, B., Araújo, J., Queiroz, M., Coutinho, P. and Castanheira, E. (2016). Magnetoliposomes based on manganese ferrite nanoparticles as nanocarriers for antitumor drugs. *RSC Advances*, 6, 17302-17313.

[3] Rafique, M., Pan, L., Javed, Q., Iqbal, M., Qiu, H., Farooq, M., Guo, Z. and Tanveer, M. (2013). Growth of monodisperse nanospheres of MnFe2O4with enhanced magnetic and optical properties. *Chinese Physics B*, 22, 1-7.

[4] Goodarz Naseri, M., Saion, E., Ahangar, H., Hashim, M. and Shaari, A. (2011). Synthesis and characterization of manganese ferrite nanoparticles by thermal treatment method. *Journal of Magnetism and Magnetic Materials*, 323, 1745-1749.

[5] Dong, C., Wang, G., Shi, L., Guo, D., Jiang, C. and Xue, D. (2012). Investigation of the thermal stability of Mn ferrite particles synthesized by a modified co-precipitation method. *Science China Physics, Mechanics and Astronomy*, 56, 568-572.

[6] Makridis, A., Topouridou, K., Tziomaki, M., Sakellari, D., Simeonidis, K., Angelakeris, M., Yavropoulou, M., Yovos, J. and Kalogirou, O. (2014). In vitro application of Mn-ferrite nanoparticles as novel magnetic hyperthermia agents. *J. Mater. Chem. B*, 2, 8390-8398.

[7] Dong, C., Wang, G., Shi, L., Guo, D., Jiang, C. and Xue, D. (2012). Investigation of the thermal stability of Mn ferrite particles synthesized by a modified co-precipitation method. *Science China Physics, Mechanics and Astronomy*, 56, 568-572.

[8] Doaga, A., Cojocariu, A., Amin, W., Heib, F., Bender, P., Hempelmann, R. and Caltun, O. (2013). Synthesis and characterizations of manganese ferrites for hyperthermia applications. *Materials Chemistry and Physics*, 143, 305-310.

[9] Nikolic, A., Boskovic, M., Spasojevic, V., Jancar, B. and Antic, B. (2014). Magnetite/Mn-ferrite nanocomposite with improved magnetic properties. *Materials Letters*, 120, 86-89.

[10] Kodama, R. (1999). Magnetic nanoparticles. *Journal of Magnetism and Magnetic Materials*, 200, 359-372.

[11] Khanna, L. and Verma, N. (2013). Synthesis, characterization and in vitro cytotoxicity study of calcium ferrite nanoparticles. *Materials Science in Semiconductor Processing*, 16, 1842-1848.

[12] Kumar, C. (2009). *Magnetic nanomaterials*. 1st ed., Wiley-VCH, 1-47.

[13] Yu, M., Jeong, Y., Park, J., Park, S., Kim, J., Min, J., Kim, K. and Jon, S. (2008). Drug-Loaded Superparamagnetic Iron Oxide Nanoparticles for Combined Cancer Imaging and Therapy In Vivo. *Angewandte Chemie International Edition*, 47, 5362-5365.

[14] Mahmoudi, M., Simchi, A., Milani, A. and Stroeve, P. (2009). Cell toxicity of superparamagnetic iron oxide nanoparticles. *Journal of Colloid and Interface Science*, 336, 510-518.

[15] Mahmoudi, M., Sant, S., Wang, B., Laurent, S. and Sen, T. (2011). Superparamagnetic iron oxide nanoparticles (SPIONs): Development, surface modification and applications in chemotherapy. *Advanced Drug Delivery Reviews*, 63, 24-46.

[16] Qin, Y., Chen, H., Zhang, Q., Wang, X., Yuan, W., Kuai, R., Tang, J., Zhang, L., Zhang, Z., Zhang, Q., Liu, J. and He, Q. (2011). Liposome formulated with TAT-modified cholesterol for improving brain delivery and therapeutic efficacy on brain glioma in animals. *International Journal of Pharmaceutics*, 420, 304-312.

[17] Roseanu, A., Florian, P., Moisei, M., Sima, L., Evans, R. and Trif, M. (2010). Liposomalization of lactoferrin enhanced its anti-tumoral effects on melanoma cells. *BioMetals*, 23, 485-492.

[18] Liu, W., Lu, J., Ye, A., Xu, Q., Tian, M., Kong, Y., Wei, F. and Han, J. (2018). Comparative performances of lactoferrin-loaded liposomes under in vitro adult and infant digestion models. *Food Chemistry*, 258, 366-373.

[19] Wang, C. and Huang, Y. (2003). Encapsulating Protein into Preformed Liposomes by Ethanol-Destabilized Method. *Artificial Cells, Blood Substitutes, and Biotechnology*, 31, 303-312.

[20] Padiya, K., Gavade, S., Kardile, B., Tiwari, M., Bajare, S., Mane, M., Gaware, V., Varghese, S., Harel, D. and Kurhade, S. (2012). Unprecedented "In Water" Imidazole Carbonylation: Paradigm Shift for Preparation of Urea and Carbamate. *Organic Letters*, 14, 2814-2817.

[21] Yang, H., Xiao, X., Zhao, X. and Wu, Y. (2017). Intrinsic fluorescence spectra of tryptophan, tyrosine and phenyloalanine. *Selected Papers of the Chinese Society for Optical Engineering Conferences held October and November 2016*, 10255, 224-233.

[22] Rodrigues, A., Mendes, P., Silva, P., Machado, V., Almeida, B., Araújo, J., Queiroz, M., Castanheira, E. and Coutinho, P. (2017). Solid and aqueous magnetoliposomes as nanocarriers for a new potential drug active against breast cancer. *Colloids and Surfaces B: Biointerfaces*, 158, 460-468.

[23] H. Curtis, N. Barnes (1989). *Biology*, 5th ed., Worth Publishers, 104.

[24] Colletier, J., Chaize, B., Winterhalter, M. and Fournier, D. (2002). Protein encapsulation in liposomes: efficiency depends on interactions between protein and phospholipid bilayer. *BMC Biotechnology*, 2, 1-8.

[25] Valeur, B. (2002). *Molecular fluorescence: Principles and Applications*. Wiley-VCH, 1-154.

[26] Lide, D. R. (2009) *Handbook of Chemistry and Physics*, 89th ed., CRCPress/Taylor and Francis, 122.

[27] Israelachvili, J.N., Marcelja, S., Horn, R.G. (1980). Physical principles of membrane organization, *Quarterly Reviews of Biophysocs*, 13, 121–200.

[28] Kell, D. and Harris, C. (1985). On the dielectrically observable consequences of the diffusional motions of lipids and proteins in membranes. *European Biophysics Journal*, 12, 181-197.

[29] Li, J., Wang, X., Zhang, T., Wang, C., Huang, Z., Luo, X. and Deng, Y. (2015). A review on phospholipids and their main applications in drug delivery systems. *Asian Journal of Pharmaceutical Sciences*, 10, 81-98.

[30] Stetefeld, J., McKenna, S., Patel, T. (2016). Dynamic light scattering: a practical guide and applications in biomedical sciences. *Biophysical Reviews*, 8, 409-427.

[31] Arzenšek, D. (2010). *Dynamic light scattering and application to proteins in solutions* (Seminar). University of Ljubljana, 1-19.

[32] Cardoso, B., Rio, I., Rodrigues, A., Fernandes, F., Almeida, B., Pires, A., Pereira, A., Araújo, J., Castanheira, E. and Coutinho, P. (2018). Magnetoliposomes containing magnesium ferrite nanoparticles as nanocarriers for the model drug curcumin. *Royal Society Open Science*, 5,1-15.

[33] Wei, M., Xu, Y., Zou, Q., Tu, L., Tang, C., Xu, T., Deng, L. and Wu, C. (2012). Hepatocellular carcinoma targeting effect of PEGylated liposomes modified with lactoferrin. *European Journal of Pharmaceutical Sciences*, 46, 131-141.

[34] Huang, F., Chen, W., Lee, W., Lo, S., Lee, T. and Lo, J. (2013). In Vitro and in Vivo Evaluation of Lactoferrin-Conjugated Liposomes as a Novel Carrier to Improve the Brain Delivery. *International Journal of Molecular Sciences*, 14, 2862-2874.

[35] Chen, H., Tang, L., Qin, Y., Yin, Y., Tang, J., Tang, W., Sun, X., Zhang, Z., Liu, J. and He, Q. (2010). Lactoferrin-modified procationic liposomes as a novel drug carrier for brain delivery. *European Journal of Pharmaceutical Sciences*, 40, 94-102.

[36] Abreu, A., Castanheira, E., Queiroz, M., Ferreira, P., Vale-Silva, L. and Pinto, E. (2011). Nanoliposomes for encapsulation and delivery of the potential antitumoral methyl 6-methoxy-3-(4-methoxyphenyl)-1H-indole-2-carboxylate. *Nanoscale Research Letters*, 6, 1-6.

[37] Honary, S. and Zahir, F. (2013). Effect of Zeta Potential on the Properties of Nano-Drug Delivery Systems - A Review (Part 2). *Tropical Journal of Pharmaceutical Research*, 12, 265-273.

[38] He, C., Hu, Y., Yin, L., Tang, C. and Yin, C. (2010). Effects of particle size and surface charge on cellular uptake and biodistribution of polymeric nanoparticles. *Biomaterials*, 31, 3657-3666.

[39] Madeo, F., Herker, E., Maldener, C., Wissing, S., Lächelt, S., Herlan, M., Fehr, M., Lauber, K., Sigrist, S., Wesselborg, S. and Fröhlich, K. (2002). A Caspase-Related Protease Regulates Apoptosis in Yeast. *Molecular Cell*, 9, 911-917.

[40] Ludovico, P., Rodrigues, F., Almeida, A., Silva, M., Barrientos, A. and Côrte-Real, M. (2002). Cytochrome *c* release and mitochondria involvement in programmed cell death induced by acetic acid in *Saccharomyces cerevisiae*. *Molecular Biology of the Cell*, 13, 2598-2606.

[41] Acosta-Zaldívar, M., Andrés, M., Rego, A., Pereira, C., Fierro, J. and Côrte-Real, M. (2015). Human lactoferrin triggers a mitochondrial- and caspase-dependent regulated cell death in *Saccharomyces cerevisiae*. *Apoptosis*, 21, 163-173.

[42] Bengoechea, C., Peinado, I. and McClements, D. (2011). Formation of protein nanoparticles by controlled heat treatment of lactoferrin: Factors affecting particle characteristics. *Food Hydrocolloids*, 25, 1354-1360.

[43] Conesa, C., Rota, C., Castillo, E., Pérez, M., Calvo, M. and Sánchez, L. (2010). Effect of heat treatment on the antibacterial activity of bovine lactoferrin against three foodborne pathogens. *International Journal of Dairy Technology*, 63, 209-215.

[44] Paulsson, M., Svensson, U., Kishore, A. and Satyanarayan Naidu, A. (1993). Thermal Behavior of Bovine Lactoferrin in Water and Its Relation to Bacterial Interaction and Antibacterial Activity. *Journal of Dairy Science*, 76, 3711-3720.

[45] González-Chávez, S., Arévalo-Gallegos, S. and Rascón-Cruz, Q. (2009). Lactoferrin: structure, function and applications. *International Journal of Antimicrobial Agents*, 33, 1-8.

[46] Bellamy, W., Takase, M., Wakabayashi, H., Kawase, K. and Tomita, M. (1992). Antibacterial spectrum of lactoferricin B, a potent bactericidal peptide derived from the N-terminal region of bovine lactoferrin. *Journal of Applied Bacteriology*, 73, 472-479.

[47] Wang, B., Timilsena, Y., Blanch, E. and Adhikari, B. (2017). Lactoferrin: Structure, function, denaturation and digestion. *Critical Reviews in Food Science and Nutrition*, 59, 580-596.

[48] Ammons, M. and Copié, V. (2013). Mini-review: Lactoferrin: a bioinspired, anti-biofilm therapeutic. *Biofouling*, 29, 443-455.

[49] Pereira, C., Guedes, J., Gonçalves, M., Loureiro, L., Castro, L., Gerós, H., Rodrigues, L. and Côrte-Real, M. (2016). Lactoferrin selectively triggers apoptosis in highly metastatic breast cancer cells through inhibition of plasmalemmal V-H^+-ATPase. *Oncotarget*, 7, 1-15.

[50] Guedes, J., Pereira, C., Rodrigues, L. and Côrte-Real, M. (2018). Bovine Milk Lactoferrin Selectively Kills Highly Metastatic Prostate Cancer PC-3 and Osteosarcoma MG-63 Cells In Vitro. *Frontiers in Oncology*, 8, 1-12.

[51] Gibbons, J., Kanwar, J. and Kanwar, R. (2015). Iron-free and iron-saturated bovine lactoferrin inhibit survivin expression and differentially modulate apoptosis in breast cancer. *BMC Cancer*, 15, 1-16.

[52] Vichai, V. and Kirtikara, K. (2006). Sulforhodamine B colorimetric assay for cytotoxicity screening. *Nature Protocols*, 1, 1112-1116.

[53] Rodrigues, A., Almeida, B., Rodrigues, J., Queiroz, M., Calhelha, R., Ferreira, I., Pires, A., Pereira, A., Araújo, J., Coutinho, P. and Castanheira, E. (2017). Magnetoliposomes as carriers for promising antitumor thieno[3,2-b]pyridin-7-arylamines: photophysical and biological studies. *RSC Advances*, 7, 15352-15361.

[54] Pereira, D., Cardoso, B., Rodrigues, A., Amorim, C., Amaral, V., Almeida, B., Queiroz, M., Martinho, O., Baltazar, F., Calhelha, R., Ferreira, I., Coutinho, P. and Castanheira, E. (2019). Magnetoliposomes Containing Calcium Ferrite Nanoparticles for Applications in Breast Cancer Therapy. *Pharmaceutics*, 11, 1-21.

[55] Sawant, R. and Torchilin, V. (2012). Challenges in Development of Targeted Liposomal Therapeutics. *The AAPS Journal*, 14, 303-315.

[56] Hong, R., Huang, C., Tseng, Y., Pang, V., Chen, S., Liu, J. and Chang, F. (1999). Direct Comparison of Liposomal Doxorubicin with or without Polyethylene Glycol Coating in C-26 Tumor-bearing Mice: Is Surface Coating with Polyethylene Glycol Beneficial? *Clinical Cancer Research*, 5, 3645-3652.

[57] Mishra, S., Webster, P. and Davis, M. (2004). PEGylation significantly affects cellular uptake and intracellular trafficking of non-viral gene delivery particles. *European Journal of Cell Biology*, 83, 97-111.

[58] Mahmoudi, M., Shokrgozar, M., Sardari, S., Moghadam, M., Vali, H., Laurent, S. and Stroeve, P. (2011). Irreversible changes in protein conformation due to interaction with superparamagnetic iron oxide nanoparticles. *Nanoscale*, 3, 1127-1138.

[59] Villanueva, A., de la Presa, P., Alonso, J., Rueda, T., Martínez, A., Crespo, P., Morales, M., Gonzalez-Fernandez, M., Valdés, J. and Rivero, G. (2010). Hyperthermia HeLa Cell Treatment with Silica-Coated Manganese Oxide Nanoparticles. *The Journal of Physical Chemistry C*, 114, 1976-1981.

[60] Pavlin, M., Bregar, Lojk, Sustar and Veranic, P. (2013). Visualization of internalization of functionalized cobalt ferrite nanoparticles and their intracellular fate. *International Journal of Nanomedicine*, 8, 919-931.

[61] Fortin, J., Gazeau, F. and Wilhelm, C. (2007). Intracellular heating of living cells through Néel relaxation of magnetic nanoparticles. *European Biophysics Journal*, 37, 223-228.

[62] Diaz, G., Melis, M., Batetta, B., Angius, F. and Falchi, A. (2008). Hydrophobic characterization of intracellular lipids in situ by Nile Red red/yellow emission ratio. *Micron*, 39, 819-824.

[63] Greenspan, P., Mayer, E. and Fowler, S. (1985). Nile red: a selective fluorescent stain for intracellular lipid droplets. *The Journal of Cell Biology*, 100, 965-973.

[64] Xu, Y., Guo, X., Tu, L., Zou, Q., Li, Q., Tang, C., Chen, B., Wu, C. and Wei, M. (2015). Lactoferrin-modified PEGylated liposomes loaded with doxorubicin for targeting delivery to hepatocellular carcinoma. *International Journal of Nanomedicine*, 10, 5123-5137.

[65] Chen, H., Qin, Y., Zhang, Q., Jiang, W., Tang, L., Liu, J. and He, Q. (2011). Lactoferrin modified doxorubicin-loaded procationic liposomes for the treatment of gliomas. *European Journal of Pharmaceutical Sciences*, 44, 164-173.

[66] Lee, Y. and Thompson, D. (2017). Stimuli-responsive liposomes for drug delivery. *Wiley Interdisciplinary Reviews: Nanomedicine and Nanobiotechnology*, 9, 1-42.

[67] Xia, T., Kovochich, M., Liong, M., Zink, J. and Nel, A. (2007). Cationic Polystyrene Nanosphere Toxicity Depends on Cell-Specific Endocytic and Mitochondrial Injury Pathways. *ACS Nano*, 2, 85-96.

[68] Ruan, G., Agrawal, A., Marcus, A. and Nie, S. (2007). Imaging and Tracking of Tat Peptide-Conjugated Quantum Dots in Living Cells: New Insights into Nanoparticle Uptake, Intracellular Transport, and Vesicle Shedding. *Journal of the American Chemical Society*, 129, 14759-14766.

[69] Park, J. and Oh, N. (2014). Endocytosis and exocytosis of nanoparticles in mammalian cells. *International Journal of Nanomedicine*, 9, 51-63.

[70] Iversen, T., Skotland, T. and Sandvig, K. (2011). Endocytosis and intracellular transport of nanoparticles: Present knowledge and need for future studies. *Nano Today*, 6, 176-185.

[71] Nativo, P., Prior, I. and Brust, M. (2008). Uptake and Intracellular Fate of Surface-Modified Gold Nanoparticles. *ACS Nano*, 2, 1639-1644.

[72] Wang, Z., Tiruppathi, C., Minshall, R. and Malik, A. (2009). Size and Dynamics of Caveolae Studied Using Nanoparticles in Living Endothelial Cells. *ACS Nano*, 3, 4110-4116.

Chapter 5 – Conclusions and future perspectives

5.1. Conclusions

The concern for the development of alternative cancer therapies that overcome the limitations of the conventional ones has been motivating the research focusing new nanotechnological solutions. As mentioned before, magnetic nanoparticles show several advantages in nanomedicine applications such as hyperthermia and magnetic guided drug delivery, due to their unique magnetic properties. The development of nanocarriers enables a controlled and safe release of drugs as well as a targeted delivery that avoids undesirable side effects. In this work, unloaded and bLf-loaded AMLs and SMLs were prepared as nanocarriers for this protein.

The synthesis of crystalline manganese ferrite nanoparticles was confirmed by X-ray diffraction and magnetic measurements. The nanoparticles exhibit superparamagnetic properties and a high saturation magnetization value (M_S= 55 emu g^{-1}). These nanoparticles were used in the preparation of aqueous and solid magnetoliposomes with sizes around 100 nm.

The incorporation of bLf in these nanocarriers was confirmed by fluorescence studies. In AMLs, bLf was probably located near the water/lipid interfaces, while in SMLs, bLf was linked to the surface of the lipid bilayer through a bioconjugation reaction between the protein and PEG molecules. It is possible that the incubation method used to bind bLf to PEG also promotes electrostatic interactions between the protein and phospholipids of the lipid bilayer. The presence of bLf increased the size of both magnetoliposomes, reaching hydrodynamic diameters around 150 nm.

Encapsulation and association efficiencies of ~ 62% and ~ 44% were obtained for AMLs and SMLs, respectively, suggesting that encapsulation of bLf is probably the best way to incorporate this protein in nanocarriers.

Cytotoxicity assays in two different cell lines, breast cancer cells and non-tumorigenic cells, were performed to study the effect of bLf-loaded magnetoliposomes. The bLf-loaded AMLs showed a slightly higher decrease of cell proliferation than bLf-loaded SMLs, possibly due to a lower amount of bLf carried in SMLs and the presence of PEG, that can difficult fusion with cell membranes. However, further independent assays need to be performed to assess statistical significant effect.

Fluorescence microscopy images indicated internalization of magnetoliposomes in both cell lines, proving the potential of these nanocarriers to deliver bLf inside tumor cells.

These results altogether demonstrate that the prepared magnetoliposomes are promising nanocarriers for proteins like lactoferrin allowing a selective targeting and triggered drug release upon rising of temperature (hyperthermia) without harming healthy cells. However, more investigation is required to improve their effectiveness in cancer cells.

5.2. Future perspectives

Regarding the low encapsulation efficiencies obtained for bLf-loaded magnetoliposomes, a different method should be tested for AMLs preparation, namely, the reverse phase evaporation method to compare it with the ethanol injection method. Also, protein-loading studies should be made to infer if a higher concentration of added bLf could result in a higher content of the protein in the formulations.

Determination of drug release rate from a liposomal formulation is important to predict its kinetics *in vivo*. Therefore, controlled release assays must be performed in conditions similar both in healthy and cancer cells.

Intact bLf can promote spatial problems due to its large size comparing to peptides and commonly used antitumor compounds. To overcome this, magnetoliposomes could be loaded with bLf derivative peptides with the same or higher anticancer activity.

Therapeutic efficiency of nanocarriers is increased when they can conduct a selective targeting and release bioactive compounds only in the local of interest. The cytotoxic effect of bLf when incorporated in the prepared magnetoliposomes was not evident. In a dual therapy, bLf could act as a ligand in the surface of magnetoliposomes to perform selective targeting, while antitumor drugs were encapsulated, promoting a synergistic effect that could enhance cytotoxicity against breast cancer cells.

PEGylation of SMLs is advantageous for increasing their lifetime in blood circulation and transport hydrophilic drugs but can present problems in cellular uptake and release of drugs. A new method of PEGylation could be used that allows the detachment of PEG in response to an intracellular or extracellular environment.

Triggered release studies of loaded protein with application of an alternating magnetic field or use of temperature or pH-sensitive lipids should be performed with the aim of increase the therapeutic effect of these nanocarriers.

For a clearer understanding on the localization of these nanocarriers inside the cells, cancer cells should be labeled with a fluorescent probe with excitation and emission bands easily separated from those of the dye used in magnetoliposomes. Also, the presence of lactoferrin inside the cells should be detected with the use of specific fluorescent markers for this protein.

In the future, *in vivo* approaches are required to study the pharmacokinetics of optimized bLf-loaded magnetoliposomes.